A Synchrotron Small-Angle X-ray Scattering Study of Order/Disorder in Colloidal Crystals

Een synchrotron kleine-hoek Röntgenverstrooiing studie van orde/wanorde in colloïdale kristallen

(met een samenvatting in het Nederlands)

Proefschrift ter verkrijging van de graad van doctor aan de Universiteit Utrecht op gezag van de Rector Magnificus, Prof. Dr. W.H. Gispen, ingevolge het besluit van het College voor Promoties in het openbaar te verdedigen op maandag 22 maart 2004 des middags te 12:45 uur

door

Igor Petrovich Dolbnya

geboren op 11 december 1962, te Krasnoyarsk, Rusland

Universiteit Utrecht

Promotor: Prof. dr. H. N. W. Lekkerkerker
verbonden aan de Faculteit Scheikunde van de Universiteit Utrecht

Co-promotoren: Dr. A. V. Petukhov
verbonden aan de Faculteit Scheikunde van de Universiteit Utrecht

Dr. G. J. Vroege
verbonden aan de Faculteit Scheikunde van de Universiteit Utrecht

Dr. W. Bras
verbonden aan de Nederlandse Organisatie voor Wetenschappelijk Onderzoek

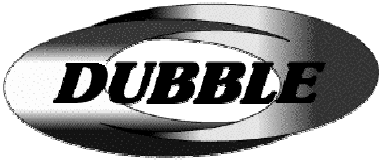

This work is financially supported by the Nederlandse Organisatie voor Wetenschappelijk Onderzoek (NWO) and was carried out at the Dutch-Belgian Beamline (DUBBLE) at the European Synchrotron Radiation Facility (ESRF) and at Utrecht University.

A digital version of this thesis can be downloaded from http://www.library.uu.nl
ISBN 90-393-3649-0

To P.A.D., L.A.D and I.V.D.

Cover: Colloidal crystals as seen by synchrotron x-rays

Front in reciprocal space with x-ray diffraction, this thesis;

Back in real space with x-ray phase-contrast imaging, unpublished.

Contents

Chapter 1

Introduction

Colloidal suspensions that form periodic self-assembling structures on sub-micrometer scales are of interest from both the fundamental scientific [1,2] and potential technological point of view [3]. Upon raising the concentration in a colloidal suspension of sufficiently monodisperse spheres the volume restrictions force particles to arrange themselves into close-packed structures. The face-centered cubic (fcc), hexagonal close-packed (hcp) and random stacking hexagonal close-packed (rhcp) phases lead to the most condensed way of packing, characterized by the same excluded volume. The fcc packing of non-interacting hard-ball spheres provides slightly larger phase space for fluctuations of the particle positions, leading to a very little preference of this structure due to the entropy contribution. However, dynamic effects or the presence of any weak interaction between the particles may dominate the final crystal structure. One of possible ways to modify the latter is to add non-interacting polymer molecules, which by osmotic compression introduce an additional depletion attraction between the colloidal particles.

Self-organisation of submicrometer colloidal hard spheres into crystalline structures provides an important and convenient model of crystal growth and glass formation. It also recently attracted significant attention as a technique of a cheap, large-scale fabrication of photonic materials. For the latter application the emphasis has been on the preparation of large single crystals with significant dielectric contrast between the spheres and the solvent, a low density of defects and small positional fluctuations of colloidal particles. Photonic crystals are regular three-dimensional (3D) dielectric structures with feature sizes on the order of the wavelength of interest. If the refraction index contrast is large enough the propagation and spontaneous emission of photons can be manipulated in new and exciting ways [3-5]. There are roughly two classes of methods to make 3D photonic crystals: on the one hand methods are employed that are also used in the fabrication of micro chips, or are

related to such methods (lithography, etching, etc.), on the other hand methods rely on the self-organization of colloids [4,5].

Optical and electron microscopy has provided essential information on the *local order* in colloidal crystals, while the *long-range order* is hardly ever addressed. In a *perfect* 3D crystal one can define a mathematically-ideal periodic average lattice, which 'locks' the averaged atomic positions. Small excursions of atoms around these lattice points due to their thermal motion does not destroy the very precise relation of the atomic positions on two opposite sides of one crystal. However, most real crystals are *imperfect* and their average lattice can only be defined over relatively small parts of the whole crystal. The long-range order can be easily destroyed by extended defects, external or internal (e.g., induced by various defects) strain field, etc. In addition, the colloidal spheres are never identical to each other but possess an inherent size polydispersity, which can also affect the long-range order. One of the very few earlier attempts to exploit small-angle X-ray diffraction has been applied to characterise the structure of charge-stabilised colloidal crystals [6]. The results obtained suggest that those crystals have a mosaic structure, i.e., the single crystal in fact consists of many positionally-independent fragments.

Small-angle x-ray scattering (SAXS) is essentially an elastic scattering technique. Hence the photon energy of the scattered waves and the length of the scattered wave vectors are preserved. In that case, it is often convenient to consider the scattering/diffraction in reciprocal space by constructing the sphere of diffraction, the so called *Ewald sphere* [7]. As can be seen in Fig. 1.1 the wave vector $\boldsymbol{k_0}$ of the incident X-ray beam points to the origin O of the reciprocal scattering space of the sample (i.e. the Fourier transform of the spatial distribution of the sample's scattering power), $\boldsymbol{k_s}$ is along the scattered beam. Both wave vectors have the same length, $2\pi/\lambda$, and therefore lie on a sphere in reciprocal space (the Ewald sphere). The difference vector $\boldsymbol{q}=\boldsymbol{k_s}-\boldsymbol{k_0}$ is called the scattering vector (or momentum transfer) and the angle between $\boldsymbol{k_0}$ and $\boldsymbol{k_s}$, 2θ, the scattering angle. In the case of diffraction from a three-dimensionally periodic crystal, the reciprocal scattering space is build up of localized spots forming the reciprocal lattice of the crystal.

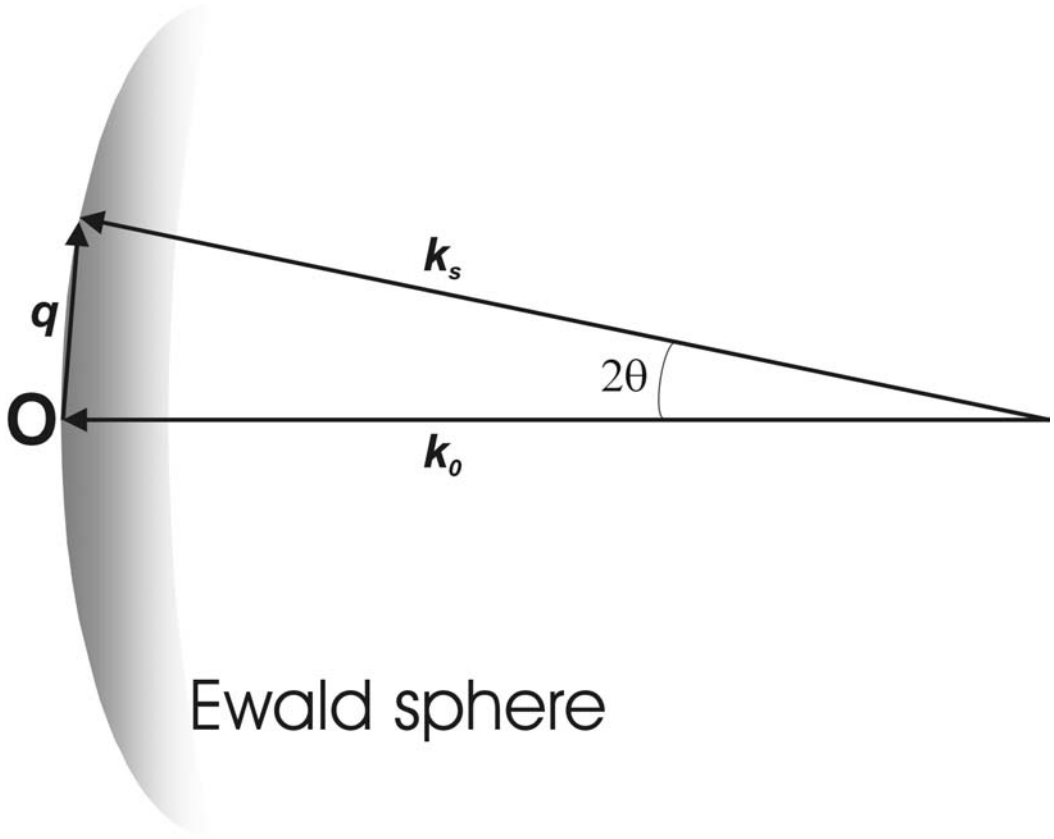

Figure 1.1. The schematics of the diffraction/scattering geometry in reciprocal space, the Ewald sphere construction. **O** *is the origin of reciprocal space,* $\boldsymbol{k_0}$ *is the incident wave vector,* $\boldsymbol{k_s}$ *is the scattered wave vector and* $\boldsymbol{q}$ *is the scattering vector/momentum transfer.*

The principles of x-ray diffraction of colloids are similar to the traditional crystallography of atomic systems. The diffraction pattern is determined by a two-dimensional cut of the Ewald sphere through the reciprocal lattice of a single crystal. By measuring the diffraction patterns at different sample orientations, one can reconstruct the three-dimensional reciprocal lattice, which yields information on the arrangement of neighbors in the crystal. In addition, one can measure the width of the reflections δq, which reflects the long-range positional order. There is, however, an essential difference between the crystallography of atomic and colloidal crystals, which originates from the drastic difference in the typical scales involved. While in atomic crystals typical spatial periods are of the order of the x-ray wavelength c.a. ~1 Å, in colloidal systems it is of the order of the wavelength of visible light, i.e. 3 to 4

orders of magnitude larger than the x-ray wavelength. The trivial consequence of this enormous difference in scales is that the reciprocal lattice vectors of colloidal crystals are very much smaller than the wave vector $k_0 = 2\pi/\lambda$ of the x-ray wave and diffraction can only be observed at small angles, $2\theta \sim 10^{-3}$ rad.

It turns out that small-angle x-ray diffraction is a very powerful and suitable technique to study various order/disorder parameters in colloidal crystals. The present work reports a first unambiguous prove that hard sphere colloidal crystals can possess perfect periodic order over distances comparable to the crystal size despite the size polydispersity of colloidal spheres. This conclusion is drawn from a profound evaluation of the size of the reciprocal lattice reflections using a specially-designed high-resolution X-ray diffraction technique with a resolution of one millionth of the incoming wave vector.

The key issue addressed in the present study was the characterization of various order parameters of the crystals such as positional, orientational and stacking orders. Although it is a general belief that the building blocks to obtain a high-quality crystal should be very monodisperse, the effect the colloid's inherent size polydispersity has on its crystalline order was unclear. By using the high-resolution synchrotron small-angle X-ray diffraction technique, the measurements of the orientational, positional and stacking order in crystals of 4 % polydisperse hard-sphere colloidal silica spheres grown in sediments of colloid-polymer mixtures have been performed on the Dutch-Belgian beamline (DUBBLE) BM26B [8] at the European Synchrotron Radiation Facility (ESRF) in Grenoble, France.

DUBBLE is an initiative and a project funded by the Dutch and Flemish Research Councils, Nederlandse Organisatie voor Wetenschappelijk Onderzoek (NWO) and Fonds voor Wetenschappelijk Onderzoek (FWO). The primary aim of this project is to satisfy the needs of the target groups of researchers as indicated by the funding organizations and to let new potential users from the Netherlands and Flanders get acquainted with synchrotron radiation experiments. The secondary aim, although in science terms equally important, is to provide beam time for general users of the ESRF. Under the terms of the agreement between DUBBLE and the ESRF 70% of the available beam time can be allocated to Dutch and Flemish user groups while the remaining 30% are made available to general ESRF users.

The design of the DUBBLE beam lines is based upon the report of E. Vlieg and Y.K. Levine [9]. The actual design phase of the beam lines started in January 1995. The design team was based at the Institute for Atomic and Molecular Physics (AMOLF) and at the NIKHEF (Nationaal Instituut voor Kern en Hoge Energie Fysica) in Amsterdam. In fact the design and construction of the beam lines was subcontracted to AMOLF. The construction phase began in 1996.

Regular experiments at the SAXS/WAXS station of the DUBBLE BM26B beamline started in around February 2000. More than ~300 experiments addressing a widely diverse range of topics, that can be found in such research areas as soft condensed matter, colloids, photonic materials, polymers, lipids and other materials and biological science subjects, have been performed in the years 2000-2003.

The present thesis is organized in the following manner.

Chapter 2 gives a general introduction to the principles of synchrotron radiation generation and a detailed description of the DUBBLE SAXS/WAXS apparatus. Particular attention has been devoted to the instrumental resolution issue.

Chapter 3 is an overview of existing theories relevant for the results presented later. Some extension has been made to describe the case of different degrees of stacking disorder in a system.

Chapter 4 discusses the results of measurements of the positional, orientational and stacking order in crystals of colloidal silica spheres. The results obtained show that the polydispersity does not prevent the formation of large single crystals with long-range positional order, but may lead to an inherent stacking disorder.

In Chapter 5, direct evidence of a dynamic regime of X-ray diffraction in long-range ordered colloidal crystal is demonstrated. It reveals itself in the diffraction patterns as an appearance of secondary Bragg rods. Simple estimates show that, in contrast to common belief, the dynamic character of x-ray diffraction can be rather typical for crystals consisting of highly ordered (sub)micrometer colloidal spheres and has to be taken into account.

Chapter 6 reports the *in-situ* observation of the crystal structure modification during drying. It is important to know how the structure and quality of the crystal is changing upon drying, as the drying process might be needed, for example, for photonic applications where a colloidal crystal is used as a template to fabricate a

band-gap photonic material. Particular efforts have been made to improve the instrumental resolution of the SAXS setup. We observed that at later stages of drying the diffraction peaks are seen to split into many separate reflections indicating that the crystal is not able to withstand anymore a too strong stress, caused by capillary forces, and it breaks up into smaller crystallites. We also see another manifestation of the dynamical regime of x-ray diffraction in the long-range ordered colloidal crystal. The diffraction switches to the (nearly) kinematic regime when the long-range positional order is destroyed. Our results indicate that the strength of the diffraction and its transition to the dynamic regime can be used as an alternative approach to probe the extent of the positional order in photonic colloidal crystals.

Literature:

[1] P.N. Pusey and W. van Megen, Nature (London), **320**, 340 (1986).

[2] A. P. Gast and W. L. Russel, Phys. Today, **51**, No. 12, 24, (1998).

[3] A. Blanco et al., Nature (London), **405**, 437 (2000).

[4] Y.A. Vlasov, X.-Z. Bo, J.C. Sturm, and D.J. Norris, Nature (London) **414**, 289 (2001)

[5] A. Yethiraj and A. van Blaaderen, Nature (London), **421**, 513 (2003).

[6] W. Vos, M. Megens, C.M. van Kats, and P. Bosecke, Langmuir, **13**, 6004 (1997), J.E.G.J. Wijnhoven, L. Bechger, and W.L. Vos, Chem. Mater, **13**, 4486 (2001).

[7] P.P. Ewald, Z. Krist. 56, 129 (1921); P.P. Ewald, Proc. Phys. Soc. London, **52**, 167 (1940).

[8] M.Borsboom, W.Bras, I.Cerjak, D.Detollenaere, D.Glastra van Loon, P.Goedtkindt, M.Konijnenburg, P.Lassing, Y.K.Levine, B.Munneke, M.Oversluizen, R. van Tol, E.Vlieg, The Dutch-Belgian Beamline at the ESRF, J. Synchr. Rad., **5**, 518 (1998).

[9] E. Vlieg and Y.K. Levine, *Conceptual design of DUBBLE*, Internal Report, 3/2/1994.

Chapter 2

The DUBBLE BM26 SAXS/WAXS beamline at ESRF

2.1 General introduction

Synchrotron radiation was originally produced as parasitic radiation from so-called first generation synchrotrons, which were designed to be powerful particle accelerators (1970's). Second generation machines were purpose-designed to produce radiation in the x-ray region. The world's first dedicated x-ray synchrotron was the Synchrotron Radiation Source (SRS) at the Daresbury Laboratory (ca. 1980), near to Warrington in the UK and this has been followed by a number of installations in other countries. Third generation synchrotron sources are now in operation and these have been designed for optimal performance from `insertion devices' rather than bending magnets. The European Synchrotron Radiation Facility (ESRF) in Grenoble, France was the first of these third generation sources and became available for user experiments in 1994 [http://www.esrf.fr]. The high brilliance of synchrotron radiation (SR) has had a dramatic effect on the potential for high quality experiments in many areas of research.

SR is the electromagnetic field emitted when relativistic charged particles are accelerated. In synchrotrons electrons, or positrons, are maintained in a quasi-circular orbit in a high-vacuum storage ring by the use of either electro- or permanent magnet arrays - the magnet lattice. As the particle bunch passes through the poles of a bending magnet its path becomes curved and a fan of synchrotron radiation is emitted tangentially in the forward direction. A series of bending magnets interspaced with straight sections are used to produce a closed particle orbit. Insertion devices can be fitted into the straight sections between bending magnets and these produce much more intense radiation. The energy of the beam, which is lost through radiative processes, is replenished via radiofrequency cavities in the beam path. Quadrupole and sextupole focusing magnets control the beam diameter and stability. Other

devices are beam steering magnets, beam position monitors and beam diagnostic devices.

Synchrotrons are complex machines and it is outside of the scope of this work to attempt to describe the physics involved in detail here. However, some of the fundamental aspects of synchrotron radiation which have had a direct importance for the experiments conducted during the course of this study will be discussed.

The principal components of a synchrotron radiation source are a linear accelerator, a booster synchrotron and a storage ring. The linear accelerator, or linac provides a source of electrons, which are injected into the booster synchrotron, where they are circulated and accelerated to the required energy, until they are injected into the main storage ring. The booster synchrotron may, or may not, operate at the same energy as the storage ring. At the ESRF the booster synchrotron increases the electron energy up to 6 GeV, the same as that of the storage ring before injection.

Useful radiation is produced from both bending magnets and insertion devices such as undulators and wigglers [1]. But characteristics of these types of radiation are fundamentally different. These characteristics are illustrated in Figure 2.1.

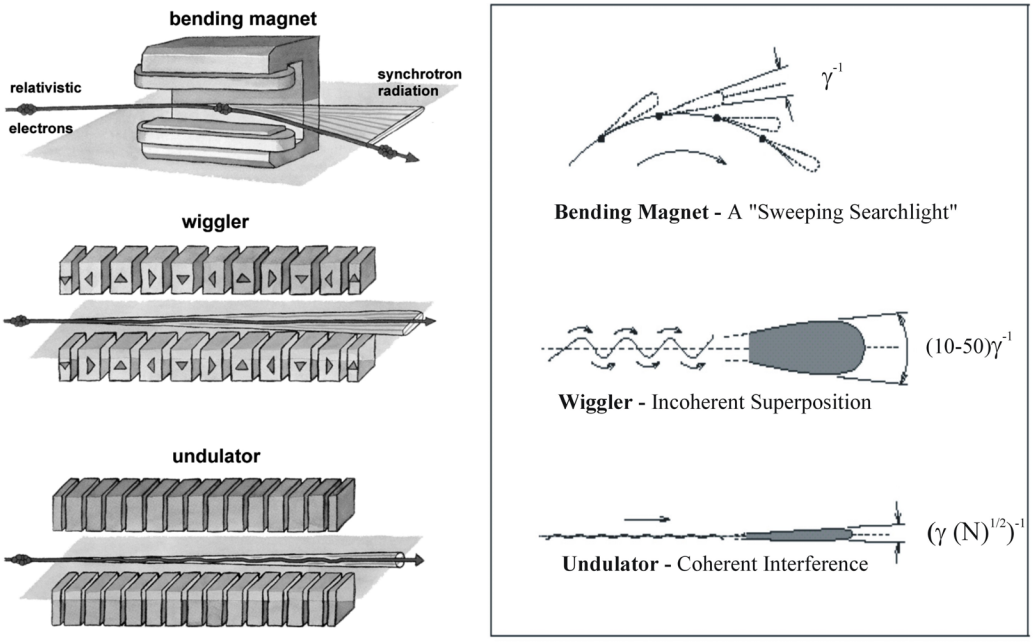

Figure 2.1. Comparison of the output angular radiation fans of three types of insertion devices. [ESRF publicity material]. Here γ is electron energy/$m_e c^2$ (m_e = electron mass, c = velocity of light), and N is the number of magnet periods.

Bending magnets

The radiation from bending magnets is in the form of a smooth continuum of energies which is defined by a single parameter, called the critical energy, e_c. The critical energy (in keV) is given by $\boldsymbol{e_c = 0.665BE_e^2}$, where B is the magnetic field in Tesla and E_e is the electron energy in GeV. Half of the emitted total power is radiated above the critical energy and half below. The photon flux radiated from bending magnets is significantly lower than that from insertion devices, for reasons described below.

Insertion devices

First and second generation synchrotrons use the radiation emitted from bending magnets as their prime source of x-rays. In third generation sources, the primary devices (those to which the machine is optimized) are those fitted into the straight sections, so called insertion devices. There are two types of insertion device in common use, multi-pole wigglers and undulators. Although similar in some respects, they vary significantly in the properties of the radiation which they produce. Therefore, they are described separately.

Both wigglers and undulators utilize a series of small magnets of alternating polarity causing the electrons to oscillate perpendicularly around their direction of motion. Each `wiggle' causes radiation to be emitted. In the simplest case a three-pole device produces a single wiggle, in practice a series of magnetic poles is often used to produce a multi-pole device.

1. In the wiggler regime transverse excursions of electrons are of such a magnitude that the related angular deviations are greater than the natural SR angular 'opening'/divergence. Pulses of radiation from subsequent magnetic poles interfere therefore incoherently. Spectrally hard x-rays are radiated along the emission axis and softer ones at increasing angles from the axis. Successive alternating magnetic periods produce circularly polarized radiation of opposite senses so that linearly polarized

radiation is produced. Wigglers radiate an intense flux over a large angular range with a brightness [1] greater than that obtained from a bending magnet.

2. In the undulator regime transverse oscillations of electrons are smaller in magnitude than for a wiggler and the related angular deviations are smaller than the natural angular divergence of SR. The amplitudes of electromagnetic fields emitted by each period are constrained to interfere coherently, resulting in a periodic spectral field. Although the total flux is generally no higher than that produced by a wiggler, the peak brilliance is orders of magnitude greater than that from both bending magnets and wigglers. Tuning of the harmonics produced from undulators is possible by varying the strength of the magnetic field, i.e. by varying the gap between magnetic poles.

There are several characteristics of synchrotron radiation that are of particular interest to *potential users*:

- **Critical wavelength** - the approximate wavelength of the most intense emission, λ (in Å)=12.38/e_c (e_c – critical energy, in keV).
- **Flux** (at the sample, at a particular wavelength and in a particular spectral bandwidth $\Delta\lambda/\lambda$) - the number of photons produced by the beamline optics per second per unit area available in the sample plane. Units are photons/s/mm^2/mA.
- **Emittance** - the product of the beam size by its divergence. It is specified in both the horizontal and vertical directions for the source. Units are metre·radians.
- **Electron beam lifetime** - the time-dependent decrease of the stored current such that $I(t) = I_0 e^{-t/\tau}$, where I_0 is the original current, τ is the lifetime. Generally expressed in hours.

The Dutch-Belgian beamlines (DUBBLE) at the ESRF receive its radiation from dipole magnet D26 of the ESRF. The available total 9 mrad horizontal radiation fan is split into two beamlines. Each beamline intercepts 2 mrad of radiation. The central 5 mrad are blocked out. ESRF bending magnets do not have a uniform magnetic field. The field along the electron orbit is changing from 0.4 Tesla to 0.8 Tesla. As a

[1] Brightness is the photon flux per unit phase space volume, often given in units of photons·s^{-1}·mr^{-1}·mm^{-2}·(0.1%spectral bandwidth)$^{-1}$.

consequence the electromagnetic spectrum emitted changes depending on which point is used as the source point. The spectrum emitted at 0.8 T is shifted to shorter wavelengths (‘harder’ radiation, critical energy of 19.15 keV). This beam line is referred to as the H(ard)-line and the other beam line as the S(oft)-line (‘softer’ radiation, critical energy of 9.58 keV). The H-line is closest to the shield wall of the ESRF storage ring. The radiation spectrum of the 0.8-T section of D26 bending magnet is presented in Fig. 2.2.

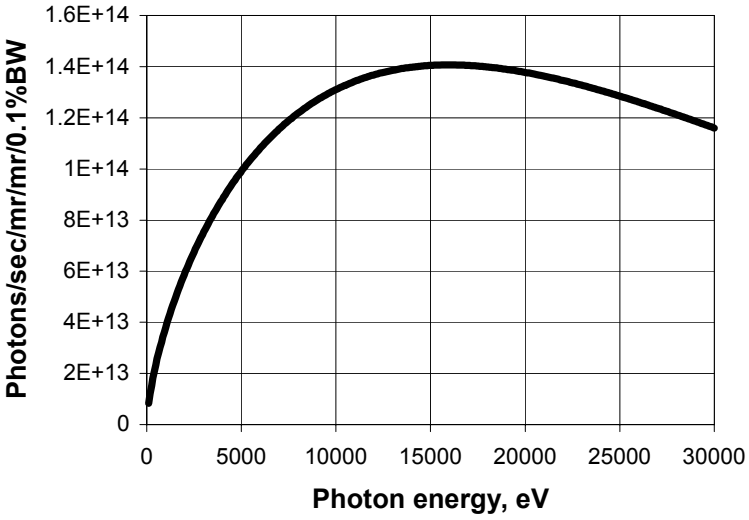

Figure 2.2. The calculated radiation spectrum of the ‘hard’ section of the D26 bending magnet.

The H-line is mainly dedicated to small- and wide-angle X-ray scattering (SAXS and WAXS) experiments. Also available is a '2+3' type diffractometer (combined '2+2' and 'z-axis') intended for surface and interface diffraction studies [2]. The latter instrument is not used in the present work.

2.2 Beamline X-ray optics

The schematic overall layout of DUBBLE optics is depicted in Figure 2.3.

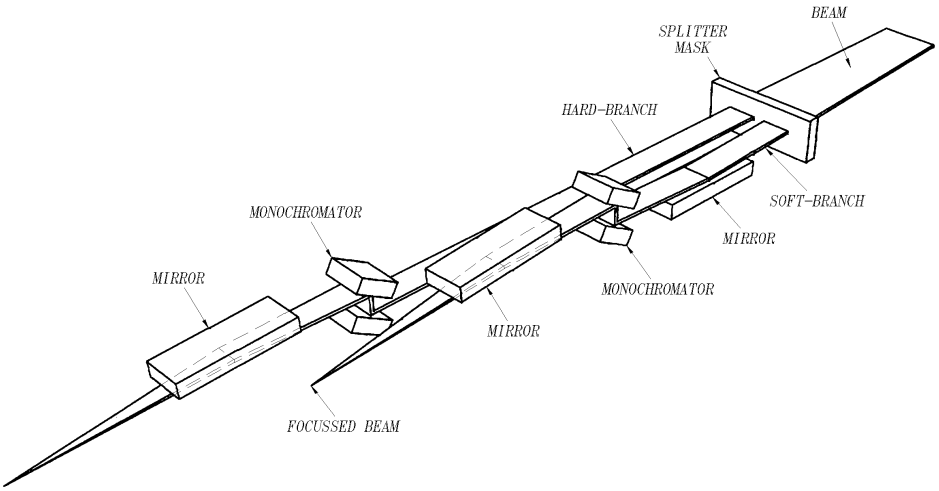

Figure 2.3. Schematic layout of the optical components of BM26. The 9 mrad radiation fan accepted by the front end is split by the cooled 'splitter mask' in two beam lines (distances and dimensions of the optical elements are not to scale, drawing is the courtesy of I. Cerjak).

The H-line X-ray optics consists of a double-crystal sagittally focusing Si(111) monochromator followed by a meridionally focusing mirror. The first (flat) crystal of the monochromator is water-cooled. The second multi-rib crystal is mounted in a specially designed bending mechanism providing a range of bending radii from ~1 m to infinity [3]. So, the second crystal can be bent and therefore focus the radiation in the horizontal plane. This is called sagittal focusing. To avoid anticlastic bending, and thus allowing a larger radiation fan to be focused, a multi-rib crystal design has been approved. In the design phase finite element analysis was performed in order to determine the ideal shape of the crystal. It was found at that time that a crystal with 4 ribs instead of the multi-rib crystal used in the original design could have a better performance. However, this has not been verified by experiments yet.

The focal distance can be easily changed so that the beam can be focused along the optical bench in the experimental hutch. The monochromator energy range tested so far is 6-30 keV and it delivers a spectral bandwidth, $\Delta\lambda/\lambda$, of about 5×10^{-4}.

The mirror is made of a highly polished single silicon crystal (overall dimensions: 1500 x 150 x 45 mm^3) and has two coatings: bare Si and Pt to operate at two different spectral ranges of 5-12 and 12-30 keV, respectively. The measured surface roughness is about 1.5 Å (rms) and the mirror has a slope error which is in the

micro radian range. The mirrors have been manufactured by REOSC and a bender design from Irelec is used (www.irelec.com). See figure 2.4.

By bending this mirror slightly the radiation is focused in the vertical plane. Depending on the focal distance required, bending radii are on the order of a few kilometers. The mirror receives the radiation under a glancing angle of ~2.6 mrad.
The advantage of this arrangement is that a change of angle of incidence of the mirror translates in relatively large vertical displacements of the beam in the experiments hutch. By choosing this solution one can keep the size of the downstream vacuum components limited to a reasonable size and one avoids large realignments of slits, samples and detector when changing the energy. The optical surface of the mirror faces downwards. This was implemented in case that at a moment in future the desire might exist to be working on surfaces of liquids.

The mirror is also used to suppress higher harmonics coming from the monochromator. The harmonics suppression coefficient achieved is about 10^{-3}. There is the option to install a collimating mirror at a later stage in the case that one wants to specialize in anomalous scattering. The typical dimensions of the beam in the focal spot are around 300×300 μm^2.

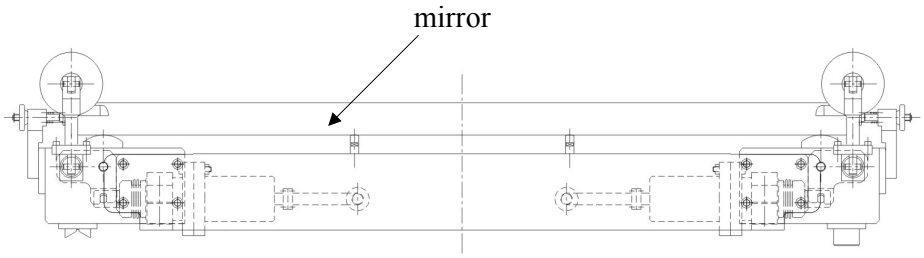

Figure 2.4. The bender design of Irelec. The mirror is bent by applying a force to two rollers placed acentrically with respect to two static rollers. The gravity compensation mechanisms are not shown. The bending radii required for the different mirrors of DUBBLE range from 5 – 22 km. This is easily achievable with this design.

Between all optical components slit sets are placed. There are also a few X-ray windows in the beamline. Most of them are made of beryllium. The total thickness of all the Be windows is 1.25 mm. The last exit window of the beamline vacuum pipe is covered with a 100 μm thick mica sheet. The vacuum design was done in such a way that the amount of Be windows in the beamline can be reduced. The primary reason for this was not only the absorption at lower energies, but also because Be windows may increase the parasitic scattering close to the direct beam. This is harmful for the

quality of SAXS experiments regarding background and achievable low-angle resolution. The only two fixed Be windows on the beamline are the obligatory: front end window separating the machine vacuum from the beamline vacuum and the window directly behind the splitter vessel. Two Be windows on the mirror vessel, separating the mirror vacuum chamber from the rest of the beamline, are actually mounted on a modified vacuum valve which can be opened when the vacuum conditions allow this.

Another inevitable consequence is that beamline windows shift the entire radiation spectrum towards higher energies as can be seen in Fig. 2.5.

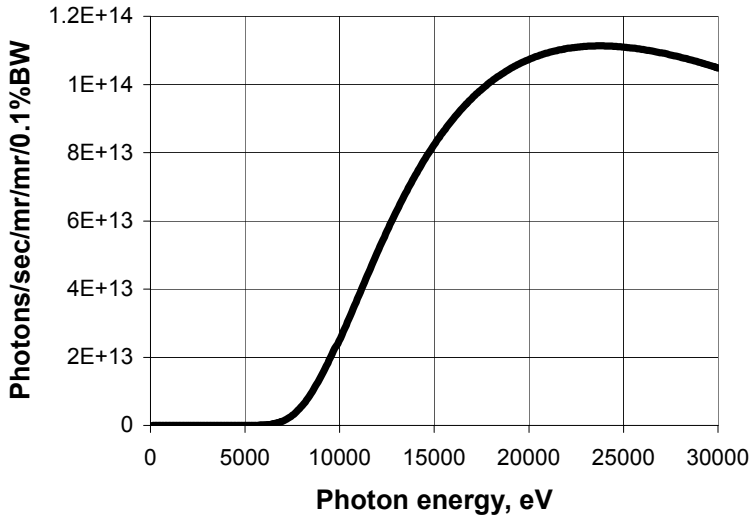

Figure 2.5. The calculated radiation spectrum of H-line. The absorption in the Be windows (total thickness of 1.25 mm) and 100 μm thick mica window is taken into account.

The experimentally measured number of photons in the focal spot is around $5 \cdot 10^{11}$ photons/sec at photon energy of 10 keV and 200 mA storage ring electron current. The H-line schematic layout is presented in Figure 2.6.

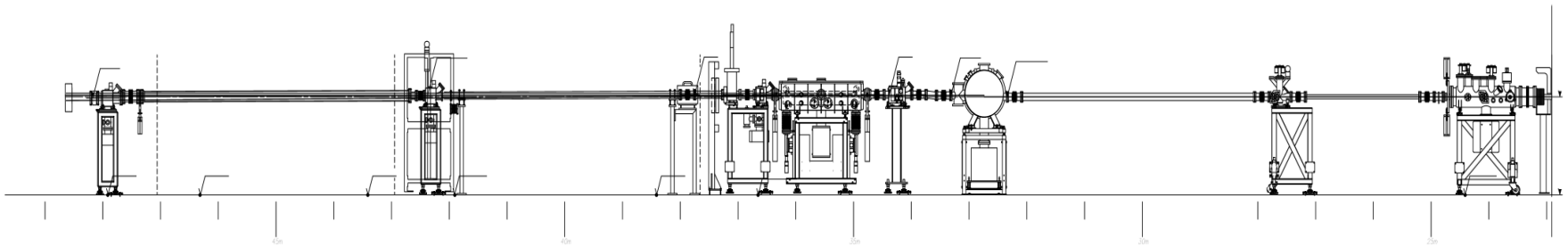

9 8 7 6 5 4 3 (2) 1

Optics hutch:			distance from tangent point [m]
1	splitter vessel		24
[2]	collimating mirror	(optional upgrade)	
3	monochromator	(sagittalfocusing Si 111)	33
4	focusing mirror	(at angle of 2.6 mrad, 2 strips on surface Si/Pt)	35.6
5	safety shutter		37
6	experiments hutch S-line (with one set of slits for H-line)		
7	control cabin S-line		
Experiments hutch:			
8	SAXS/WAXS equipment	(not shown)	48 - 56
9	ID diffractometer	(not shown)	58

Figure 2.6. The H-line layout.

2.3 The SAXS/WAXS Instrument

The experimental hutch contains the SAXS/WAXS instrument, shown schematically in Figure 2.7 with variable sample-to-detector distance of 1.4-8.5 m, and interface diffractometer mentioned above.

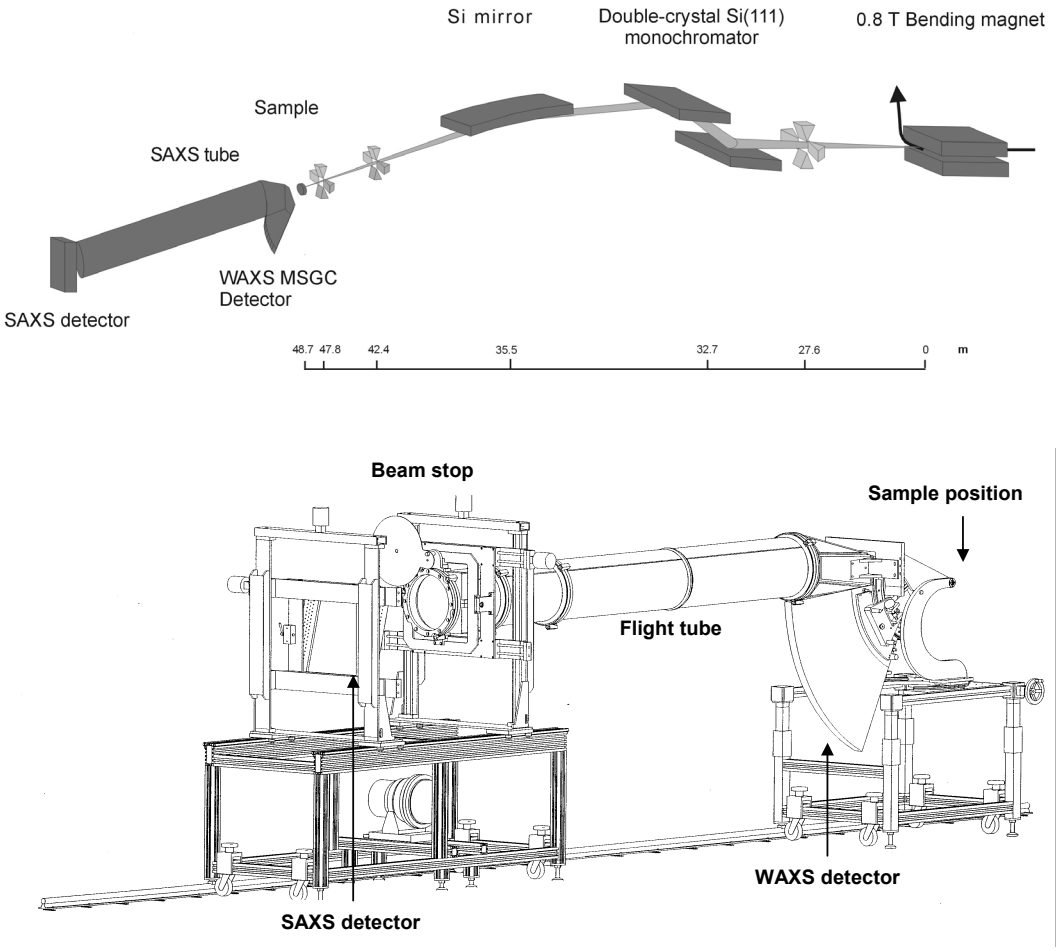

Figure 2.7. The SAXS/WAXS set-up. An evacuated flight tube is placed between the sample position and the SAXS and WAXS detectors. Heavy sample environments can be supported from the floor and a frame placed over the beam line exit.

There are several slits in the beamline. The most important are the primary beamline slits (slits set H1) which shape the primary (unmonochromated) X-ray beam and the last two slits (sets H5 and H6) which serve as guard slits to cut out parasitic small-angle scattering. Parasitic scattering is generated all through the beamline, whenever the X-ray beam touches anything, and has to be removed as much as possible. The

direct beam and the parasitic scatter cone are so intense that they damage detectors and therefore have to be taken out by a beamstop. Even if the intensity of the parasitic scatter cone falling on the detector is reduced by filters it is still orders of magnitude larger than the scattered intensity of any sample. This means that there is no serious information to be obtained in this region. Most of the parasitic scatter is found around the direct beam and thus the parasitic scatter cone is the main limiting factor in the low angle resolution that can be observed with a SAXS beamline.
However, if a slit touches the direct beam it also creates an intense scattering pattern. This slit scattering is also close to the direct beam. So the last two slits sets should not touch the beam but be positioned very close to the direct beam.

It was found so far that the maximum beam size that can be focused by the sagittal focusing system is ~44 mm as is determined by the width of the beamline's primary slits. The footprint on the monochromator crystals is ~52 mm wide. This means that effectively ~1.6 mrad of the radiation horizontal fan can be focused at present.

To measure the size of the focal beam spot (at different openings of the beamline's primary slits) a tantalum blade was scanned across the beam in the horizontal and vertical directions. The recorded integral intensities have been then differentiated and first derivatives of intensity profiles were fit to Gaussian profiles. The results for different openings of the primary slits are shown in Fig. 2.8.
The measurements have been performed at an X-ray photon energy of 15 keV. The X-ray beam has been focused (in both directions) at the sample position, located at a distance of 48.8 m from the bending magnet source. The fact that the focal beam spot is larger in the vertical direction can be attributed to vertical beam instabilities, most likely due to mechanical vibrations in the monochromator, which might effectively spread out the beam in that direction. Another possible reason can be the spherical aberrations induced by the mirror.

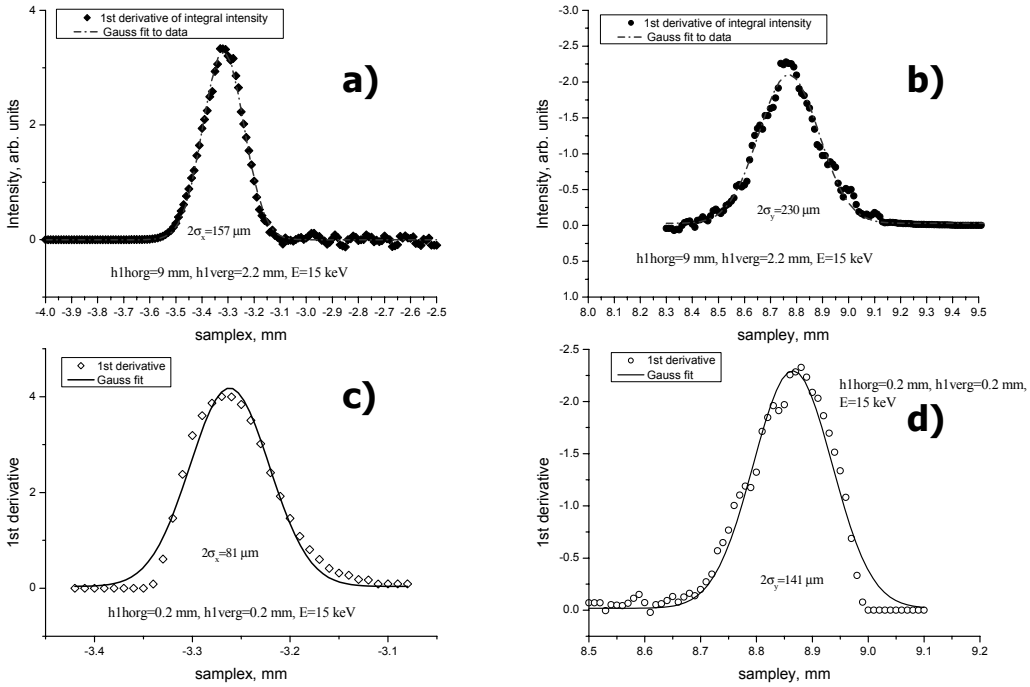

Fig. 2.8. The beam spot dimensions at the focal plane for different primary slits openings: 9×2.2 mm^2 (H×V) - (a) and (b), and 0.2×0.2 mm^2 - (c) and (d); (a) and (c) – horizontal profiles; (b) and (d) – vertical profiles.

2.4 Detectors

Detectors routinely utilized on the DUBBLE beamline at the moment are of the following types:

(1) Ionization chambers, used to monitor the incoming and transmitted intensities.

(2) Multiwire one-dimensional (quadrant type) and two-dimensional proportional gas chambers, and a CCD-camera (Photonic Science Xios-II, 1024×1024 pixels, resolution: ~23 μm) are used as SAXS-detectors [4]. The latter is optional where one needs to improve point-to-point resolution.

(3) The linear array micro-strip gas chamber is used as WAXS-detector [5].

The choice of detection system used for an x-ray diffraction experiment is of fundamental significance and will depend on factors such as the intensity of the source, the time resolution required and the type of information which is intended to be extracted during subsequent analysis. There is not a single system which is suitable

for all applications. It is clear that the choice of detector will always involve a degree of compromise, especially when one is performing experiments at the limits of the capabilities of the instrument.

For example, for structural crystallography work, good spatial resolution is required but high time resolution in general is not. Good spatial resolution is achieved by the use of many small sensor elements. This can take a significant amount of time to read out. In contrast, for studies utilizing high time resolution the number of sensing elements can be reduced to improve, i.e. reduce, the read-out time.

The characteristics of a detector system which are of interest to the experimentalist include:

1. Number of dimensions. One dimensional detectors are high-sensitivity single-event counters which are widely used with powder diffractometers. Two-dimensional, or area, detectors are often used in a single-crystal diffraction studies.

2. The dynamic range gives an indication of the numeric range of single 'pixel' photon events which may be detected before readout. For integrating devices this is often quoted in 'bit' terms; i.e. an 8-bit device will have a dynamic range of $2^8 = 256$, etc.

3. Detector efficiency. The effect of the detector on measurement accuracy is expressed by the detective quantum efficiency (DQE), defined as the square of the ratio of the output signal-to-noise ratio to the input signal-to-noise ratio:

$\mathrm{DQE} = (S_o/\sigma_o)^2/(S_i/\sigma_i)^2$,

where σ_o is the standard deviation of the output signal, with average value S_o, and σ_i is the standard deviation of the input signal, with average value S_i. For a perfect detector the DQE would be 1, but in reality many solid-state detectors achieve values of ≥ 0.5.

4. Spatial resolution is determined by the pixel size in solid-state detectors, by the wire separation in multiwire designs and by the scanner raster resolution for image plates and photographic film.

5. The point spread function (PSF) describes the amplitude response of the detector as a function of distance from the centre of a point signal, and it is generally assumed to have a Gaussian profile. The PSF is usually quoted as the full width at half maximum (FWHM) of the Gaussian profile.

6. Linearity of response. Non-linearity of response can be caused by a fall off in DQE at high count rates due to “dead-time” counting losses in integrating detectors or in saturation effects in media based detectors. Serious errors in the interpretation of intensity measurements can be introduced if a detector is used outside its linear region.
7. Spatial distortion is a function of irregularities in detection unit spatial arrangement and is present in measurable degrees in most detectors. For many studies, especially crystallographic studies, it has to be corrected for.
8. The read out rate is the rate at which data can be retrieved from the detecting surface and is a function of the DQE, the incident flux and the nature of the electronic circuitry (or other means) by which the data are transferred to permanent media. The read out rate varies from microseconds for some types of electronic devices to tens of minutes for high resolution devices.

These factors are considered in greater detail in [6,7].

The choice of detector for any particular application will be made on the basis of factors mentioned above and on other, non-technical, considerations such as availability, cost, portability, etc. For diffraction experiments, several particular types of detectors have routinely been used and these are described briefly in the following section.

1. X-ray photographic film has been used for many years. It has a reasonable dynamic range and spatial resolution but the processing is time consuming. Utilization of the data generally relies on a subsequent digitization process, which is often 8-12 bit, thus significantly reducing the useful dynamic range. Photographic film is excellent for high resolution static structural studies, but has limited application in time resolved studies as data collection times are of the order of hours on a conventional X-ray tube generator and minutes on a synchrotron.

2. Image plates are a comparatively recent development and consist of an aluminum or polymer substrate [often A4 in size (297x210 mm^2)] that has been coated on one side by a rare earth doped barium halide phosphor. This photo-stimulated phosphor can store a fraction of the absorbed x-ray energy and when later stimulated by visible

light, in the form of a scanning HeNe laser, it emits photo-stimulated luminescence, the intensity of which is proportional to the absorbed x-ray intensity. Image plates have excellent dynamic range, spatial resolution and DQE with significantly improved background noise levels over photographic films. However, although exposure times are improved in comparison with film, laser readouts generally take several minutes, which again results in a limited application in time-resolved experiments.

3. Semiconductor-based detectors fall into the categories of Silicon Intensifier Target (SIT) and Charge Coupled Device (CCD) technologies. A popular generic name for SIT types of detector is TV detector, due to the original application in TV cameras. SIT technology has been largely replaced by CCD technology due to reduced costs, improved resolution, higher dynamic range and the capability of higher frame readout rates coupled with much simpler electronics.

2.4.1 MWPC counters

4. The detectors, which were chosen as routine SAXS and WAXS detectors, are gas-filled Multi-wire proportional (MWPC) and micro-strip (MSGC) chambers. They have similar principle of operation, although differ in characteristics and technical design. Below we consider these two types of detectors in more detail.

MWPC counters are formed of one- or two-dimensional arrays (often 512 × 512 channels) of parallel wires held at high voltage in a mixed gas filled atmosphere. The principle of operation of gas detectors is based on the collection and amplification of photo-electrons, liberated in a suitable gas mixture by the photoelectric effect when the X-rays pass through the gas volume. Further to this, an Auger electron and/or X-ray fluorescence photon releases the excess energy of the X-ray photon. Photon absorption events are electronically logged as a function of position along the wires. The typical operational energy range of these detectors is 2-25 keV.

The photo- and Auger electrons are thermalized by ionization of the gas. The result is typically a few hundreds of secondary electrons. In the case of photon counting, the detector detects the charge of the secondary electrons and generates a

signal. The noble gas used as the main detecting agent is a defect-free and homogeneous medium, therefore electrons can drift over a long distance without losses. The presence of electronegative impurities like H_2O, oxygen etc. can induce some losses in charge collection. The extent of the secondary-electron cloud is the limiting factor for spatial resolution of the detector. The (re)absorption of fluorescent photons by the gas contributes to the tail of the point-spread function of the detector. To obtain reasonable quantum efficiency for X-ray absorption, a certain gas depth is needed. This gas thickness will imply a parallax in the X-ray imaging if the photons do not impinge under right angles onto the detector. However, there are several ways to handle, reduce or even eliminate the parallax.

The number of secondary electrons created in the gas is rather small ($\sim E_{x\text{-}ray}/30eV$) and it is convenient to multiply them in the gas in order to have a detectable signal. For electron multiplication one needs to create a region in the gas with a sufficiently high electric field, where electrons can gain energy between the collision of the gas atoms. If the energy gain exceeds the ionization energy of the gas atoms, an avalanche multiplication will take place. The multiplication is an exponential process, but can be controlled. The extreme limit is gas discharge. Depending on the gas composition, the typical drift speed of the electrons in the gas is in the order of few cm/μsecond. The signal rise time is essentially limited by the multiplication length divided by the drift speed. Positive ions created at the multiplication have considerably lower drift speed and in the case of high local count rate can reduce the electric field by screening (space charge effect). In such a case, the multiplication factor is *locally* reduced.

The ion neutralization takes place on the cathode. The result of this process is a neutral and *excited* gas atom (noble gas). In the pure noble gas, there are two main de-excitation processes: UV light emission and direct energy transfer to the cathode metal by collision. In the last case, it is very likely that an electron is emitted from the cathode. Similarly, an electron emission can take place from the cathode metal surface by the photoelectric effect caused by UV absorption. Electrons liberated in these processes create a positive feedback in the amplification process and can lead to a breakdown in the gas. To limit the photon feedback, a polyatomic gas is added to the detector. These so-called quencher molecules (methane, ethane, carbon dioxide etc.) de-excite the noble gas atoms by absorbing the UV photons and collision. They emit

the excess energy by infrared emission, hence the photoelectric effect on the cathode is no longer possible.

In MWPCs the high electric field, necessary for electron multiplication, is created by applying a high voltage potential on fine wire(s) mounted in a gas chamber. The electric field strength close to the wire surface can reach the necessary value for electron multiplication. The main advantage of this construction is that the electric field is radial and its strength is rapidly decreasing with the distance from the wire. Hence, the avalanche multiplication is confined to the region near to the wire surface and thus the build up of a spark discharge is *naturally* limited. The signal rise time is in the order of few nanoseconds, as a result of the short multiplication distance.

In MWPCs hundreds of such wires are fixed on the anode frame. Typically, they are of 5-10 μm in diameter, made of tungsten and fixed on a suitable frame. The anode frame is then sandwiched between two cathode frames made from thicker wires. Wires run perpendicularly to latter two frames and serve as signal pick up electrodes to determine the X and Y coordinates of the photon absorption. The critical parameter is the wire spacing on the anode frame. The anode wire pitch and the anode-to-cathode spacing have to be roughly identical. This creates a serious technical difficulty for large frames with an anode wire pitch below 1 mm.
Positive ions have to drift over the anode-cathode distance, which limits the local rate capability of the detector close to 10^5 cps/mm^2.

A detector has to withstand a high-accumulated dose during an experiment. Noble gases, used to detect X-rays, are inherently radiation hard and are not altered by radiation. However, the added organic (quenching) molecules are readily cracked by radiation and different types of radicals are created. The result is an isolating deposit in the detector, which initially appears as a ‘dead’ (non-counting) spot in the detector. The method used on DUBBLE to suppress the radiation damage of the detector is to flow the gas continuously through the detector. The applied mixture is Ar (Q.S.), ethane (10%), CF4 (0.5%). The pressure and the flow rate (6l/hour) are maintained by a special gas handling system developed during the course of this work. The

advantage of such a system is that possible (for example radiation induced) emanations from the detector construction materials are also eliminated.

The limitations of this system are principally concerned with the inability of the associated electronics to adequately discriminate between individual events at high photon fluxes. This has direct implications for both the local and global count rates, if the detector is to be maintained in the linear response region. The MWPC detectors used at DUBBLE are count rate limited, mainly due to the relatively slow readout used (delay line based data acquisition system). However, the possible time resolution is excellent (down to 10 μsec), noise is almost zero, the dynamic range is high (and is limited only by the electronic 'memory depth'). The inherent limitations of earlier generations of MWPCs have been largely addressed in the latest generation of devices, such as the RAPID detector developed at the Daresbury SRS, which has at least a twenty-fold increase in throughput over earlier designs [8].

2.4.2 The MSGC counter

5. For small-angle X-ray scattering (SAXS) experiments one can use a variety of different types of 2D and 1D position sensitive detectors. For wide-angle X-ray scattering (WAXS) a fast, angular sensitive detector with high count rate capabilities was required with sufficient angular resolution and a large opening angle. The WAXS detector used at DUBBLE SAXS/WAXS instrument is a one-dimensional linear array curved microstrip gas chamber (MSGC). The MSGC detector was specifically designed to simultaneously record wide-angle scattering/diffraction patterns, in combination with an independent SAXS detector, in time resolved combined SAXS/WAXS experiments with a time resolution down to a few msecs per time frame. The special requirement is to be able to sustain high *local* count rates since the wide-angle diffraction peaks from crystalline materials are often quite sharp and fairly intense.

MSGCs are produced with thin metal anode and cathode microstrips lithographically printed on insulating or semiconducting glass substrates. The small spacing between anode and cathode electrodes allows for a small drift distance for

collection of positive ions, produced in electron multiplication avalanches, leading to sub-μs ion transit times, and thereby decreasing the space charge effect. Hence the count rate capability is increased by about two orders of magnitude as compared to standard multi-wire gas proportional counters [9,10].

The developed MSGC detector is a "curved" detector thus avoiding parallax problems, due to the large X-ray absorption length in a gas chamber, when X-rays are not impinging at right angles onto the detection surface. The special feature is that the X-ray photons propagate through the drift space parallel to the anode strips and over the glass substrates instead of onto it. This also allows to avoid problems with escape electrons when the X-ray photon would be absorbed in the glass.

The strip pattern consists of 1024 10-μm wide aluminium anode and 90-μm wide cathode strips of 1 μm thickness printed on 0.4-mm thick D263 glass plates. The spatial period of the strip pattern is 400 μm. All the anode strip electrodes point to the sample position, placed at a radius of 360 mm from the inside edge of the 40-mm long anode strips. The distance between the drift electrode and the glass plates is 10 mm. The 8-mm wide detector entrance window is covered with aluminized Mylar film. The detector has a total acceptance angle of 60° with an ultimate angular resolution of nearly 0.03°. Depending on the X-ray photon energy used, the detector may be filled with different gas mixtures such as Ar/DiMethylEther (DME) or Xe/DME.

In the detector, a negative potential is applied to the drift electrode. The anode strips are grounded via the DC connection to the preamplifier. Each anode strip is individually equipped with a charge sensitive preamplifier-shaper, discriminator and scaler. The rear edge of the strips is wire bonded to the electronics. Figure 2.9 shows the schematics of the operational principle of the detector electronics.

There is also an electronic circuit for the detection of 2-strip coincidence events. Such a coincidence event is indicative of a photon that impinges on a position between two strips. The addition of the coincidence circuit doubles the number of channels to 2048, thus improving the angular resolution by a factor two. The readouts of real (physical) channels can be corrected for coincidences by subtracting the number of counts of corresponding coincidence (virtual) channels from the number of counts of its neighbouring real channels.

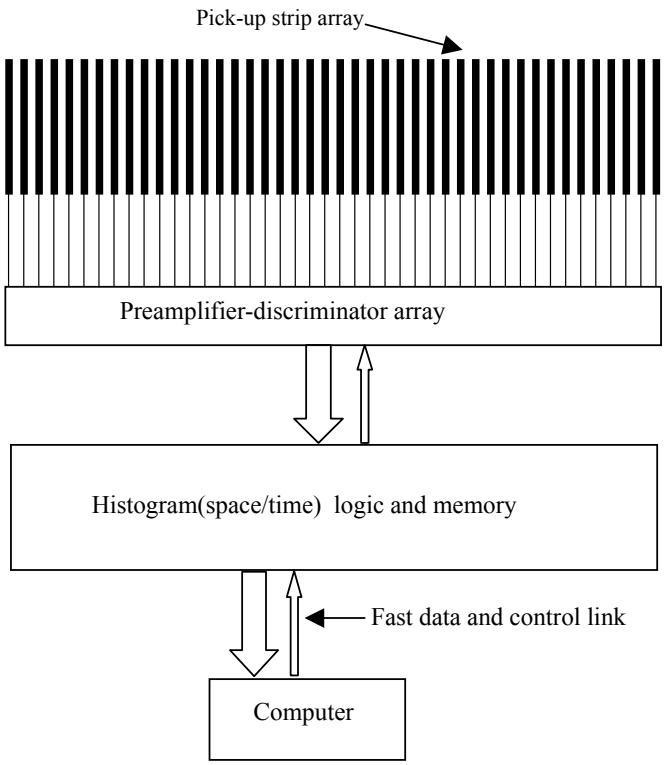

Fig. 2.9. Schematic arrangement of the one-dimensional, parallel readout WAXS-detector.

The detector electronics consist of two sets of 2048 12-bits scalers which are being read out every 0.5 msec. While one set of scalers is counting the data contained in the other set is transferred to a 32-bits incrementing memory thus leading to a dead time free read-out mechanism. There is also a facility to read sixteen general-purpose input channels. These channels can be used to record parameters associated with the experiments like for instance read-out signals of an X-ray intensity monitor or the sample temperature. These readings are converted into frequency signals and passed over to the same type of counters as used for the other channels. Special data acquisition software has been developed to control both the SAXS and WAXS detectors operation [11].

2.4.3 Performance of MSGC

Figure 2.10 shows the characteristic count load curve of the MSGC. Shown is the integrated intensity over the Si(111) Bragg reflection, normalized to the calculated peak width, as a function of the monitor ion chamber signal, after the peaks were fitted to a Gaussian profile. As seen from the figure, at the point where the detector begins to saturate the achieved local count rate is ~450 kHz per detector channel. This falls short of the restrictions on time resolution, by a factor of ~20, imposed by the response time of the detector gas chamber and the signal shaping time of preamplifiers used (~100 ns). This is most likely due to the effect of surface charging of the glass substrates and subsequent drop in the gas gain.

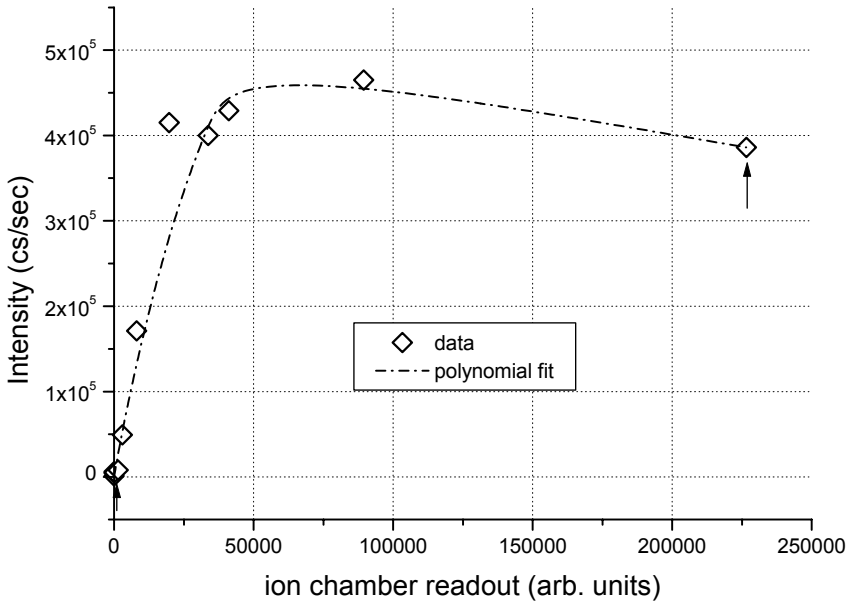

Fig. 2.10. Integrated intensity over the Si(111) reflection, normalized to the calculated peak width. Arrows in the plot indicate the fitting range. Detector settings: Ar:DME - 0.7:0.3, pressure - 1.3 bar, HV applied on drift gap was -2100 V, HV applied between anode and cathode strips was -610 V.

The time frame rate performance of the detector was also tested out by measuring the powder diffraction pattern of high density polyethylene. Figure 2.11 shows the time behaviour of the detector at an extreme data collection rate of 1.5 ms per time frame.

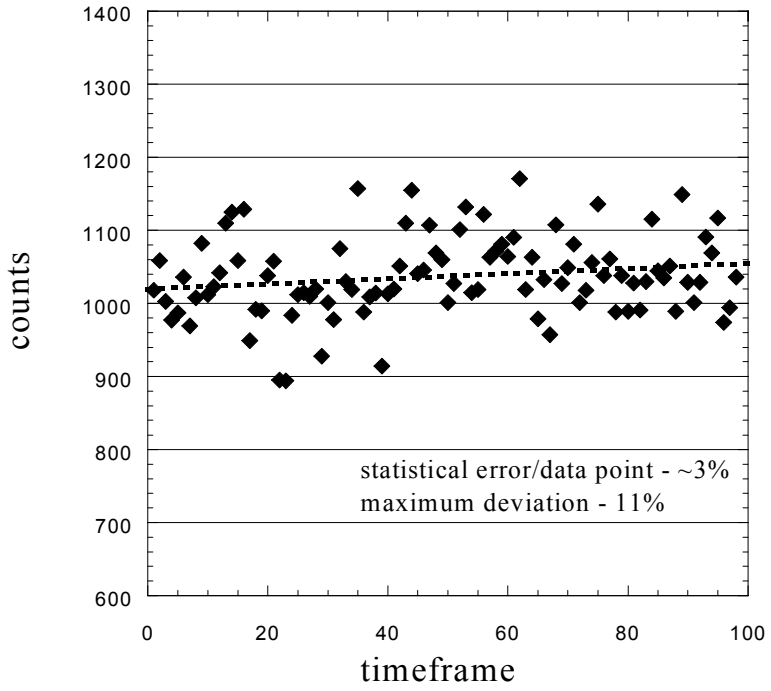

Fig. 2.11. Time evolution of the integrated intensity of the (110)-reflection of HDPE (high density polyethylene) shows good agreement with Poisson's photon counting statistics. The dashed line is a linear fit to the data points. The time framing rate was 1.5 msec/frame.

The technical characteristics of position-sensitive detectors used at the DUBBLE SAXS/WAXS beamline are summarized in Table 1.

Table 1.

Detector type	Focal Distance	Count rate, Cs/s/channel	Dynamic range	Spatial resolution	Readout	Global count rate	Active length/area	Gas mixture
MWPC 1D quadrant detector [4]	-	1×10^3	10^5	300-400 μm	Delay line	~800-900 kHz	15 cm, 2048 pixels	Ar/C_2H_6
MWPC 2D detector [4]	-	1×10^3	10^5	400-500 μm	Delay line	~800-900 kHz	13.3x13.3 cm^2, 512×512 pixels	Ar/C_2H_6
Photonics Science Xios-II CCD camera	-		16 bits	~25 μm	Shift registers		1024×1024 pixels	-
MSGC, (Dubble) [5]	0.38 m	4.5×10^5	10^6	400 μm	Parallel	~450MHz	60 Degrees, 2048 pixels	Ar/DME or Xe/DME

2.5 Instrumental resolution

2.5.1 Transverse resolution

In this thesis the transverse resolution is defined as the resolution with which a scattering (or diffraction) pattern $I(\boldsymbol{q})$ can be measured at the DUBBLE SAXS/WAXS beamline. Here I denotes the scattering intensity and $\boldsymbol{q}$ is the scattering vector. At small angles $\boldsymbol{q}$ is practically orthogonal to the wavevector of the incident x-ray wave, which explains the use of the word "transverse" here. It is also introduced in order to distinguish it from the longitudinal resolution of a single-crystal diffraction scheme, which is discussed in Section 2.5.2. In fact, the transverse resolution is the only relevant resolution of the setup for most experiments at DUBBLE (for example, in small-angle scattering, powder or fiber diffraction, etc.).

Apart from the resolution of the detector itself, which is discussed above, the transverse resolution is also determined by the quality and coherence of the x-ray beam. A scattering or diffraction pattern appears as a result of coherent interference. The beam coherence lengths define the coherently irradiated volume on a sample and also contribute to the achievable instrumental resolution. Thereby, this implies certain requirements on the beam coherence length.

In the transverse direction, the coherence length is basically determined by the angular source size [2] as it is seen from the sample plane. For a freely-propagating beam it can be written as

$l_{\mathrm{tr}} = \lambda R_s / d_s$,

where R_s is the distance between the radiation source and the sample, and d_s is the source size. The inverse of this value $2\pi/l_{\mathrm{tr}}$ mainly determines the maximum resolution $\delta q_{\perp}$ that can be achieved in the transverse direction.

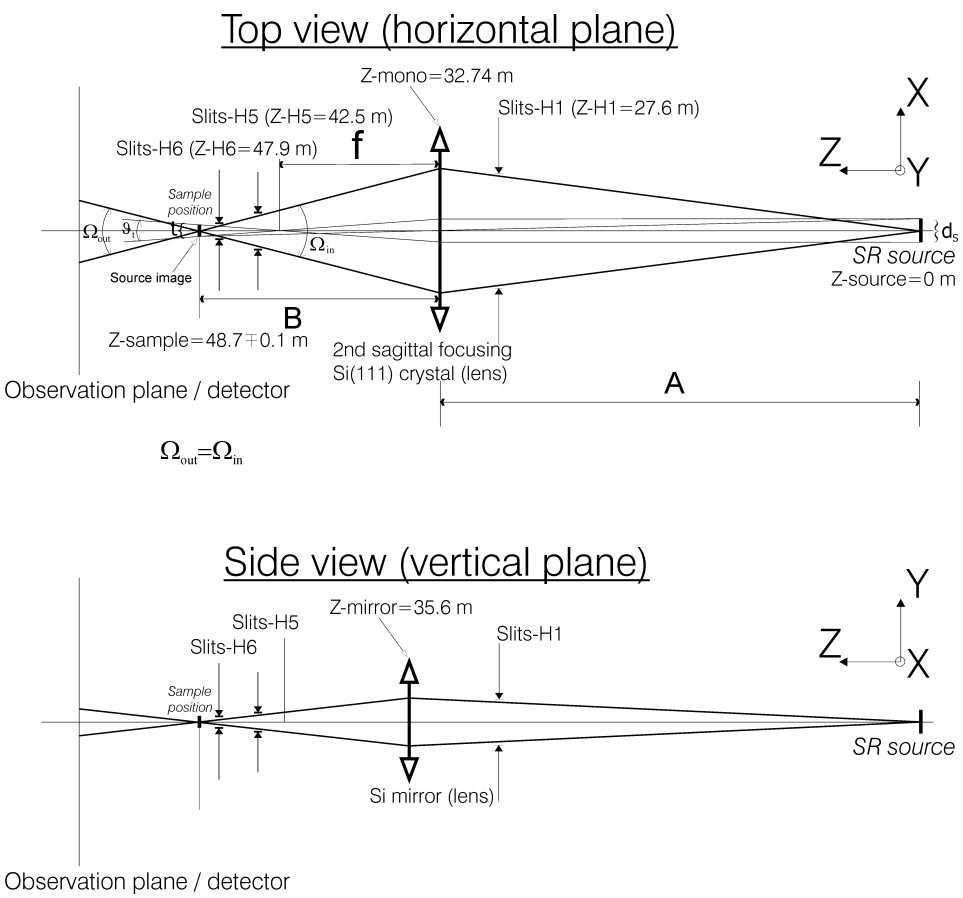

Fig. 2.12. The beamline optical geometry.

Assuming a source size of ~100 μm (rms), at 48 m distance from the source and a wavelength of 1 Å, one may estimate the transverse coherence length of the beam at the sample position to be $l_{tr} \cong 50$ μm. This is valid under conditions that there are no optics and defining/collimating apertures in the beam.

Fig. 2.12 depicts the beam line optical geometry. For many experiments the beam has to be focused at the sample to minimize the beam size, as it is shown in the figure. Below we will consider the transverse coherence of the beam in this case.

The second, focusing, crystal of the monochromator and the mirror can be considered as thin lenses since they are placed at large distances from the source and because of the small angular divergence of the beam. With a lens one needs to use the projected source size at the position of lens in order to estimate the transverse coherence length in the sample plane. In the vertical plane the angular beam divergence is determined by the natural divergence of the SR bending magnet beam, unless the primary beamline aperture does collimate it further. Synchrotron radiation

occurs in a narrow cone with nominal angular width ~1/γ, where γ is the ratio of the electron energy to the energy of the rest electron mass. In case of the 6-GeV ESRF machine it equals to 0.511[MeV]/6000 ≅ 85 μrad.

In the horizontal plane (i.e. electron orbit plane) it is ultimately determined by the width of the primary beamline aperture located at 27.6 m from the source. In case of aperture sizes corresponding to the above mentioned natural divergence of 85 μrad (2.35mm×2.35mm), the projected source size (~100 μm) at the monochromator second crystal, d_p, would be 100+32.74*85 [μm]=2883 μm, and at the mirror 100+35.6*85 [μm]=3130 μm. Hence, at the sample position, using 1 Å X-rays, one finds a horizontal transverse length $l_{tr,h}= \lambda R_{mono\text{-}sample}/d_p \cong 0.53$ μm, and a vertical transverse length $l_{tr,v}= \lambda R_{mirror\text{-}sample}/d_p \cong 0.43$ μm.

By collimating the beam down by means of primary slits, one can improve this situation. For instance, with apertures of ~0.1mm×0.1mm the horizontal length becomes $l_{tr,h}$ ~7.4 μm, and the vertical one $l_{tr,v}$ ~5.8 μm. The inverse of that length, $2\pi/l_{tr}$, will define the ultimate limit of the resolution $\delta q_{\perp}$ in reciprocal space in the transverse direction.

2.5.2 Longitudinal resolution in single-crystal diffraction

Coherent properties of an x-ray beam are different in the transverse and longitudinal directions. As will be shown here, in the longitudinal direction the conditions for coherent interference can be fulfilled on much larger distances than those in the transverse direction. As will be further demonstrated in Chapter 4, this can be exploited for a high-resolution diffraction study in a single-crystal diffraction mode.

In the longitudinal direction (along the incoming wave vector) the coherence length is determined by the spectral bandwidth of the incoming beam and is given by [12,13]:

$l_{long} = \lambda^2/\Delta\lambda$.

To fulfill the conditions of coherent diffraction, this length should be compared with the optical path length difference between waves diffracted at the rear and front sides

of the sample with respect to the incoming beam as is schematically shown in Fig. 2.13.

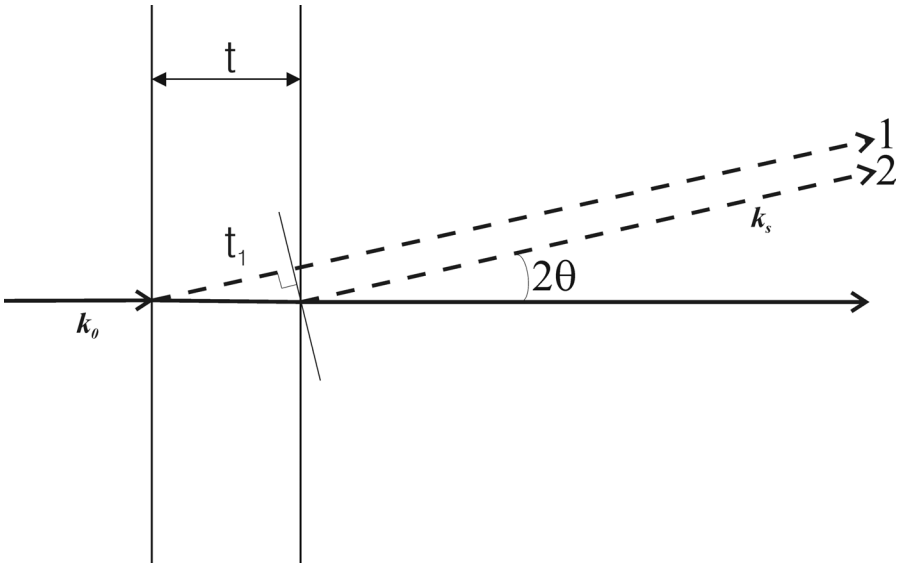

Fig.2.13. Sketch illustrating the optical path length difference between two waves diffracted at front and back sides of the sample.

This is equal to

$\Delta_{path}=t-t_1=t(1-\cos 2\theta)=2t\cdot\sin^2\theta$,

where 2θ is the scattering/diffracting angle and t is the sample thickness. For coherent interference, Δ_{path} should be either less or equal to l_{long} . Using this simple relation, one may then obtain an estimate of the optimum thickness of the sample, t_{opt}, which is equal to

$t_{opt}=\lambda^2/(\Delta\lambda\cdot 2\sin^2\theta)$.

The beamline produces monochromatic light with $\Delta\lambda/\lambda$ of, typically, $\sim 5\cdot 10^{-4}$. In the case of small-angle X-ray diffraction/scattering, depending on the sample-to-detector distance, the scattering angles vary from ~0.01° to ~5°. Thus, for wavelengths typically used in SAXS (0.7-2 Å), the finite spectral bandwidth of the radiation does not destroy coherent summation of the waves scattered by objects separated in the longitudinal direction by the distance t_{opt}, which ranges from ~40 μm up to a maximum value of 26 m (!). In fact, the latter is just an extreme upper limit.

This effect can be also seen from the Ewald sphere [14] construction in Fig. 2.14. The wavelength bandwidth, $\Delta\lambda$, leads to the spread of the radii of the Ewald sphere for the case of small divergences of incoming and scattered beams. Therefore, the Ewald sphere degenerates into a spherical shell of variable thickness. The thickness/width of that shell, $\delta q_{||}$, at scattering angle, 2θ, determines the resolution in reciprocal space along the scattered vector. Consequently, the value $2\pi/\delta q_{||}$ determines the characteristic distance along the beam over which the scattered waves can interfere with each other in the diffraction pattern at the plane/point of observation.

From geometrical considerations one may deduce the value of the thickness of the Ewald shell, $\delta q_{||}$, at a given scattering angle 2θ, shown in Fig. 2.14 as a solid black segment (right panel), by:

$$\delta q_{||,1} = (k_0 + \triangle k)\cdot\cos(2(\theta-\theta_1)) - k_0 - \triangle k\cdot\cos(2\theta),$$

which, in an approximation of small scattering/diffracting angles and narrow wavelength spreads, is equal to

$$\triangle k(1-\cos 2\theta) = 2\triangle k\sin^2\theta \simeq (4\pi\triangle\lambda/\lambda^2)\theta^2.$$

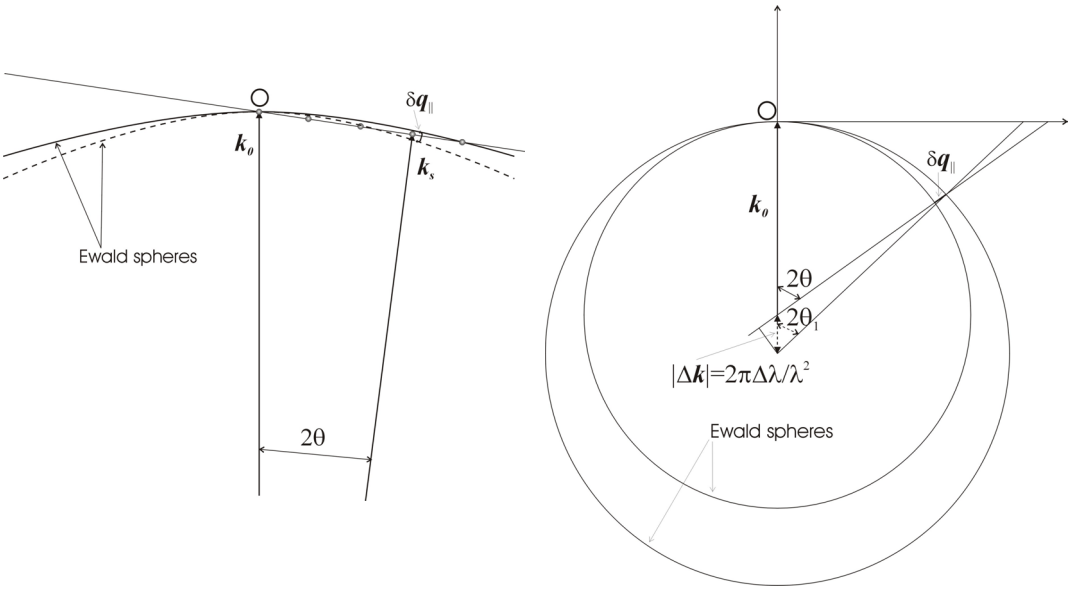

Fig. 2. 14. The influence of wavelength spread on the smearing of the Ewald sphere. A series of nodes of the reciprocal lattice of a crystal is also shown (left panel).

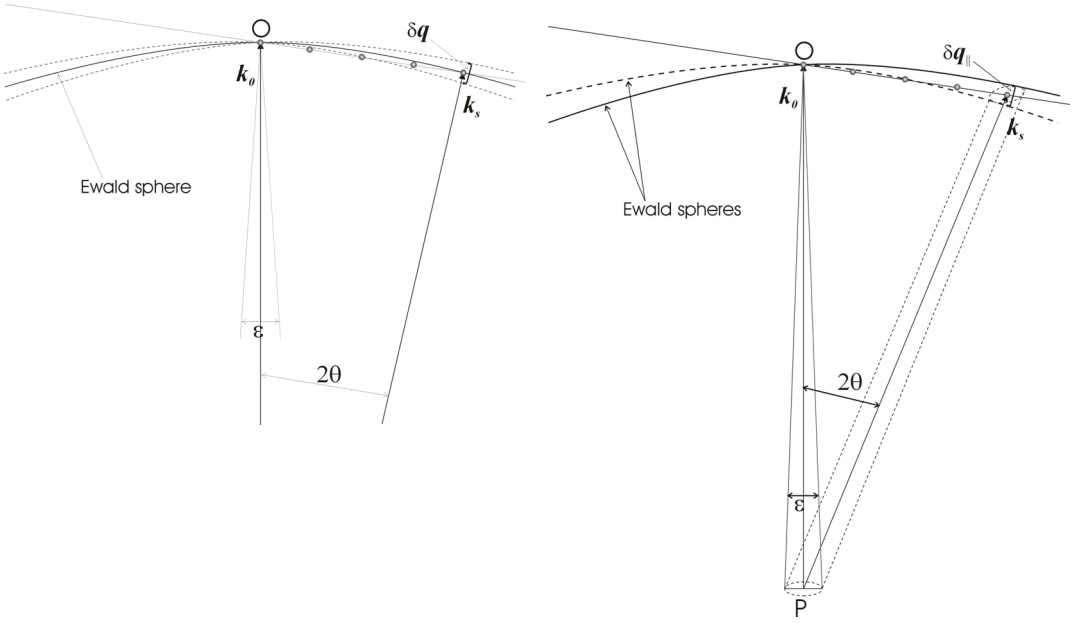

Fig. 2.15. The influence of the finite angular divergence of the beam on the smearing of the Ewald sphere.

Another contribution to the resolving power in the longitudinal direction comes from the fact that the incoming beam has a finite angular divergence, ε. As is schematically shown in Fig. 2.15 (right panel), in this case the starting points of the incoming wave vectors, **P**, would be distributed along a disk-shaped area in reciprocal space. Each point at that disk corresponds to an individually oriented Ewald sphere. For a given direction of scattered/diffracted waves, scattered vectors $\boldsymbol{k}_s$, drawn from points **P** of that disk would form the cross-section of the Ewald "*envelope*", which is also disk shaped. The finite (point-to-point) angular resolution of the detector would also smear that "*scattering disk*" further out. As can be seen in Fig. 2.15, the described effect also influences the resolution in reciprocal space in the direction along the scattered wave vector $\delta q_{||}$. In the case of small diffraction angles this is equal to $\delta q_{||,2} = q \cdot \varepsilon = k_0 \cdot 2\theta \cdot \varepsilon$.

In real space, it would manifest itself in some characteristic distance along the scattered wave vector, $\Lambda_{tr} = 2\pi / \delta q_{||,2} = \lambda / (\varepsilon \cdot 2\theta) = l_{tr} / 2\theta$, over which the waves, scattered at different points in a sample within the distance (in a transverse direction) defined by the transverse coherence length l_{tr}, diffract coherently as is sketched in Fig. 2.16.

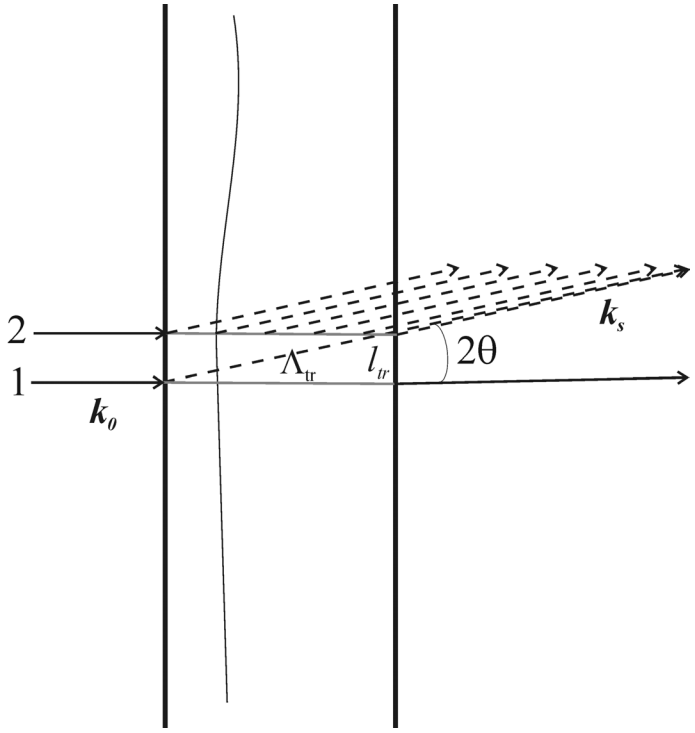

Fig. 2.16. A sketch illustrating how the finite transverse coherence length (in other words, the angular spread of the plane-wave components of the incoming wave field as it actually defines this length) may influence the longitudinal resolution.

As will be shown in Chapter 4, the typical angular range used in this work was about $10^{-3} \div 10^{-2}$ radians. Thus, taking into account only the natural angular divergence of the beam of 85 μrad one obtains an estimate of Λ_{tr} ~0.15 ÷ 1.5 mm (for 1.24 Å X-rays, beam energy of 10 keV), which was sufficient for the present study as will be discussed in Chapter 4.

2.5.3 Low-angle resolution

The achievable low-angle resolution defines the smallest scattering angle at which meaningful scattering data can be collected. It greatly depends on such an important factor as the amount of the parasitic scattering background relative to the typical strength of the sample scattering or diffraction. The background scattering is typically most harmful at the smallest scattering angles, where tails of the strong

direct beam could significantly contribute to the measured intensity, and at the largest scattering angles, where the sample scattering is usually weak. The parasitic scattering background can be reduced by careful alignment of the protective H5 and H6 guard slits. Note that one has to avoid the intense x-ray beam from touching the slits since that may result in a strong scattering originating from the slit edge. For weakly-scattering samples the scattering of the x-ray beam in air can become an important factor as well so that all air gaps have to be minimized in order to reduce the background unless the sample is not placed in a vacuum.

At a sample-detector distance of ~8 meter a Bragg spacing of ~4000 Å can typically be resolved with 10-12 keV X-rays at DUBBLE. By using an X-ray detector with sufficient spatial resolution and optimizing the whole setup, this can be improved. To illustrate the latter, Figure 2.17(b) shows the diffraction pattern of a body-centred tetragonal (bct) silica colloidal crystal. This unusual crystal structure is prepared by colloidal crystallization in an external electric field, and subsequent fixation in a polymer gel [15]. The nearest-neighbour distance is about 1.6 μm.

The results presented are obtained with a 12.38 keV (wavelength 0.1 nm) X-ray beam. X-ray diffraction is recorded by a CCD camera with a spatial resolution of ~55 μm (Sensicam, 1024×1024 pixels). The beam has been collimated and carefully focused onto the detector plane. The sample-detector distance was ~8.5 m. The lead beamstop used had a size of 5mm×5mm. To demonstrate the scale in the reciprocal space, Fig. 2.17(a) displays the fibre diffraction pattern of the dry rat tail collagen *(d*-spacings calibration sample). The white arrows point to the first-order diffraction peaks originating from the 65 nm long period of the collagen. The white arrow in Fig. 2.17(b) points to the lowest-order diffraction (110) peak corresponding to an interplanar spacing of d = 1.33 μm (as estimated from the diffraction pattern) in real space. This value compares well with the confocal microscopy result of d = 1.35 μm.

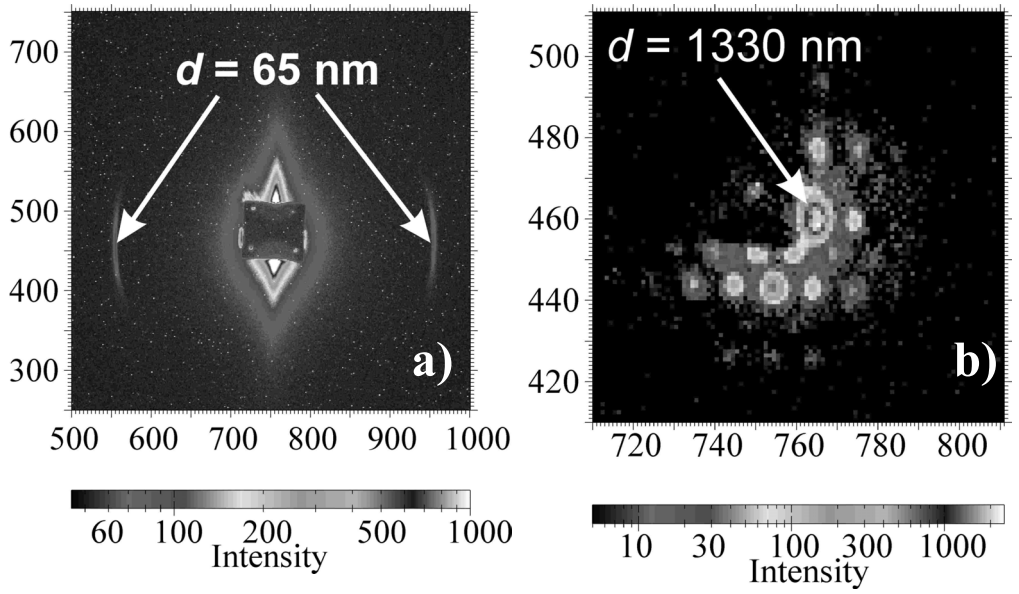

Fig. 2.17. (a): Diffraction pattern of dry rat tail collagen (the calibration sample ordinarily used in SAXS technique); (b): magnified (5 times relative to panel a) diffraction pattern of the bct colloidal crystal. Data weremeasured at DUBBLE by Jacob Hoogenboom, Arnout Imhof, Alfons van Blaaderen (soft condensed matter, University of Utrecht), Igor Dolbnya (DUBBLE) and Andrei Petukhov (van 't Hoff laboratory for physical and colloid chemistry, UU); the sample was provided by Job Thijssen (scm, UU).

Literature:

[1] Margaritondo G., *Introduction to synchrotron radiation* (Oxford University Press), 1986

[2] E.Vlieg, J. Appl.Cryst., **31,** 198 (1998).

[3] Freund A.K., Ishikawa T., Khounsary A.M., Mancini D.C., Michette A.G., Oestreich S., Proceedings of SPIE: Advances in X-ray optics, Vol. **4145** (2001), Bellingham, WA, USA

[4] A. Gabriel, F. Dauvergne, Nucl. Instr. Meth. **201,** 223 (1982).

[5] I.P. Dolbnya, H. Alberda, F.G. Hartjes, F. Udo, R.E. Bakker, M. Konijnenburg, E. Homan, I. Cerjak, P. Goedtkindt and W. Bras, Rev. Sci. Instrum. **73**, No. 11, 3754 (2002).

[6] Arndt U.W., J. Appl. Cryst., **19**, 145 (1986).

[7] Stanton M., Phillips W.C., Li Y., and Kalata K., J. Appl. Cryst., **25**, 549 (1992).

[8] Lewis R.A., Helsby W.I., Jones A.O., Hall C.J., Parker B., Sheldon J., Clifford P., Hillen M., Sumner I., Fore N.S., Jones R.W.M., Roberts K.M., Nucl. Instr. Meth. **A392** No.1, 32 (1997).

[9] A. Oed et al., Nucl. Instr. Meth. **A263,** 351 (1988).

[10] V. Zhukov et al., Nucl. Instr. Meth. **A392**, 83 (1997).

[11] E. Homan, M. Konijnenburg, C. Ferrero, R.E. Ghosh, I.P. Dolbnya, and W. Bras, J Appl. Crystallogr. **34** (Part 4) 519 (2001).

[12] R.W. James, *The Optical Principles of the Diffraction of X-rays* (Cornell University Press, Ithaca, New York, 1965); J.M. Cowley, *Diffraction Physics* (North-Holland, Amsterdam, 1981).

[13] M. Born and E. Wolf, *Principles of Optics* (Pergamon Press, Oxford, 1970).

[14] P.P. Ewald, Z. Krist. **56**, 129 (1921); P.P. Ewald, Proc. Phys. Soc. London, **52**, 167 (1940).

[15] A. Yethiraj and A. van Blaaderen, Nature **421**, 513 (2003).

Chapter 3

Theoretical aspects of small-angle diffraction for the study of colloids and colloidal crystals

3.1 Small-angle X-ray scattering and diffraction

Our starting point is the equation of electron motion in the external field of an incoming plane electromagnetic wave of frequency ω [1]:

$$m\dot{\boldsymbol{v}}' = e\boldsymbol{E} = e\boldsymbol{E}_0 \cdot e^{-i\omega t}, \qquad (3.1)$$

where $\boldsymbol{v}'$ is the additional velocity acquired by electron in the wave field.

Hence, $\boldsymbol{v}' = ie\boldsymbol{E}/m\omega$ and $\boldsymbol{r} = -e\boldsymbol{E}/m\omega^2$.

Let us define the electron number density function in a medium as $\rho(\boldsymbol{r})$.

The corresponding density of the current induced is $\boldsymbol{j}' = e\rho\boldsymbol{v}' = ie^2\rho(\boldsymbol{r})\boldsymbol{E}/m\omega$.

The microscopic/local Maxwell equations can be then written as follows:

$$rot\boldsymbol{E} = i\frac{\omega}{c}\boldsymbol{H}, \qquad (3.2)$$

$$rot\boldsymbol{H} = -i\frac{\omega}{c}\boldsymbol{E} + 4\pi\frac{\boldsymbol{j}'}{c} = -i\frac{\omega}{c}[1 - \frac{4\pi e^2\rho(\boldsymbol{r})}{m\omega^2})]\boldsymbol{E} = -i\frac{\omega}{c}\boldsymbol{D} = -i\frac{\omega}{c}\varepsilon\boldsymbol{E}, \qquad (3.3)$$

where ε is the dielectric constant which is now a function of coordinates within the medium. Note that all equations are given in Gaussian units.

At this point one needs to mention that electric field $\boldsymbol{E}$ describes now the *local* field inside the medium and can be represented as a vector sum of two parts: the field of the incident wave and a part due to scattering $\boldsymbol{E}=\boldsymbol{E}_0+\Delta\boldsymbol{E}_{sc}$.

Eliminating $\boldsymbol{H}$ from equations 3.2 and 3.3 one obtains:

$$rotrot\boldsymbol{E} = \frac{\omega^2}{c^2}\varepsilon\boldsymbol{E}$$

Using vector identity for a triple cross product

$$rotrot\boldsymbol{E} = \vec{\nabla}\times(\vec{\nabla}\times\boldsymbol{E}) = \vec{\nabla}(\vec{\nabla}\cdot\boldsymbol{E}) - \vec{\nabla}^2\boldsymbol{E},$$

and taking into account that *div***D**=0 as it follows from Eq. 3.3 (this is also consistent with the assumed high-frequency behavior), we obtain the classical wave equation in a medium:

$$\vec{\nabla}^2 \boldsymbol{E} + \frac{\omega^2}{c^2}\varepsilon \boldsymbol{E} = 0 \ , \tag{3.4}$$

which can be rewritten as:

$$\vec{\nabla}^2 \boldsymbol{E} + \frac{\omega^2}{c^2}\boldsymbol{E} = \frac{4\pi e^2 \rho(\boldsymbol{r})}{m\omega^2}(\boldsymbol{E_0} + \Delta \boldsymbol{E_{sc}}) = \frac{r_0 \lambda^2 \rho(\boldsymbol{r})}{\pi}\boldsymbol{E_0} + o(\Delta \boldsymbol{E_{sc}}) \ , \tag{3.5}$$

where $r_0=e^2/mc^2$ is the Thompson radius and λ the wavelength.

Here, the second term can be neglected as it is the product of a quite small quantity $\frac{r_0 \lambda^2 \rho(\boldsymbol{r})}{\pi}$ (typically of the order of 10^{-5}-10^{-6} in the X-ray wavelength range) and $\Delta \boldsymbol{E}_{sc}$ assumed to be small too as is required in a first approximation of perturbation theory. So, it is essential here that the the right-hand side of Eq. 3.5 under $\boldsymbol{E_0}$ we can use the given field of the incoming wave.

One may find the solution of Eq. 3.5 in a space outside the scattering medium at a large distance from it [1]:

$$\boldsymbol{E} = \frac{e^2}{m\omega^2}\frac{e^{ikR_0}}{R_0}[\boldsymbol{k}' \times [\boldsymbol{k}' \times \boldsymbol{E_0}]] \int \rho(\boldsymbol{r}) e^{-i\boldsymbol{qr}} dV \ , \tag{3.6}$$

where R_0 is the distance from the origin of coordinates inside the medium to the observation point, $\boldsymbol{q}$ is the scattering vector (momentum transfer) $\boldsymbol{q}=\boldsymbol{k}'-\boldsymbol{k}$, $\boldsymbol{k}$ and $\boldsymbol{k}'$ are incoming and scattered wave vectors, respectively, and k=k'=ω/c (elastic scattering).

From (3.6) the differential scattering cross-section can be written as:

$$d\sigma = r_0^2 \sin^2 \psi \left| \int \rho(\boldsymbol{r}) e^{-i\boldsymbol{qr}} dV \right|^2 d\Omega \, , \tag{3.7}$$

where $d\Omega$ is the solid angle, and ψ is the angle between the $\boldsymbol{E_0}$ and $\boldsymbol{k}'$ vectors.

It is clear that the intensity scattered in a certain direction is mainly determined by the square modulus of the integral $\int \rho(\boldsymbol{r}) e^{-i\boldsymbol{qr}} dV$, i.e. by the spatial Fourier transform component of the electron density. At $\boldsymbol{q} \to 0$ the integral simply gives the volume averaged electron density $\langle \rho \rangle$ and this would be in fact the case of ordinary *refraction* of X-rays in a medium with refraction index $n = \sqrt{\varepsilon}$. Thus, the scattering/diffraction at very small angles can be considered as refraction.

As known, atoms, molecules and even larger macroscopic formations (i.e. colloidal particles) may form ideal crystal structures in which they have definite positions in an extended regular array (lattice). So, let us assume now that the electron density in a medium is a spatial *periodic* function of coordinates. In that case, the electron density at any point can be expressed as a Fourier sum over the reciprocal lattice:

$$\rho(\boldsymbol{r}) = \sum_{b} A_b e^{i\boldsymbol{br}}, \qquad (3.8)$$

where the sum runs over all periods, $\boldsymbol{b}$, of the reciprocal lattice given by $\boldsymbol{b}_{hkl}=h\boldsymbol{b}_1+k\boldsymbol{b}_2+l\boldsymbol{b}_3$ where $\boldsymbol{b}_1$, $\boldsymbol{b}_2$, $\boldsymbol{b}_3$ are reciprocal lattice vectors defining the unit cell in reciprocal space (or in other notations $\boldsymbol{a}^*$, $\boldsymbol{b}^*$ and $\boldsymbol{c}^*$, respectively). *h, k, l* are the Miller indices of the reflection described by the reciprocal lattice point and A_b may be identified as the structure amplitude for the particular *hkl*-reflection. Conversely:

$A_b = \int_v \rho(\boldsymbol{r}) e^{-i\boldsymbol{br}} dv$, where integration is performed over the volume of the unit cell, *v*.

By substituting (3.8) into (3.7) one may realize that a notably non-zero result is only obtained at values of $\boldsymbol{q}$ close to some $\boldsymbol{b}$. Hence, we can consider each diffraction maximum individually and independently and assume that $\rho = A_b e^{i\boldsymbol{br}}$ with a fixed value of $\boldsymbol{b}$. By substituting this expression into Eq. (3.7) we end up with

$$d\sigma = r_0^2 \sin^2\psi \left|A_b\right|^2 \left|\int e^{-i(\boldsymbol{k'-k-b})\boldsymbol{r}} dV\right|^2 d\Omega .$$

As seen, the most intensive maxima appear in directions where the exact equality holds: $\boldsymbol{k'-k=b}$.

Since $|\boldsymbol{k'-k}|=2k\sin(\theta)$, where 2θ is the scattering angle (between the $\boldsymbol{k}$ and $\boldsymbol{k'}$ wave vectors), this then leads to the famous Bragg equation

$2k\sin(\theta)=b$,

which determines the diffraction angle of the main maximum.

3.2 Static lattice disorder

In this section we are guided by the theory developed by Guinier [2] and Wilson [3]. Partial extension has been made to include the case of different degrees of stacking disorder.

For a **perfect** crystal, a periodic three-dimensional (3D) lattice in object space has nodes which are defined by vectors $\vec{r}_n$, where *n* stands for the group of three integral numbers n_a, n_b, n_c. The corresponding reciprocal lattice has nodes at the extremities of vectors $\vec{b}_{hkl}$, *h,k,l* being Miller indices. Each lattice node corresponds to a unit cell which, by definition, repeats itself identically from node to node. This unit cell appears in the diffracted intensity calculations through its crystal structure amplitude (the square root of its structure factor):

$$A(\vec{q}) = \sum_i f_i(\vec{q}) \exp(-i\vec{q}\vec{u}_i),$$

for diffraction vector $\vec{q} = \vec{b}_{hkl}$, f_i is the "atomic" scattering factor (particle form-factor) and $\vec{u}_i$ is the vector connecting the lattice node to the *i*th particle. The summation runs over all particle positions in the unit cell.

For an **imperfect** crystal based upon a similar (average) lattice, the position and content of the unit cell corresponding to a given node depend on the node considered. Therefore, the structure amplitude is now different for each unit cell:

$$A_n(\vec{q}) = \sum_i f_{ni}(\vec{q}) \exp(-i\vec{q}\vec{u}_{ni}).$$

Now, particles might have different sizes ($f_{ni} \neq f_{n'i}$) or they can be displaced ($\vec{u}_{ni} \neq \vec{u}_{n'i}$). So, in one case the difference is the modulus of the terms of the above sum and in the other it is the argument. If the particles are all identical (monodisperse) and only simply displaced, A_n has a constant modulus and its phase alone varies:

$$A_n = f(\vec{q}) \exp(-i\vec{q}\Delta\vec{u}_n),$$

where $\Delta\vec{u}_n$ is the displacement of the *n*th particle from the corresponding node of the average lattice, chosen such that $\sum_n \Delta\vec{u}_n = 0$ for all the particles (="atoms") of the crystal. Once the structure amplitudes for each unit cell are defined, the scattering intensity for a crystal of volume V containing N unit cells can be calculated:

$$I_N(\vec{q}) = \sum_n \sum_{n'} A_n A_{n'}^* \exp[-i\vec{q}(\vec{r}_n - \vec{r}_{n'})] \qquad (3.9)$$

Introducing the notation $\vec{r}_m = \vec{r}_{n'} - \vec{r}_n$ where $m=n'-n$, or $m_a=n_a'-n_a$, $m_b=n_b'-n_b$, $m_c=n_c'-n_c$, the equation can then be rewritten as

$$I_N(\vec{\boldsymbol{q}}) = \sum_m \sum_n A_n A_{n+m}^* \exp(i\vec{\boldsymbol{q}}\vec{\boldsymbol{r}}_m) . \qquad (3.9a)$$

For a sufficiently large number, *p,* of unit cells the sum $\sum_n A_n A_{n+m}^*$ is nearly constant independent of which particular node is considered. Let us set

$$\overline{A_n A_{n+m}^*} = \frac{1}{p} \sum_{p \text{ unit cells}} A_n A_{n+m}^* = y_m .$$

To calculate the number of terms involved in the summation over *n*, let us now displace the original volume V by a distance $\boldsymbol{r}_m$. The volume common to two solids is then $\langle V \cdot V(\boldsymbol{r}_m) \rangle$, which basically represents the auto-correlation function of the shape of the object, $V(\boldsymbol{r}_m)$. The number of terms required is then equal to $V V(\boldsymbol{r}_m)/v_c$, where v_c is the volume of the unit cell of the average lattice. So, equation 3.9a can be rewritten as

$$I_N(\vec{\boldsymbol{q}}) = \frac{V}{v_c} \sum_m V(\vec{\boldsymbol{r}}_m) y_m \exp(i\vec{\boldsymbol{q}}\vec{\boldsymbol{r}}_m) .$$

The scattering power per unit cell is in fact

$$I_c(\vec{\boldsymbol{q}}) = \sum_m V(\vec{\boldsymbol{r}}_m) y_m \exp(i\vec{\boldsymbol{q}}\vec{\boldsymbol{r}}_m) . \qquad (3.10)$$

Let us now consider in more detail the situation where stacking faults appear in a close-packed structure. As is well known, the most compact arrangement of spheres is obtained by stacking hexagonal lattice planes in such a way that each sphere in a certain layer is in contact with three spheres in the neighboring layer, so that it is situated above the center of the equilateral triangle formed by the centers of these three spheres. There are two ways in which the second layer can be placed on the first one. As is depicted in Figure 3.1, the projection of a layer on the reference plane can take three different possible lateral positions A, B and C. The crystallographic hexagonal axes ***a*** and ***b*** (in the base layer/plane A), together with projections of the positions of C and B particles onto them, are also shown.

The two simplest arrangements which are periodic, and which can therefore give a crystal lattice, are the hexagonal close-packed arrangement ABAB…, and the face-centered cubic arrangement ABCABC… for which the hexagonal planes are the (111) planes. Since it is usually only the weak interaction between second neighbors which distinguish the hcp lattice from fcc, because the second layers are identical in

the first case (ABA) and different in the other (ABC), it is possible that such a compact lattice may contain stacking faults, a layer A being substituted for a layer B or C [2,3]. This displacement disorder is essentially a particular case of planar disorder.

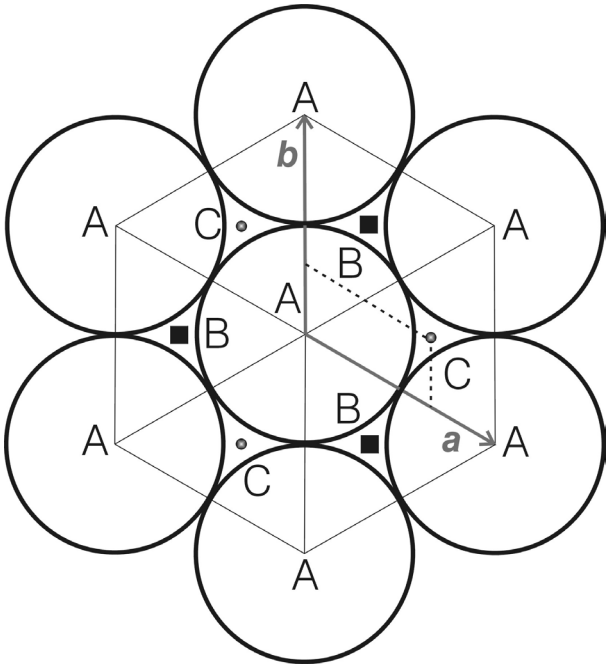

Figure 3.1. Close-packed arrangement of spherical particles. Shown: A, B and C – different possible positions of particles in three consecutive layers; ***a*** *and* ***b*** *– two in-plane crystallographic hexagonal axes.*

We define the crystal axes in such a way that the axis ***c*** is normal to the hexagonal planes. For planar disorder, the displacement $\Delta \boldsymbol{u}_n$ depends only on the plane where the nth unit cell is located, and therefore only on the parameter n_c (n along the **c**-axis). Thus

$$y_m = \left|\overline{A}_n\right|^2 y_{m_c} = \left|A\right|^2 y_{m_c} = \overline{A_n A_{n+m}^*} = \left|f\right|^2 \overline{\exp[i\vec{\boldsymbol{q}}(\Delta \boldsymbol{u}_{n_c+m_c} - \Delta \boldsymbol{u}_{n_c})]}$$

For simplicity, the vector $\boldsymbol{r}_m$ can be written in a manner to show its component along ***c***:

$$\boldsymbol{r}_{m_a m_b m_c} = \boldsymbol{r}_{m_a m_b 0} + \boldsymbol{r}_{00 m_c} = \boldsymbol{r}_{m_{ab}} + \boldsymbol{r}_{m_c}$$

The volume common to the two solids $V \cdot V(\boldsymbol{r}_m)$ is then equal to the product of the intersection surface area $S(\boldsymbol{r}_{m_{ab}})$ and the length $N_c c - |\boldsymbol{r}_{m_c}|$, or $(N_c - |m_c|)c$, where N_c is

the number of lattice planes (001) of which the crystal is formed and *c* denotes the lattice period in real space along axis ***c***. Thus, if *S* is defined as the surface cross-section area of the object, then $V=SN_c c$ and Eq. 3.10 can be rewritten as

$$I_c(\vec{\boldsymbol{q}}) = \left[|A|^2 \sum_{m_a} \sum_{m_b} \{S(\boldsymbol{r}_{m_{ab}})/S\} \exp(i\vec{\boldsymbol{q}}_{a^*b^*}\vec{\boldsymbol{r}}_{m_{ab}}) \right] \sum_{m_c} \left(1 - \frac{|m_c|}{N_c} \right) y_{m_c} \times \exp(i\vec{\boldsymbol{q}}_{c^*}\vec{\boldsymbol{r}}_{m_c}) \quad (3.11)$$

The first factor (in square brackets) is nothing else but the diffracted intensity from the two-dimensional plane lattice. It may be shown that around each node *hk0* and for sufficiently large cross-section area of the object *S* (large hexagonal planes), the integral scattering intensity value is defined by [2]

$$\int I(\vec{\boldsymbol{q}}) dq_a dq_b = \frac{A_{hk}^2}{s_c},$$

which can be interpreted as the product of the average value of the interference function, A_{hk}^2, by the surface of the reciprocal plane lattice unit cell (001), $1/s_c$. Thus, in reciprocal space the intensity diffracted by a 3D imperfect crystal is concentrated in columns whose cross-sections are the plane reflection domains surrounding the nodes of the base plane, and varies along the rows *hk* according the following law:

$$I_c(\vec{\boldsymbol{q}}) = \frac{|A|^2}{s_c} \sum_{m_c} \left(1 - \frac{|m_c|}{N_c} \right) y_{m_c} \exp(i\vec{\boldsymbol{q}}_{c^*}\vec{\boldsymbol{r}}_{m_c}).$$

We can now suppress the index *c* to simplify the notation. The period of the crystal reciprocal lattice along the axis ***c**** is equal to $2\pi/c$. By setting $\vec{\boldsymbol{q}}_{c^*} = 2\pi l/c$ and $\vec{\boldsymbol{r}}_{m_c} = mc$, the expression above is then can be rewritten as

$$I(l) = \frac{1}{s_c} \sum_{-N}^{+N} \left(1 - \frac{|m|}{N} \right) y_m \exp(2\pi i l m) \quad (3.12)$$

where *l* is the ordinate along ***c**** expressed in units of the lattice parameter $2\pi 1/c$ of the unit cell of the reciprocal lattice, *m* is an integer between –N and +N, N is the total number of hexagonal planes in the object, $y_m = |A|^2 y_{m_c}$ is the average of the product of the structure factors for two unit cells separated by distance *mc*, and *I(l)* is the scattering intensity along a row [001].

For close-packed crystals consisting of stacked hexagonal layers, the generic reciprocal lattice is sketched in Figure 3.2. The shadowed planes are parallel to the

hexagonal planes in the crystal. The hexagonal arrangement of the reciprocal space features is underlined by dashed lines.

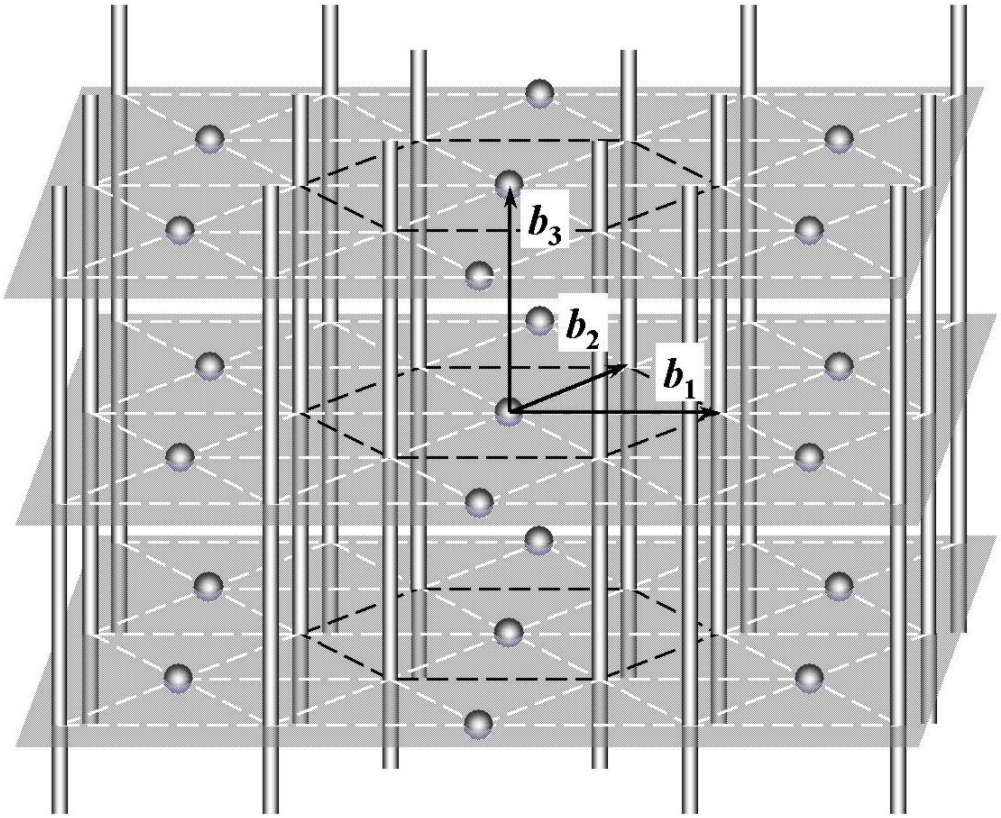

Figure 3.2. Reciprocal lattice of a random-hexagonal-close-packed crystal consisting of localized diffraction spots and rods. The shadowed planes, corresponding to integer values of l, are shown for illustration purposes only.

Let us now consider, in greater detail, the case of stacking faults when two regular arrangements are possible, namely hexagonal and cubic ones. First of all, we define the structure factor of the unit cell. The hexagonal axes in a reference plane are shown in Fig. 3.1. The first particle in layer A is placed at a corner of the unit cell, thus having coordinates (0,0,0) and a scattering factor *f*. The other second particle/atom of the unit cell is in layer C (or B) and has coordinates (2/3,1/3) in the hexagonal (*ab*) plane as can be deduced from Fig. 3.1. Because of the periodicity within the hexagonal layers the diffraction is only observed for integer values of *h* and *k*. Thus, the structure amplitude for a unit cell of layer C is

$$A_C = f\exp\left[-2\pi i(\frac{2h}{3}+\frac{k}{3})\right] = f\exp\left[-(2\pi ih-\frac{2\pi ih}{3})-\frac{2\pi ik}{3})\right] = f\exp\left[2\pi i(\frac{h-k}{3})\right] \tag{3.13}$$

Similarly, $A_B = f\exp\left[-2\pi i(\frac{h}{3}+\frac{2k}{3})\right] = A_C^*$ for layer B and, by definition, $A_A = f$.

Therefore, for *h-k* divisible by 3, diffraction is independent of the stacking order and is only observed for integer values of *l*. For other values of *h-k* the diffraction intensity sensitively depends on the probability, α, of finding an fcc-like stacking sequence among three consecutive layers within the crystal.

To calculate the average value y_m, let us introduce the probability P_m that two layers separated by distance *mc* are identical, then $1-P_m$ gives the probability that two layers are of the type AB or BA, AC or CA, BC or CB. The *m*th neighbor of a plane A would be planes A,B,C, which can be found in a proportions P_m, $(1-P_m)/2$ and $(1-P_m)/2$, respectively. At the same time, we have an equal number of A, B and C planes. Therefore

$$y_m = \frac{1}{3}A_A\left[P_m A_A^* + \frac{1-P_m}{2}\left(A_B^* + A_C^*\right)\right]$$
$$+\frac{1}{3}A_B\left[P_m A_B^* + \frac{1-P_m}{2}\left(A_A^* + A_C^*\right)\right]$$
$$+\frac{1}{3}A_C\left[P_m A_C^* + \frac{1-P_m}{2}\left(A_B^* + A_A^*\right)\right].$$

Using the values for structure amplitudes A_A, A_B, A_C, calculation gives

$$y_m = f^2\left[P_m + (1-P_m)\cos\left(2\pi\frac{h-k}{3}\right)\right],$$

and finally for $I(l)$ one obtains:

$$I(l) = \frac{f^2}{s_c}\left\{\cos\left(2\pi\frac{h-k}{3}\right)\sum_{-N}^{+N}\left(1-\frac{|m|}{N}\right)\exp(2\pi ilm)\right.$$
$$\left.+\left[1-\cos\left(2\pi\frac{h-k}{3}\right)\right]\sum_{-N}^{+N}\left(1-\frac{|m|}{N}\right)P_m\exp(2\pi ilm)\right\} \tag{3.14}$$

So, for rows having indices *hk* such that is *h-k* divisible by 3,

$$\cos\left(2\pi\frac{h-k}{3}\right)=1,$$

and we have nodes with the periodicity $1/c$ of a perfectly regular crystal containing N planes.

For the other rows

$$\cos\left(2\pi\frac{h-k}{3}\right)=\frac{-1}{2},$$

and one obtains

$$I(l)=\frac{3f^2}{2s_c}\sum_{-\infty}^{+\infty}P_m\exp(2\pi ilm)-\frac{f^2}{2s_c}\sum_{-\infty}^{+\infty}\exp(2\pi ilm), \qquad (3.15)$$

here the object size effect is neglected ($\frac{|m|}{N}\to 0$), which is valid under the assumption that the crystal is large enough.

In a situation when the layers are arranged at random, P_m tends to 1/3 for a large value of m considered. Under the assumption that the interaction is limited only to neighboring layers, for a given layer we can find two different neighboring layers with an equal probability. If that layer is A, the probability that the (m-1)th layer would be B or C is (1-P_{m-1}), and there is only one chance out of two that the next mth layer would be A. Therefore, we can write the following recurrence relation:

$P_m=(1-P_{m-1})/2$.

By setting $P_m=1/3+q\rho^{|m|}$, one may solve this equation and find that [2]

$P_m=1/3+2/3(-1/2)^{|m|}$.

Then the scattering intensity is

$$I(l)=\frac{f^2}{s_c}\sum_{-\infty}^{+\infty}\left(-\frac{1}{2}\right)^{|m|}\exp(2\pi ilm) \qquad (3.16)$$

The above summation gives

$$I(l)=\frac{f^2}{s_c}\frac{3/4}{(5/4)+\cos 2\pi l}$$

The intensity has large maxima at $l=i+(1/2)$, and minima at $l=i$, where i is an integer. This is the greatest disorder which can exist in a close-packed arrangement.

Considering now a *close-packed hexagonal* lattice under the assumption that the probability of faults is small enough [2], then after the pair AB one should generally find a layer A. However, there is a *small* probability α of finding C. If the first layer is A, we define again the probability P_m that the mth layer will be also A. I have A in the mth layer if (m-2)th layer is A and if there are no faults, since we have the series ABA or ACA. The probability for this is $(1-\alpha)P_{m-2}$. One may also have a fault (BCA or CBA) with A neither in the (m-2)th layer nor in the (m-1)th. The probability for this is $\alpha(1-P_{m-2}-P_{m-1})$. Thus

$P_m=(1-\alpha)P_{m-2}+\alpha(1-P_{m-2}-P_{m-1})$

or

$P_m+\alpha P_{m-1}+(2\alpha-1)P_{m-2}=\alpha.$

This equation can be solved by setting $P_m=(1/3)+q\rho^{|m|}$, if [2]

$\rho^2+\alpha\rho-1+2\alpha=0.$

To satisfy the initial conditions $P_0=1$, $P_1=0$, it is necessary to use two roots of the above equation and, neglecting higher powers of $\alpha\rho^{|m|}$, finally one may obtain

$$P_m=\frac{1}{3}+\frac{1}{6}\left(1-\frac{3}{2}\alpha\right)^{|m|}+\frac{1}{2}\left(-\left(1-\frac{\alpha}{2}\right)\right)^{|m|}.$$

To summarize, the scattering intensity, using Eq. 3.15, is given by

$$I(l)=\frac{f^2}{s_c}\left\{\frac{1}{4}\sum_{-\infty}^{+\infty}\left(1-\frac{3}{2}\alpha\right)^{|m|}\exp(2\pi ilm)+\frac{3}{4}\sum_{-\infty}^{+\infty}\left(\frac{\alpha}{2}-1\right)^{|m|}\exp(2\pi ilm)\right\} \quad (3.17)$$

Using the symmetry properties of the *sin* and *cos* functions this expression can be reduced to the following form:

$$I(l)=\frac{f^2}{s_c}\left\{1+\frac{1}{2}\sum_{1}^{+\infty}\left(1-\frac{3}{2}\alpha\right)^{m}\cos(2\pi lm)+1+\frac{3}{2}\sum_{1}^{+\infty}\left(\frac{\alpha}{2}-1\right)^{m}\cos(2\pi lm)\right\}=$$

$$=\frac{f^2}{s_c}\left\{2+\frac{1}{2}\sum_{1}^{+\infty}\cos(2\pi lm)\left[\left(1-\frac{3}{2}\alpha\right)^{m}+3\left(\frac{\alpha}{2}-1\right)^{m}\right]\right\} \quad (3.18)$$

The analogous approach may be used to treat the face-centered cubic lattice containing a few rare faults. Omitting the details, let us reproduce the final expression for the intensity scattered on the rows $h-k\neq 3n$, where n is integer:

$$I(l) = \frac{f^2}{s_c}\left\{\sum_{-\infty}^{+\infty}(1-\beta)^{|m|}\cos\frac{2\pi m}{3}\exp(2\pi i l m)\right\} =$$
$$= \frac{f^2}{2s_c}\left\{\sum_{-\infty}^{+\infty}(1-\beta)^{|m|}\exp\left[2\pi i\left(l+\frac{1}{3}\right)m\right]+\right.$$
$$\left.+\frac{f^2}{2s_c}\sum_{-\infty}^{+\infty}(1-\beta)^{|m|}\exp\left[2\pi i\left(l-\frac{1}{3}\right)m\right]\right\}, \qquad (3.19)$$

here the coefficient α is replaced with (1-β), β is being small. There are two series of maxima of equal intensity corresponding to $l = i \pm (1/3)$, where i is integer.

To summarize, Fig. 3.3 demonstrates the results of simulations for different values of the coefficient α in the range $-1 < l < +1$. The black bold curve corresponds to α=0.5, i.e. the case when stacking order is absent. In this case, two broad maxima at l=-0.5 and l=0.5 can be observed.

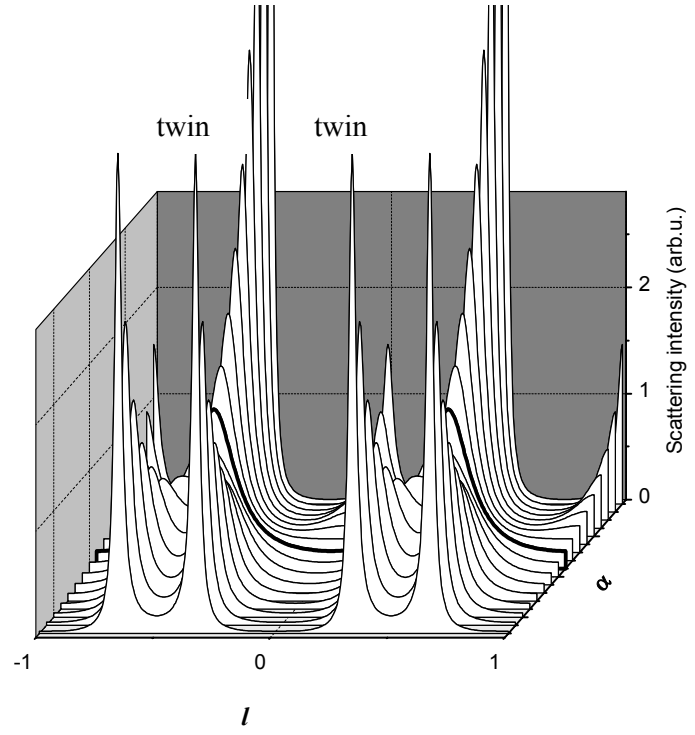

Figure 3.3. Theoretical distribution of the scattering intensity calculated in the range of –1 < l < 1 for different values of fcc-like stacking probability coefficient α ($0.1 \le \alpha \le 0.9$, in steps of 0.05).

The curve in front of the figure corresponds to mainly fcc stacking with probability

α = 0.9. The scattering intensity along the rod is then mostly concentrated near the diffraction spots corresponding to l = 2/3,1/3,-1/3,-2/3 of twin fcc crystals of an ABCABC lattice and of its symmetric ACBACB lattice.

We have so far considered only the so-called *growth faults* when the crystal is formed by the stacking of successive planes. Another type of faults, *distortion faults*, can be also considered, starting with perfect fcc crystal ABCABC… and assuming that the distortion has the effect of slipping one plane. Thereby, it will change one type of stacking sequence to another while preserving the sequence for the other planes. This type of fault therefore never give rise to twinning, as in growth faults.

3.3 "Time-dependent" lattice disorder

There is another, time-dependent, type of crystal lattice disorder due to the thermal vibrations of particles around their average lattice sites. The period of vibrations is short compared to the duration of any feasible/realizable diffraction experiment in which the intensity is measured, but very long compared to the period of X-rays. Therefore, the observed intensity is the average of diffracted intensities for all possible configurations of particles. Each particle moves according to a single statistical law and, at a given moment, the displacements of different particles are statistically identical to displacements of a given particle taken at arbitrary moments separated by time intervals large enough compared to the period of vibrations. Then, the average values of displacement vectors $\Delta\boldsymbol{x}_n$ for all the particles at a given instant are identical to the average values of $\Delta\boldsymbol{x}_n$ in time, for a given nth particle. If Δx_{1n} is the projection of $\Delta\boldsymbol{x}_n$ on the direction of scattering vector $\boldsymbol{q}$, then let us define Δx_{2n} and Δx_{3n} to be the projections of vector $\Delta\boldsymbol{x}_n$ on two other axes such that all three axes are orthogonal. It may be then written

$\Delta x_n^2 = \Delta x_{1n}^2 + \Delta x_{2n}^2 + \Delta x_{3n}^2$.

If the displacements of particle are perfectly isotropic around the lattice node, the averages $\langle\Delta x_{1n}^2\rangle$, $\langle\Delta x_{2n}^2\rangle$, $\langle\Delta x_{3n}^2\rangle$ are equal and

$3\langle\Delta x_{1n}^2\rangle = \langle\Delta x_n^2\rangle = b^2$,

if we set b as the quadratic average of $|\Delta\boldsymbol{x}_n|$.

In an approximation of statistically independent (uncorrelated) fluctuations, one may then assume that the time-averaged electron density distribution function at every lattice point can be obtained by "diffusing" the particle with the Gaussian function with rms width $<\Delta x_{1n}^2>$:

$$\langle \rho(\vec{\boldsymbol{r}}) \rangle_t = \sum_l \sum_m \sum_n \delta\left\{\vec{\boldsymbol{r}} - (l\vec{\boldsymbol{a}} + m\vec{\boldsymbol{b}} + n\vec{\boldsymbol{c}})\right\} \otimes \left[\rho_0(\vec{\boldsymbol{r}}) \otimes \frac{1}{\sqrt{2\pi < \Delta x_{1n}{}^2 >}} \exp\left(\frac{-|\vec{\boldsymbol{r}}|^2}{2 < \Delta x_{1n}{}^2 >} \right) \right] \tag{3.20}$$

where $\rho_0(\boldsymbol{r})$ is the electron density distribution function of particle, symbol δ denotes the Dirac delta-function and symbol $\otimes$ stands for convolution. Taking the Fourier transform, we thus obtain for the structural amplitudes:

$$\langle A \rangle_t = A_0(\vec{\boldsymbol{q}}) \sum_h \sum_k \sum_l \delta\left\{\vec{\boldsymbol{q}} - (h\vec{\boldsymbol{b}}_1 + k\vec{\boldsymbol{b}}_2 + l\vec{\boldsymbol{b}}_3)\right\} \exp\left(- < \Delta x_{1n}{}^2 >^2 \boldsymbol{q}^2 / 2 \right)$$

and for the intensity per unit cell

$$\langle A \rangle_t{}^2 = \left| A_0(\vec{\boldsymbol{q}}) \right|^2 \exp\left(\frac{-b^2 \boldsymbol{q}^2}{3} \right) \sum_h \sum_k \sum_l \delta\left\{\vec{\boldsymbol{q}} - (h\vec{\boldsymbol{b}}_1 + k\vec{\boldsymbol{b}}_2 + l\vec{\boldsymbol{b}}_3)\right\} \tag{3.21}$$

Therefore, as one may see from the expression above, the intensities of Bragg reflections are decreasing with increasing the wavevector transfer, $\boldsymbol{q}$, proportional to the Debye-Waller factor $\exp\left(-b^2 \boldsymbol{q}^2 / 3\right)$.

3.4 Conclusion

In this Chapter we have treated the types of displacement disorders most relevant to the work presented here. There are several extensions to the theory possible. For instance, in case of crystals composed by atoms or particles of different sort (size, for example) there can be another type of disorder: substitutional disorder. The combination of substituonal and displacement disorders is also possible. Various types of defects and imperfections such as point and line defects, vacancies, dislocations may also exist. The defects may deteriorate or even destroy the long-range order in a crystal. These will not be treated extensively here. The interested reader is refered to the classical book by A. Guinier [2].

Literature:

[1] Landau L.D. and Lifshitz, *Electrodynamics of continuous media* (Pergamon, Oxford, 1960)

[2] A. Guinier, *X-ray Diffraction in Crystals, Imperfect Crystals, and Amorphous Bodies* (W.H. Freeman and Company, San Francisco and London, 1963).

[3] O.S. Edwards and H. Lipson, Proc. Roy. Soc. A **180**, 268 (1941); A.J.C. Wilson, *ibid*, **180**, 277 (1941); A.J.C. Wilson, *X-Ray Optics* (Methuen & Co. Ltd., London, 1949).

[4] R.W. James, *The Optical Principles of the Diffraction of X-rays* (Cornell University Press, Ithaca, New York, 1965); J.M. Cowley, *Diffraction Physics* (North-Holland, Amsterdam, 1981).

Chapter 4

Diffraction studies of order parameters in silica hard-sphere colloidal crystals

4.1 Experimental

A typical example of a colloidal hard-sphere crystal is shown in Figure 4.1(a). The sample is oriented such as to display a clear Bragg reflection of green light from one of the crystals, which typically grow in the concentrated sediment within 1-2 weeks after sedimentation from the top of the sediment.

The sample was prepared by sedimenting a dilute 5% volume fraction colloid suspension in a flat glass capillary of internal path length of 0.2 mm. The silica spheres of 224 nm diameter and 4.1% size polydispersity were covered with 2 nm thin hydrocarbon layers to prevent their agglomeration in the cyclohexane solvent [1]. Osmotic compression by adding non-adsorbing polymer (polydimethylsiloxane, 14 nm radius of gyration, at volume fractions of polymer coils ϕ_p of 10-15% around the phase separation boundary [2]) to the suspension is observed to accelerate crystallization and to give large high-quality crystals, which have been selected for the present study. In addition, reference samples without polymer have also been used.

Small angle X-ray diffraction measurements have been performed at the Dutch-Flemish bending magnet BM26B "DUBBLE" beam line at the European Synchrotron Radiation Facility (ESRF) in Grenoble (France). The scattering of a 10 keV X-ray beam (wavelength λ=1.24 Å, band pass $\Delta\lambda/\lambda=2\cdot10^{-4}$, size 0.1×0.1 mm^2 at the sample) has been registered at ~8 meters distance from the sample by a two-dimensional (512×512 pixels) gas-filled proportional detector [3]. The samples have been mounted on a goniometer head, which allows for careful orientation around three orthogonal axes.

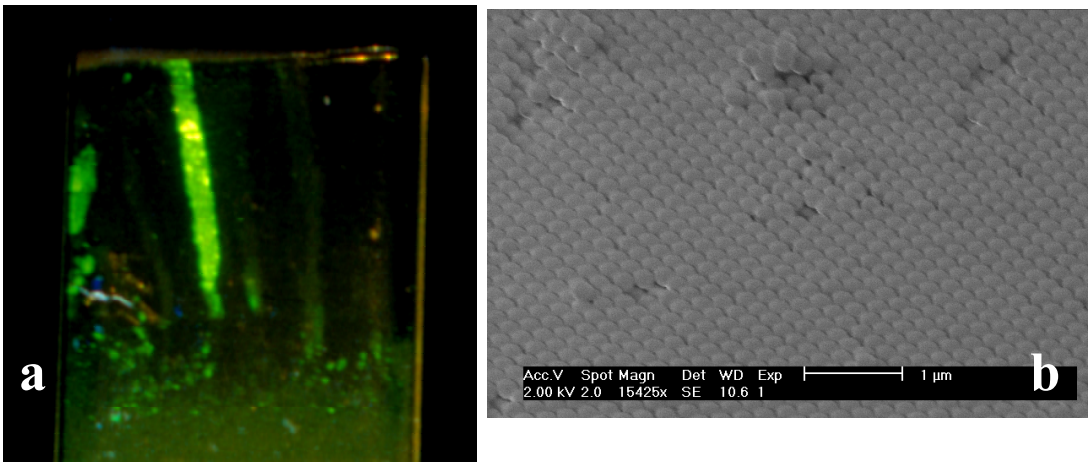

Figure 4.1. (a) Photograph of a typical sample with hard-sphere silica colloidal crystals in a flat glass capillary. (b) Scanning electron microscope image of a crystalline area in a dried sample.

4.2 Single-crystal X-ray diffraction

A carefully oriented sample gives a diffraction pattern as in Figure 4.2(b). The orientation of the sample with respect to the incoming wave vector is schematically depicted in Figure 4.2(a). The laboratory *x,y,z* coordinate frame is also depicted.

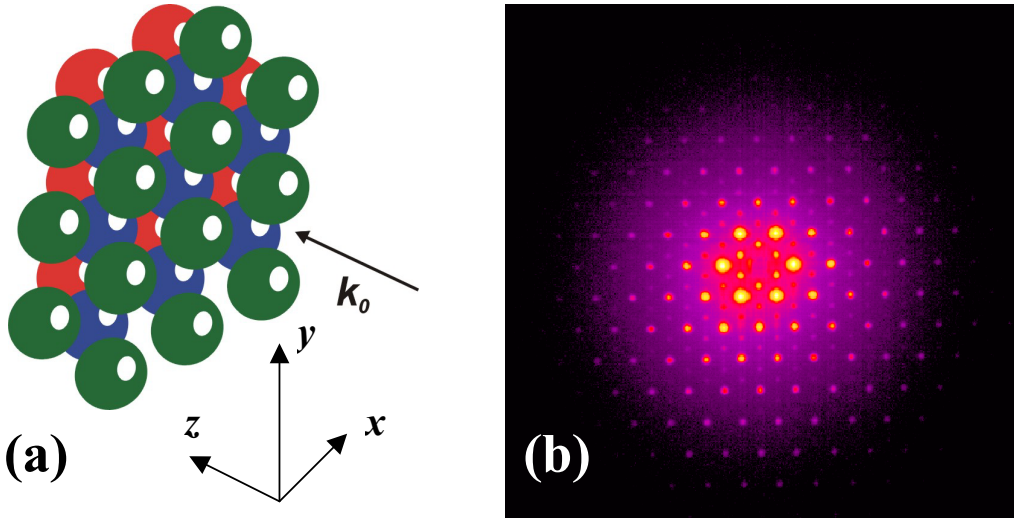

Figure 4.2. (a) Sketch illustrating the orientation of the sample with respect to the incoming beam. Three successive hexagonal layers of spherical silica particles are shown. The hexagonal layers are normal to the incoming wave vector $\mathbf{k_0}$ *leading to a diffraction pattern as the one shown in (b).*

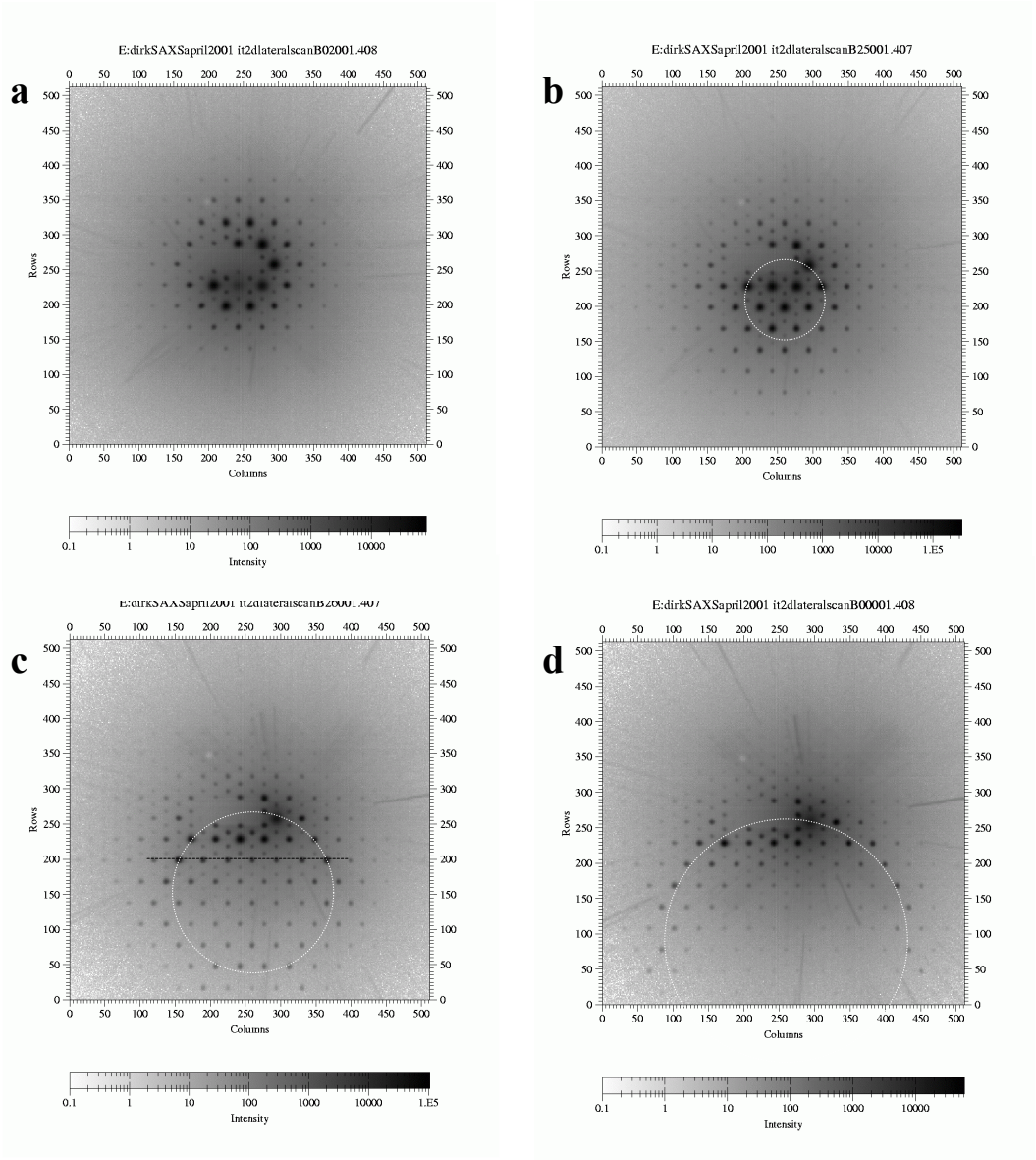

Figure 4.3. Diffraction patterns taken at different rocking angles ξ around the horizontal x axis parallel to the detector: (a) $\xi \sim 0°$, (b) $\xi = 0.1°$, (c) $\xi = 0.2°$ and (d) $\xi = 0.3°$. Patterns are taken approximately in the middle of the crystal.

The diffracted intensity can be written as a product of the structure factor $\Sigma(\boldsymbol{q})$, which is the result of the diffraction of the periodic lattice of a single crystal, and the square of the form factor f($\boldsymbol{q}$) representing the intra-particle scattering:

$$I(\boldsymbol{q}) = \Sigma(\boldsymbol{q}) |f(\boldsymbol{q})|^2 .$$

The predominantly hexagonal features of the pattern are a consequence of the Fourier transformed electron density of hexagonally packed planes of spheres within the crystal normal to the beam (see Figure 4.2).

4.3 Positional and orientational order

Figure 4.3 illustrates the extreme sensitivity of the diffraction pattern to the sample tilt (rotations by less than 0.1° show changes in the diffraction pattern which are easily detected). The size of the diffraction pattern spots is dominated by the spatial resolution of the detector and the limited coherence in the transverse direction (as discussed in Section 2.4). However, our results shown in Fig. 4.3 do allow evaluation of the positional order in the longitudinal direction.

Fig. 4.4 is a sketch demonstrating how the diffraction patterns, shown in Fig. 4.3, can be visualized by applying the Ewald sphere construction in reciprocal space [4,5]. Diffraction is only observed whenever the Ewald sphere crosses a node of the reciprocal lattice.

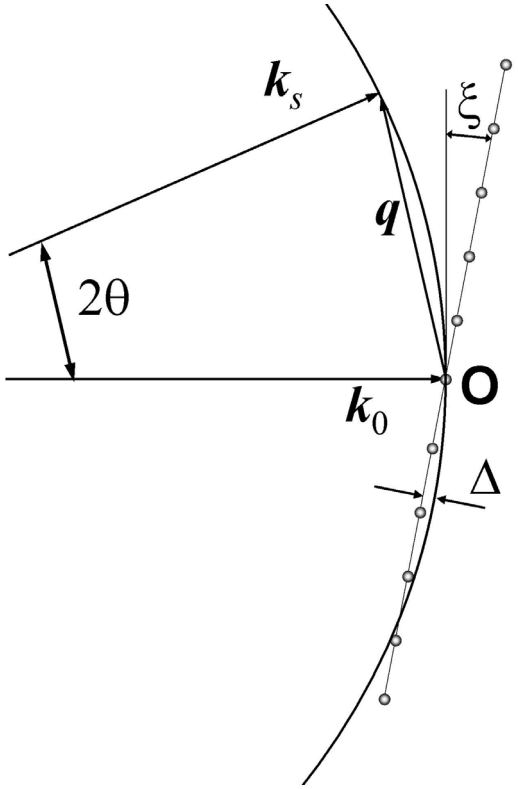

Figure 4.4. A sketch of the intersection of the Ewald sphere through a set of reflections in reciprocal space for a tilted sample. The curvature of the Ewald sphere is greatly enhanced for clarity. In reality the radius of the Ewald sphere is larger and the cut is nearly planar. O denotes the origin of the reciprocal space.

Since in the SAXS regime scattering angles are very small (within the detector area of Fig. 4.3 $2\theta < \sim 14$ mrad) and periods of the reciprocal lattice are much smaller than the radius

of the Ewald sphere $|\boldsymbol{k}_0|$, the relevant part of the Ewald sphere is nearly flat. However, its curvature clearly reveals itself in the diffraction patterns shown in Fig. 4.3 leading to a strongly asymmetric pattern with much brighter diffraction peaks in the bottom part of the detector.

For the tilted sample the Ewald sphere intersects the plane of the reciprocal lattice reflections along a circle. The center of this circle is at $2\theta=\xi$ (see Fig. 4.4), where for $\xi=0.2°$ the Ewald sphere deviates from the plane by as little as $\Delta=(1-\cos\xi)k_0=6\cdot10^{-6}k_0$. However, the intensity of the diffraction spots here is very much reduced due to the mismatch suggesting that the reciprocal lattice spots are much smaller than Δ. To determine the size dq of the reciprocal lattice spots we show in Fig. 4.5 the profile of the structure factor obtained after dividing out the form factor $|f(\boldsymbol{q})|^2$ along a row of diffraction peaks indicated in Fig. 4.3(c) by the black dashed line.

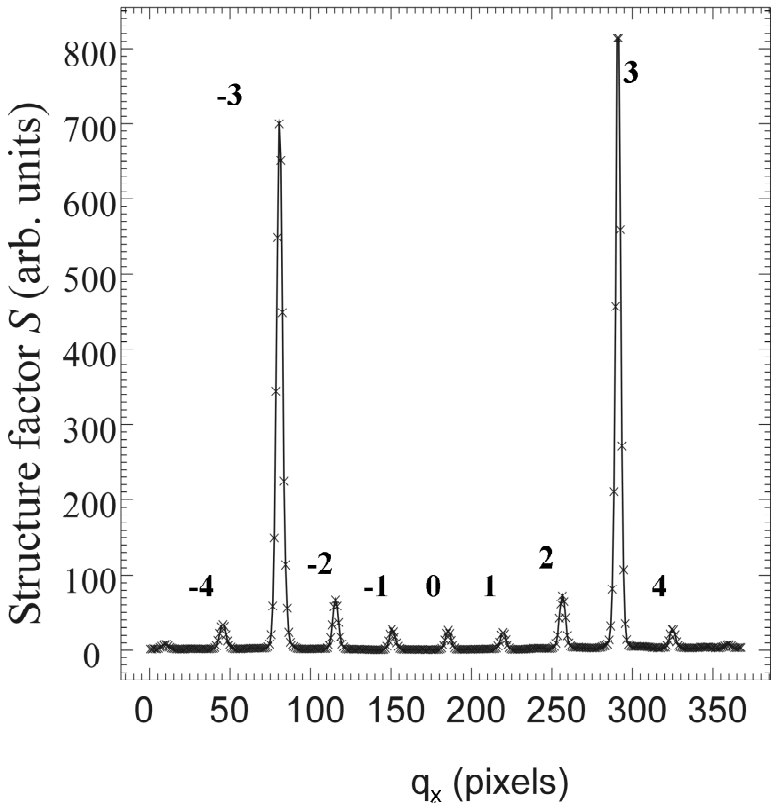

Figure 4.5. Variation of the structure factor along the line, indicated by the black dashed line in Fig. 4.3(c).

Two very strong reflections (denoted as 3 and -3) are closest to the Ewald sphere for this sample orientation. For the neighboring reflections ±2 and ±4 the mismatch from the Ewald

sphere amounts to $2\cdot10^{-6}k_0$ and $3\cdot10^{-6}k_0$, respectively. They are seen in Fig. 4.5 to be weaker than the brightest ±3 reflections by at least one order of magnitude indicating that the width of the reciprocal lattice spots dq is smaller than $10^{-6}k_0$. The inverse of this width $\Lambda_{corr}=2\pi/\mathrm{d}q$ translates into a positional correlation [5,6] between at least 500 crystal layers along the beam. We thus find high positional order, possibly ranging over the entire sample thickness (the thickness of the capillary allows to accommodate about 1000 layers). Whereas here the spatial extent, Λ_{corr}, of the positional order is evaluated by comparing the diffraction intensity of peaks of different order within a single diffraction pattern, a similar estimate of Λ_{corr} can be obtained by measuring the rocking curve, i.e. the dependence of the intensity $I_{(hkl)}$ of a particular (hkl) reflection on the sample tilt angle ξ. This evaluation yields a similar result. To summarize, a resolution in reciprocal space of order $\mathrm{d}q=10^{-6}k_0$ is demonstrated with synchrotron small-angle x-ray diffraction on colloidal crystals. The use of the single-crystal diffraction technique is crucial in obtaining such a resolution, which is much more difficult to achieve in powder diffraction [7,8]. The data presented in Figs. 4.3 and 4.5 do not allow for a similar determination of the in-plane positional order correlation length (in the transverse direction). However, as will be shown in Section 4.4, the crystal possesses high in-plane positional order as well.

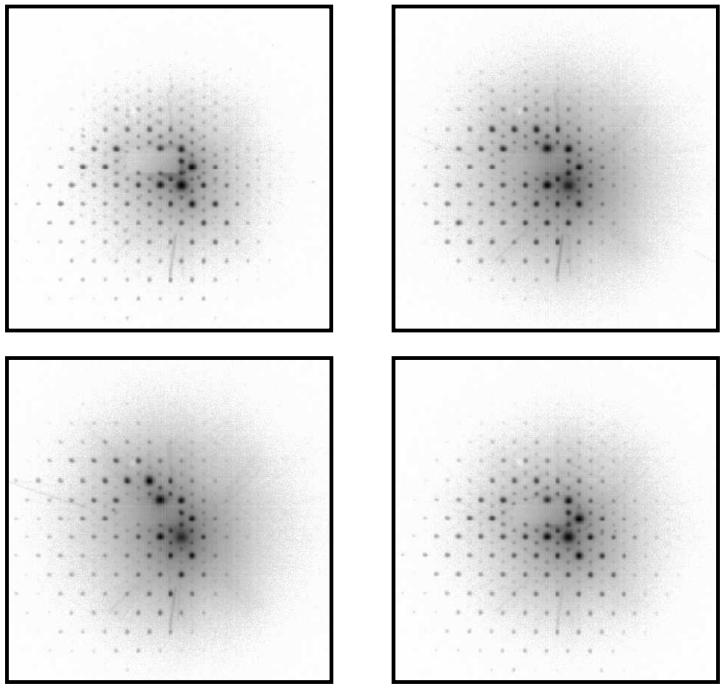

Figure 4.6. Examples of diffraction patterns of one crystal monodomain taken at various positions in the sample (separated by up to 0.35 mm horizontally and 1 mm vertically).

Figure 4.3 illustrates that scattering patterns are extremely sensitive to out-of-plane rotation (of 0.1° or even less) around the horizontal x axis (see Fig. 4.2). This axis corresponds to the direction of polarization of the incoming X-ray beam. A similar extreme sensitivity is observed for crystal rotations around the y axis. This allowed us to carefully follow the out-of-plane orientation of the crystal while translating it laterally. It has been observed that the pattern does not change noticeably upon translating the sample vertically and horizontally indicating a very high degree of orientational order within this single crystal area of size $0.5\times1\times0.2$ mm^3 ($x\times y\times z$), surrounded by crystals with other orientations. The latter is illustrated in Fig. 4.6. This high orientational order suggests a high rigidity of the crystal planes, which are flat within a sphere diameter over a distance comparable to the crystal size.

4.4 Stacking order/disorder and direct visualization of Bragg rods

Monte Carlo simulations have indicated that colloidal hard spheres favor a face centered cubic (fcc) crystal as a close-packed structure [9]. However, experimentally it is found that a random hexagonal close packing (rhcp) structure is more common [8,10-13], either as a transient state or possibly even permanently. This could be due to for instance size polydispersity which can readily influence the small free energy differences involved. Therefore, simulations might be incomplete since they do not take this into account. As has been shown in Chapter 3, due to irregular stacking of hexagonal layers in the three possible lateral positions, some features in the reciprocal lattice of their rhcp structure are smeared out into *Bragg scattering rods* [14,15] in the direction perpendicular to the hexagonal layers (Figs. 3.2). Periodicities common to all layers lead to sharp *Bragg spots*.

The results presented in Fig. 4.3 correspond to the case $l\approx0$. Larger rotations of the sample around an in-plane axis give different intersections (at larger l) between the reciprocal lattice and the Ewald sphere. This enables one to experimentally measure the intensity profile along the rods and, thus, to determine the stacking order of consecutive hexagonal planes. In Fig. 4.7 the structure factor for a sample rotated by an angle of 9.5°, around the vertical in-plane axis, is shown.

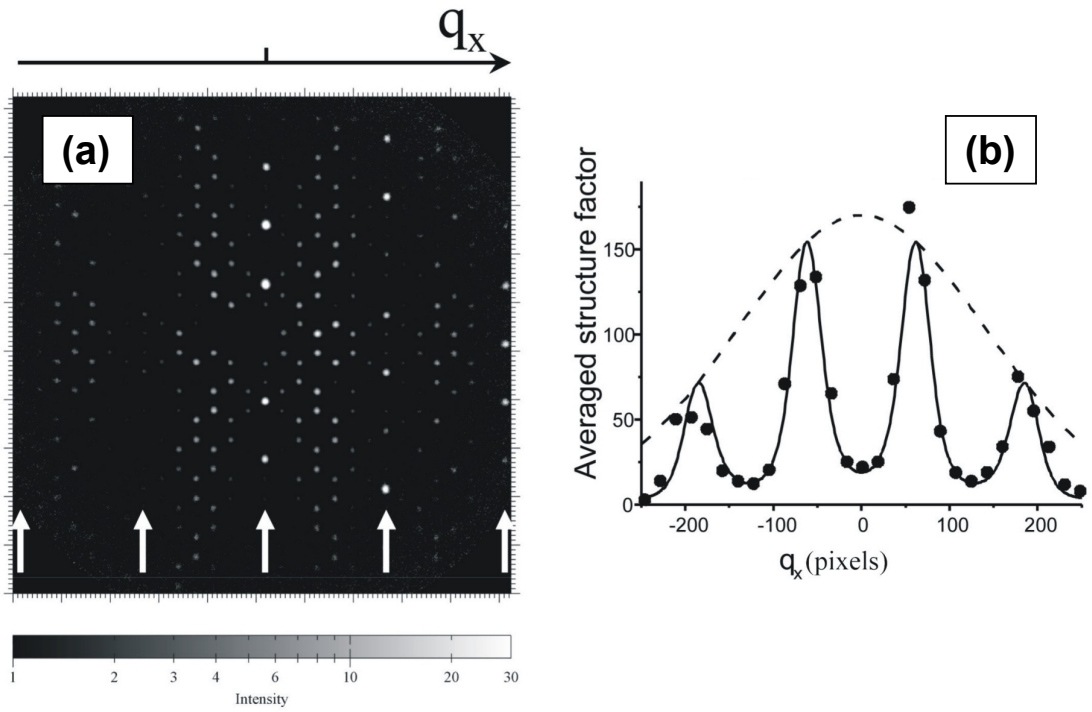

Figure 4.7. (a) Structure factor after the sample is rotated by 9.5° around the vertical axis relative to its orientation shown in Fig. 4.3(a). (b) Horizontal variation of rod intensities in (a). The solid line displays the result of calculations for α=0.55 multiplied by a Debye-Waller factor (shown by the dashed line).

The corresponding Ewald sphere cuts through the origin of reciprocal space and intersects 5 planes of spots corresponding to l= 0, ±1, ±2 (at q_x indicated by arrows in Fig. 4.7(a)) within the range of scattering angles presented at the detector, leading to vertical lines of bright diffraction peaks. Again, note the asymmetry (stronger on the right, vanishing on the left) of the relative intensity of these peaks across the entire diffraction pattern. The additional pattern in between the rows of diffraction spots is formed by intersections with rods. This pattern is symmetric since the curvature of the Ewald sphere does not play any role here; it only very slightly shifts the point of intersection along the rod with its smoothly varying intensity profile. By vertically averaging the intensities of the rod pattern we get a representation of the intensity variation along the length of the rods. As shown in Fig. 4.7(b), this corresponds closely to a stacking parameter α= 0.55±0.05; i.e., the case where the crystal possesses no stacking order. The experimental data shown in Fig. 4.7(b) were fitted by the theoretical intensity modulation curve (section 3.2 of this thesis and Ref. [14,15]) multiplied by a Gaussian function. The latter corresponds to the ordinary Debye-Waller factor in crystals, which accounts for the thermal fluctuations in the particle positions around the average lattice

positions [5,15,16] that has been introduced in Section 3.3. This effect, however, is not related to the stacking disorder discussed in this Chapter. A positional fluctuation of about 2% of the sphere diameter is consistently found, which can be compared to the average nearest neighbor distance that is about (3±1)% larger than the sphere diameter as determined from diffraction patterns. Within 1% accuracy the same nearest neighbor distance is found at all heights.

With the same set of samples two similar x-ray diffraction studies have been performed, two weeks after crystallization and a year later. The results shown in Figures 4.3 and 4.7 have been obtained in the second measurement session. The earlier experiment already indicated the presence of high positional order in the crystals. The degree of the stacking disorder remained the same within one year. A similar study has been performed on reference samples without non-absorbing polymer. Except for a smaller typical crystal size leading to difficulties in exploring the three-dimensional reciprocal properties by crystal rotation, the results indicate the presence of long-range positional order and stacking disorder in the polymer-free samples.

We also note that in the previous section the spatial extent of the positional order was determined from the analysis of the intensities of the localized Bragg spots. Alternatively, one can evaluate Λ_{corr} by comparing the intensity of diffraction originating from the intersection of the Ewald sphere with a bright spot and a scattering rod, respectively. While the maximum diffraction intensity in a spot is proportional to Λ_{corr}, in a rod it is independent of Λ_{corr}. This estimate gives a result similar to the one obtained in Section 4.3.

Experiments on a direct visualization of Bragg diffraction rods have also been carried out. The scheme of our diffraction geometry in that particular case is shown in Fig. 4.8. In order to directly visualize the Bragg rods on the detector, the sample had to be oriented in such a manner that the Ewald sphere produced a vertical cut through the reciprocal lattice of Fig. 4.8(a). In the flat capillaries used one can find crystals with various orientations. Now a crystal was chosen such that its hexagonal planes made an angle of about 60 degrees with respect to the capillary wall, thus enabling us to align the incoming wave vector parallel to the crystal planes as is schematically outlined in Fig. 4.9. This yields the diffraction pattern $I(\mathbf{q})$ as shown in Fig. 4.10(a). For this orientation, the Ewald sphere cuts through the reciprocal lattice as shown by the solid line in Fig. 4.8(b).

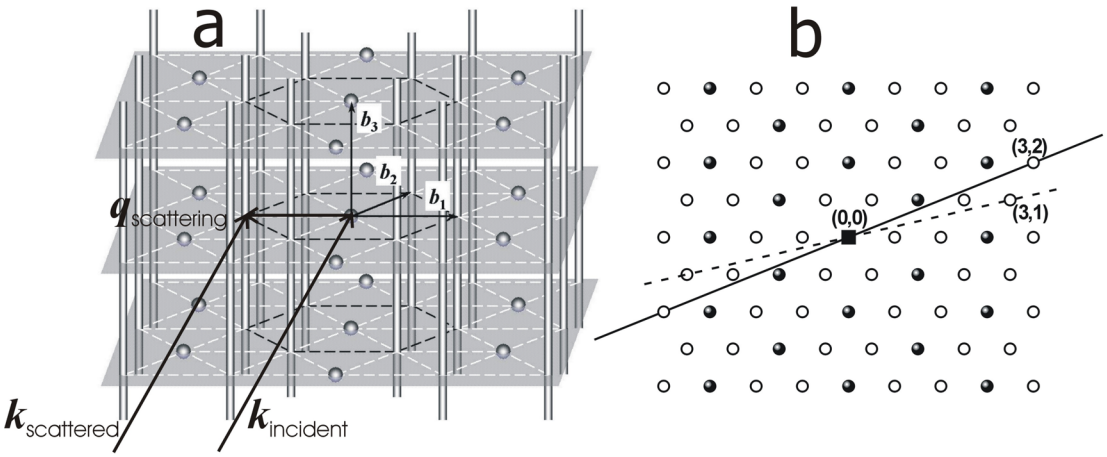

Figure 4.8. The scheme of the in-plane diffraction experiment. (a) Sketch of the reciprocal lattice of randomly-stacked hexagonal close packed crystals. The shadowed planes are to guide the eye. (b) Top view of the reciprocal lattice illustrating the orientation of the Ewald sphere in Fig. 4.10 (solid line) and in Fig. 4.11 (dashed line). The closed symbols correspond to lines of localized reflections (spots) while open symbols display the position of rods.

Fig. 4.10(b) shows a magnified view of the structure factor $\Xi(\boldsymbol{q})=I(\boldsymbol{q})/|f(\boldsymbol{q})|^2$. The form factor $f(\boldsymbol{q})$ has been determined from the scattering pattern of a dilute suspension of colloidal particles. X-ray scattering is observed on the detector along several lines, which originate from the Bragg rods and spots of the reciprocal lattice.

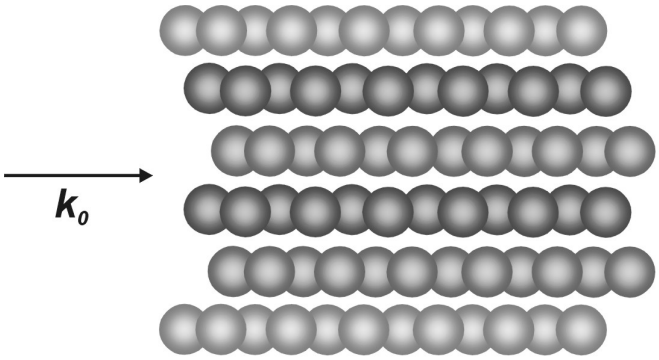

Figure 4.9. Schematic representation of the sample orientation in the in-plane diffraction experiment (see the text). Hexagonal layers are parallel to the incoming wave vector, $\boldsymbol{k_0}$, in this case.

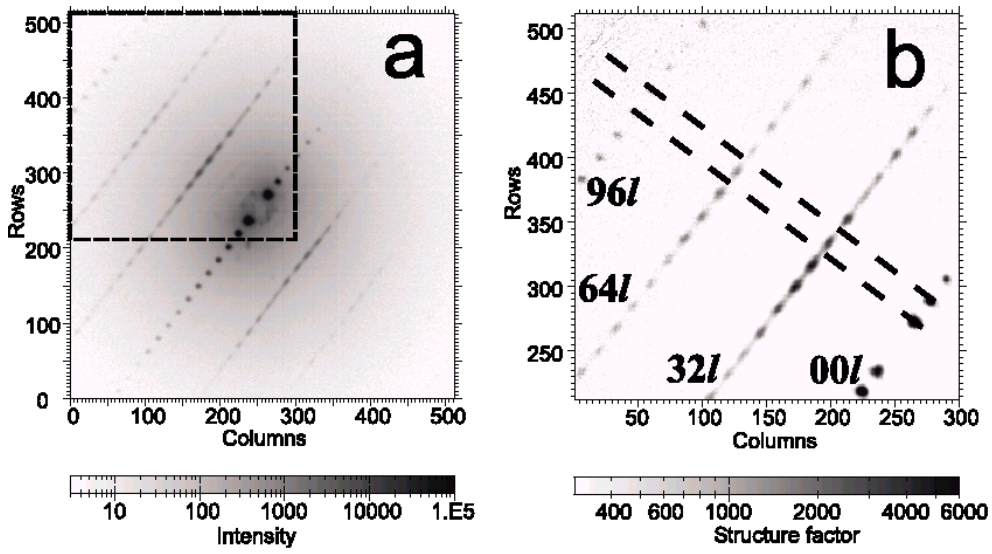

Figure 4.10. (a) Diffraction pattern measured for the crystal orientation corresponding to the Ewald sphere position illustrated by the solid line in Fig. 4.8(b). The direct beam is absorbed by a small beam stop in the middle of the detector. (b) Magnified view of the structure factor $\Sigma(\mathbf{q})$ *profile within the area marked on panel (a). The dashed lines in (b) display the position of the shadowed planes of Fig. 4.8(a) at l=1 and l=2.*

In this case the Ewald sphere misses many rods of low order but does cross the (32*l*) and (64*l*) rods (see Fig. 4.8(b)). The diffraction intensity along the Bragg rods in Fig. 4.10 is seen to smoothly vary and display a periodic modulation with minima at integer values of *l* and broad maxima in between them. This profile of the structure factor along the rod is typical for an *rhcp* crystal with stacking parameter $\alpha = 0.5$. Simulations show that for $\alpha < 0.4$ the maxima are narrower and new maxima develop at integer values of *l* [14] (see Fig. 3.3 in Chapter 3). For $\alpha > 0.6$ the broad maxima split into two. Note that the diffraction into (00*l*) spots in Fig. 4.10 is still very strong and might affect the distribution of the x-ray power over the sharp reflections as well as along the rods. However, since this can change the wave vector only by an integer times the $\boldsymbol{b}_3$ vector, these multiple scattering events should not significantly change the intensity profile within one period of the structure factor along the rod, which is equal to b_3.

In Fig. 4.7 the assignment of the *rhcp* structure for one-year-old crystals was based on the comparison of intensities of different reflections, which might be somewhat affected by dynamic diffraction, which will be discussed in the next Chapter. The results presented in Fig. 4.10, however, unambiguously confirm the *rhcp* structure because multiple scattering cannot broaden sharp reflections into Bragg rods.

4.5 Coexistence of *rhcp* and *fcc* phases

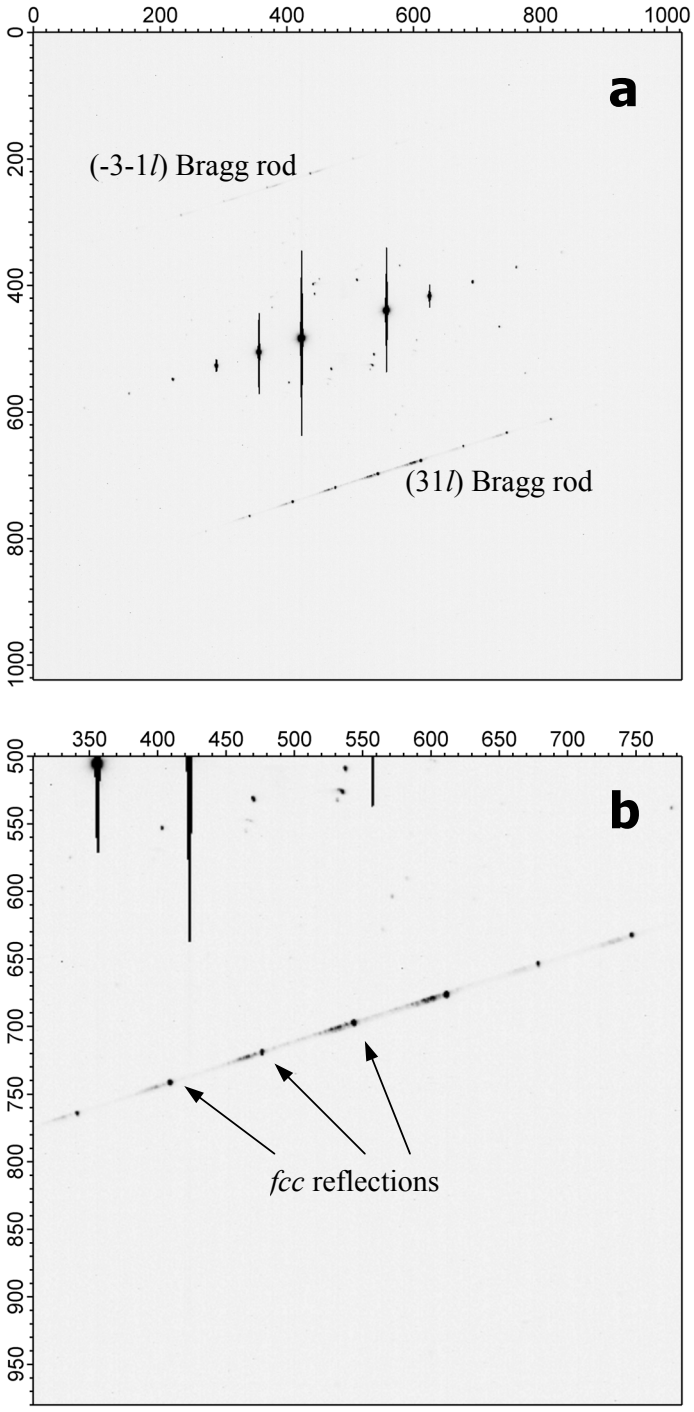

Figure 4.11. (a) Diffraction pattern ("in-plane" diffraction geometry) showing coexistence of rhcp and fcc crystals and (b) magnified view of the scattering rod region. The data are taken with the 15 keV x-rays.

In Fig. 4.11(a) we present experimental diffraction patterns taken with the same samples of colloidal crystals as were discussed in the previous section. A setup with much higher transverse resolution (discussed in detail in Chapter 6) is used in this experiment. Three lines of reflections are shown: the central one is a row of very bright Bragg spots *(00l)* on both sides of which there are rows of low order (31*l*) Bragg rods. In this case the sample was oriented in a manner that the Ewald sphere cuts through the reciprocal lattice as shown by the dashed line in Fig. 4.8(b).

Here, the improved detector spatial resolution and a higher degree of collimation of the incoming beam played a crucial role. As a detector, an X-ray sensitive CCD camera has been used (Photonic Science, spatial resolution ~55 μm, field of image of 7.5 cm, 12-bits, 1024×1024 pixels digital image size – compared to ~0.5 mm of spatial resolution of the gas-filled multi-wire 2D detector used before). In the results presented before, our sedimented crystals seemed to have an *rhcp* structure with the stacking probability α of finding an *fcc* stacking sequence close to α = 0.5. Due to the stacking disorder, the reciprocal lattice of *rhcp* crystals possesses Bragg scattering rods. The latter were directly visualised on the detector in the previous experiments as was described in the former Section 4.4. The intensity distribution along the rod (broad maxima at half-integer values of *l*) closely corresponds to α = 0.5. However, with the improved system instrumental resolution, we can now resolve additional sharp reflections along the Bragg rod (see Figures 4.11 and 4.12).

They appear at $l = n - 1/3$, where n is any integer. In the rod $(\bar{3}\bar{1}l)$, similar sharp reflections appear at $l = n + 1/3$ (Fig. 4.11(a)). The only plausible explanation for the existence of these sharp reflections is the presence of a single-domain *fcc* crystal with one of its (111) planes attached to the hexagonal planes of the *rhcp* single crystal [17]. Note that the volume of the *fcc* crystal (which could be estimated by integrating the intensity within one reflection) is small compared to the volume of the *rhcp* crystal. The latter is proportional to the integral along the rod within one period of the structure factor. The absence of twin *fcc* reflections indicates that the crystal does not possess a single *stacking fault* as discussed in the previous Chapter 3. Thus, although most part of the crystalline sediment possesses *rhcp* structure, occasionally one can find small crystals with a faultless *fcc* structure.

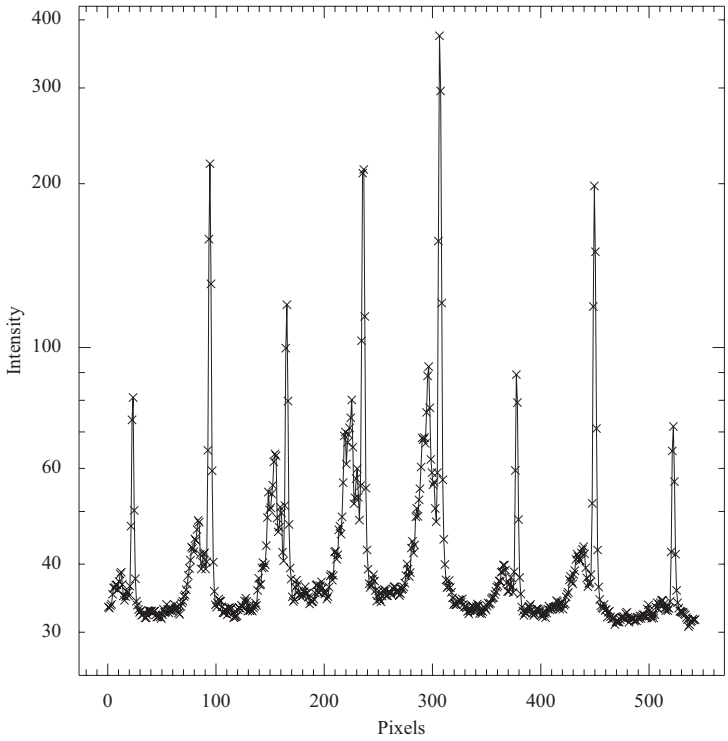

Figure 4.12. Coexistence of rhcp and fcc crystals: a slice of the diffracted intensity along the rod (appearing in the bottom part of the diffraction pattern shown in Fig. 4.11(a)).

4.6 Conclusion

The data, presented here, allow for an accurate characterization of various long-range order parameters and clearly reveal that the inherent size polydispersity of colloids does not prevent the formation of high-quality large single crystals possessing long-range positional and orientational order [18-24]. Theory predicts that for monodisperse hard spheres the face-centered cubic structure is the most stable [9]. However, a random stacking structure is found, which is also commonly observed in other hard-sphere systems [10,11].

The present results suggest that the stacking disorder has a long lifetime (much longer than a year) or even might be the stable state due to, e.g., the sphere polydispersity. It is interesting to note that the structure displayed by hard-sphere crystals distinctly differs from the structure of charge-stabilized colloidal crystals [22,7]. Although the latter have a mosaic structure with a much shorter extent of the positional order [22], they do display a high degree of *fcc* stacking order [22,7].

Common belief is that the metastable hard-sphere *rhcp* crystals may have various values of the stacking parameter α. Our results, instead, seem to indicate that the α-parameter can only

have two discrete values of 0.5 (in *rhcp*) and 1 (in *fcc*). This would suggest that the transition from *rhcp* to *fcc* does not go by a smooth variation of α but through a rearrangement mechanism as proposed in Ref. [21].

Literature:

[1] N.A.M. Verhaegh, D. Asnaghi, and H.N.W. Lekkerkerker, Physica A **264**, 64 (1999)

[2] E. H. A. de Hoog, L. I. de Jong-van Steensel, M. M. E. Snel, J. P. J. M. van der Eerden, and H. N. W. Lekkerkerker, Langmuir **17**, 5486 (2001).

[3] A. Gabriel, F. Dauvergne, Nucl. Instr. Meth. **201**, 223 (1982).

[4] P.P. Ewald, Proc. Phys. Soc. London, **52**, 167 (1940).

[5] R.W. James, *The Optical Principles of the Diffraction of X-rays* (Cornell University Press, Ithaca, New York, 1965); J.M. Cowley, *Diffraction Physics* (North-Holland, Amsterdam, 1981).

[6] J. L. Harland, S. I. Henderson, S. M. Underwood, and W. van Megen, Phys. Rev. Lett. **75**, 3572 (1995).

[7] T. Harada, H. Matsuoka, T. Ikeda, and H. Yamaoka, Colloids Surf. A **174**, 79 (2000).

[8] A. V. Petukhov, D. G. A. L. Aarts, I. P. Dolbnya, E. H. A. de Hoog, K. Kassapidou, G. J. Vroege, W. Bras, and H. N. W. Lekkerkerker, Phys. Rev. Lett., **88**, 208301 (2002).

[9] P.G. Bolhuis, D. Frenkel, S.-C. Mau, and D.A. Huse, Nature (London) **388**, 235 (1997).

[10] N.A.M. Verhaegh, J.S. van Duijneveldt, A. van Blaaderen, and H.N.W. Lekkerkerker, J. Chem. Phys., **102**, 1416 (1995).

[11] J. Zhu et al.,Nature (London), **387**, 883 (1997).

[12] W.K. Kegel and J.K.G. Dhont, J. Chem. Phys., **112**, 3431 (2000).

[13] A. V. Petukhov, I. P. Dolbnya, D. G. A. L. Aarts, G. J. Vroege, and H. N. W. Lekkerkerker, Phys. Rev. Lett., **90**, 028304 (2003).

[14] O.S. Edwards and H. Lipson, Proc. Roy. Soc. A 180, 268 (1941); A.J.C. Wilson, ibid, 180, 277 (1941); A.J.C. Wilson, *X-Ray Optics* (Methuen & Co. Ltd., London, 1949).

[15] A. Guinier, *X-ray Diffraction in Crystals, Imperfect Crystals, and Amorphous Bodies* (W.H. Freeman and Company, San Francisco and London, 1963).

[16] M. Megens and W.L. Vos, Phys. Rev. Lett., **86**, 4855 (2001).

[17] I. P. Dolbnya, A. V. Petukhov, D. G. A. L. Aarts and G. J. Vroege, to be submitted.

[18] S.I. Henderson and W. van Megen, Phys. Rev. Lett. **80**, 877 (1998).

[19] S. Auer and D. Frenkel, Nature (London) **413**, 711 (2001).

[20] D.A. Kofke and P.G. Bolhuis, Phys. Rev. E **59**, 618 (1999).

[21] W. G. T. Kranendonk and D. Frenkel, Mol. Phys. **72**, 679 (1991).

[22] W. Vos, M. Megens, C.M. van Kats, and P. Bosecke, Langmuir **13**, 6004 (1997); J.E.G.J. Wijnhoven, L. Bechger, and W.L. Vos, Chem. Mater, **13**, 4486 (2001).

[23] Zh. Cheng et al., Phys. Rev. Lett., **88**, 015501 (2002).

[24] S.R. Williams, I.K. Snook, and W. van Megen, Phys. Rev. E, **64**, 021506 (2001).

Chapter 5

Effects of dynamical diffraction in random stacking colloidal crystals

5.1 Introduction

So far, the *kinematic* approach (single-scattering approximation) has been used to describe the results. In principle, the scattering by any three-dimensional sample always includes some processes of multiple scattering since photons scattered by one part of the sample will propagate through other parts and, thus, have a probability to re-scatter again. The electron density of ensemble of atoms/particles can be presented as:

$$\rho(\vec{\boldsymbol{r}}) = \sum_i \rho_i(\vec{\boldsymbol{r}}) \otimes \delta(\vec{\boldsymbol{r}} - \vec{\boldsymbol{r}}_i),$$

where $\rho_i(r)$ is the electron density of atom/particle at its position at a point $\vec{\boldsymbol{r}} = \vec{\boldsymbol{r}}_i$, symbol δ denotes the Dirac delta-function and symbol $\otimes$ stands for convolution. The applicability of the single-scattering approach suggests that the amplitude of the single-scattered wave is very small in comparison with the amplitude of the incoming (reference) wave. Therefore, the amplitudes of double- and multiple-scattered beams would become even less, and thus can be neglected in comparison with the amplitude of a single-scattered wave. If the sample comprises spatially disordered atoms or particles the phase factors of different waves scattered by different atoms would be random, and therefore they would be averaged in the corresponding expressions for the scattered intensities. In another extreme case of true long-range order periodic structures, i.e. crystals, where the positions of individual atoms/particles in space are well correlated, the phases of scattered waves will be well defined and can be unambiguously determined. Thereby, the amplitudes of waves scattered by different atoms will be summed leading to waves, which interfere with each other. Such a correlated multiple scattering can be considered as *dynamical* scattering. The intensity of the corresponding diffracted waves, appearing in a crystal, depends on the

differential scattering cross-section, crystal size and orientation of the crystal with respect to the incoming beam.

It is instructive to make a comparison with electron diffraction, which is often exploited in transmission electron microscopy. Unlike x-rays, electrons have significantly shorter (de Broglie) wavelengths and electron diffraction is observed at small angles even in atomic crystals. Another essential difference is that electrons interact much stronger with matter. The effects of dynamic diffraction are then important even in very thin crystalline samples. It was electron diffraction, which first called for a development of the theory of dynamic diffraction that was founded in pioneering works of Bethe [1]. Due to the small diffraction angles of electrons, the Bragg condition is often simultaneously fulfilled for many reflections and the theory of Bethe also included *n*-beam interactions.

For x-rays with their smaller contrast, dynamic effects in the so-called perfect crystals were also recognized a long time ago and the corresponding theories were developed by Zachariasen [2], James [3], Batterman and Cole [4], Pinsker [5] and Authier [6]. One may also mention the recent work in that field by Shen and Collela (see [7] and references cited therein).

The case of x-ray small-angle diffraction in large-period colloidal crystals is similar to electron diffraction. First of all, the diffraction is also observed at small angles and one can thus create conditions when many diffracted waves exist in a crystal simultaneously. However, the effects of dynamical diffraction in colloidal crystals were hardly addressed in the past. Here, we demonstrate that the effects of multiple scattering can play a significant role and therefore must be taken into consideration, which makes small-angle x-ray diffraction in colloidal crystals even more similar to electron diffraction in atomic crystals.

5.2 Secondary Bragg rods

The (scheme of the diffraction) geometry was the same as was used to directly visualize Bragg diffraction rods (described in Chapter 4). It is reproduced in Fig. 5.1. To demonstrate the effects of dynamical diffraction, the sample was oriented in such a

manner that the Ewald sphere crosses the reciprocal lattice along the solid line shown in Fig. 5.1. In that case, the sample produced the diffraction pattern shown in Fig. 5.2.

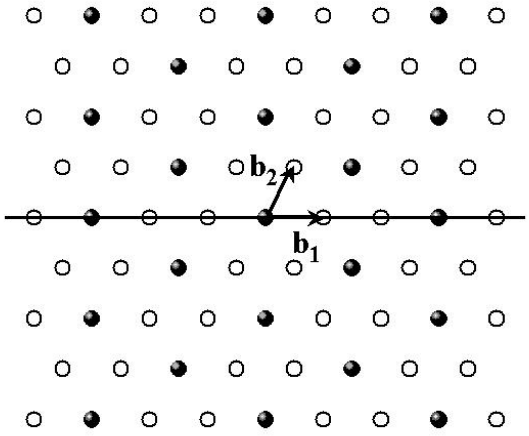

Figure 5.1. Representation of the reciprocal lattice as seen along the (00-1) direction, which illustrates the orientation of the Ewald sphere to observe the effects of dynamical diffraction (see Fig. 5.2). The closed symbols correspond to lines of localized reflections (spots) while open symbols display the position of rods.

In this case many Bragg rods, including the low-order (10*l*) rod, lie on the Ewald sphere. Here *l* denotes the continuously varying component of the diffraction vector along the rod (i.e., along the basis vector $\boldsymbol{b}_3$ of the reciprocal lattice of rhcp). Scattering into these rods is possible and they are clearly visible in Fig. 5.2. However, additional diffracted intensity (secondary Bragg rods) may be also seen in between the Bragg spots (00*l*), (30*l*), (60*l*), etc. We attribute this effect to the effect of multiple scattering: the incoming X-ray wave can be first scattered into a rod and then be re-scattered again. Note that these multiple scattering events always lead to scattering along the same lines on the detector, which are equally spaced.

To support the interpretation of the secondary Bragg rods as a multiple scattering effect, one can compare Fig. 5.2 with Fig. 4.10. In the latter case scattering into many low-order rods does not occur and the first Bragg rod observed is the (32*l*) rod. The scattering into this high-order rod is then much weaker, mainly due to the rapid decay of the form factor $|f(\boldsymbol{q})|^2$. Correspondingly, the multiple scattering via the Bragg rods is very much suppressed. In Fig. 4.10 the lines of diffraction spots (00*l*) and (96*l*), *l* = integer, are clearly seen without appearance of secondary rods.

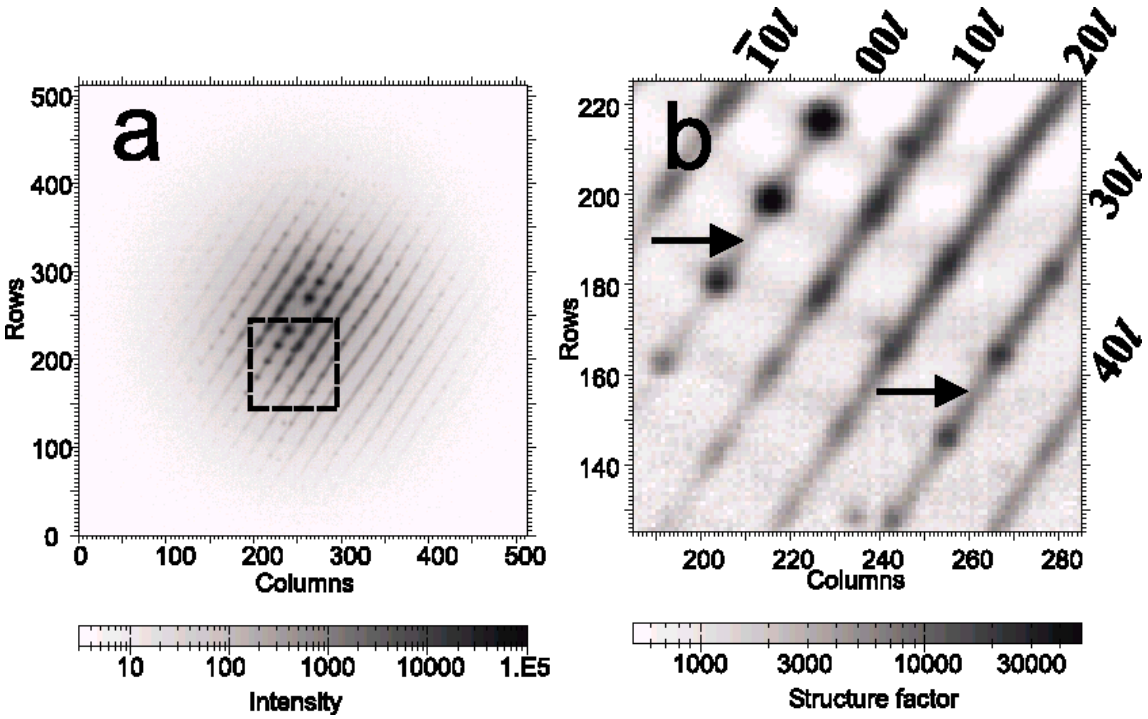

Figure 5.2. (a) Diffraction pattern measured for the crystal orientation corresponding to the Ewald sphere position illustrated by the solid line in Fig. 5.1. The direct beam is absorbed by a small beam stop in the middle of the detector image area. The photon energy is 10 keV. (b) Magnified view of the structure factor $\Sigma(\mathbf{q})$ *profile within the area marked on panel (a). Arrows point to the secondary Bragg rods in between the sharp Bragg spots.*

Dynamical diffraction takes place when the interaction of the incident wave with the sample is no longer weak and one has to take into account that the diffracted waves deplete the incident beam and become in turn sources of secondary diffraction. The complexity of the theoretical modelling of such dynamic interactions raises significantly upon increasing the number of mutually interacting waves [7]. An even more complicated description is developed for visible light waves in photonic materials, where the refractive index contrast is large and the effect of diffraction is not weak even within one period of the structure [8,9]. Almost all theories deal with dynamic diffraction in crystals with full 3D periodicity. The effect of stacking faults lifting periodicity in one direction has been investigated in Ref. 8 and the photonic gap for visible light at normal and grazing incidence is found to broaden. Despite the significant progress of theories, there is no one that can be easily applied to describe our data shown in Fig. 5.2.

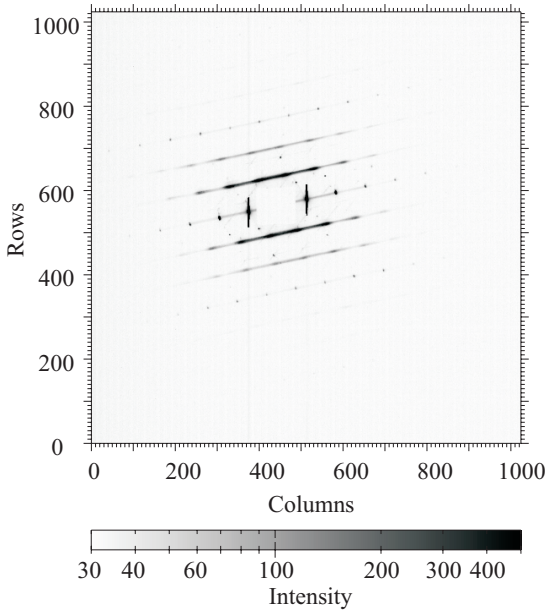

Figure 5.3. Diffraction pattern visualizing low-order (10l)- and (20l)-class rods and (00l)-and (30l)-class spots. The photon energy is 15 keV. Note the multiple-diffraction-induced scattering between the spots. The brightest reflections much over-saturate the CCD camera used leading to vertical streaks on the detector. Note also that the X-ray beam hits a few crystals: extra reflections, which belong to other crystals, can be also seen.

A similar observation, obtained during another experimental session with a higher-resolution setup (described in more details in section 6.2) is presented in Fig. 5.3. Note that a higher x-ray photon energy of 15 keV was used here. Thus, the contrast was reduced $(15/10)^2 = 2.25$ times in comparison with Fig. 5.2. Still, secondary Bragg rods are clearly visible.

5.3 The strength of diffraction

To demonstrate that in our system diffraction enters the dynamic regime, one can estimate the strength of diffraction using the much simpler kinematic approach. The power $dP_{sc} = (d\sigma/d\Omega)I_0 d\Omega$ of the wave scattered by a single colloidal particle into a small element $d\Omega$ of the solid angle can then be described by the differential scattering cross section $(d\sigma/d\Omega) = r_0^2 Z^2 |f(\boldsymbol{q})|^2$, where I_0 is the intensity of the incident wave at the position of the particle, $r_0 = e^2/(mc^2)$ is the Thompson radius, $\boldsymbol{q}$ is the scattering vector and Z is the excess number of electrons in the colloidal particle

relative to an equivalent volume of solvent. The form factor is normalized such that $|f(\mathbf{q}\rightarrow 0)|^2 = 1$, and it equals $|f(\mathbf{q})|^2 = 9(\sin qR - qR\cos qR)^2/(qR)^6$ [10] for a sphere of radius R with a uniform distribution of the electron density. Under the conditions of our experiment (specific weight [11] of silica particles and the solvent cyclohexane are 1.7 and 0.77 g/ml , respectively, corresponding to a refractive index contrast of $\Delta n = 2.1\times10^{-6}$ for 10 keV X-rays), the total small-angle scattering cross section $\sigma=\int(d\sigma/d\Omega)d\Omega$ of one sphere is about 12 nm^2 , i.e., only 3×10^{-4} of its geometrical cross section πR^2. Thus, a single particle only weakly interacts with the x-ray wave.

However, the situation may change drastically if silica spheres form a single long-range ordered crystal and the incident x-ray beam provides conditions for coherent interference over large distances [12]. If for a sharp *hkl*-reflection with (*h-k)* divisible by 3 the Bragg condition is fulfilled (i.e., it is crossed by the Ewald sphere), the weak waves scattered by individual spheres interfere constructively and the diffracted power grows quadratically:

$$P_{(hkl)} = (L/L_{(hkl)})^2 P_0; \qquad (5.1)$$

with the distance L traveled by the beam in the sample. Here P_0 is the total power of the incident beam and the characteristic length $L_{(hkl)}$ is determined by [3]:

$$(L_{(hkl)})^{-2} = \lambda^2 n^2_{\mathrm{sph}} (d\sigma/d\Omega)_{(hkl)} ; \qquad (5.2)$$

where n_{sph} is the number density of spherical particles. Assuming a close-packed crystal structure with $n_{\mathrm{sph}}=1/(4\sqrt{2}\,R^3)$ and collecting all the numbers in Eq. (5.2) for the lowest order (001) reflection seen in Fig. 5.2, one finds $L_{(001)}$ = 0.11 mm, i.e., about half the crystal size along the beam. Clearly, the diffracted power is then comparable to P_0 and diffraction switches from the kinematic to the dynamic regime. Interestingly, the dependence of $L_{(hkl)}$ on the particle size R cancels in Eq. (5.2) since $(d\sigma/d\Omega) \propto R^6$ and $n_{\mathrm{sph}} \propto R^{-3}$. Thus, for larger spheres dynamic diffraction can be observed for a smaller number of lattice periods. This factor leads to a principal difference between atomic and colloidal crystals in requirements of their perfectness to observe dynamic diffraction. While the former requires perfect order over 10^5 lattice constants, in the latter positional order over as little as a few hundreds of lattice periods can break up the kinematic description of x-ray diffraction.

In contrast to a sharp reflection like (001), in a Bragg rod the scattering amplitudes of different hexagonal planes have additional stacking-dependent phase shifts. This significantly reduces the intensity diffracted in one particular direction and

spreads the diffraction intensity along the Bragg rod. However, if the crystal possesses long-range in-plane order along the beam, scattering amplitudes within each layer interfere constructively leading to a similar quadratic dependence of the scattered power with the distance L. For example, to evaluate the power $P_{(10l)}^{[0,1]}$ scattered into a piece of the low-order (10l) rod between l = 0 and l = 1 , one has to integrate the form factor $|f(q)|^2$ together with the structure factor $S_{\mathrm{rod}}(\boldsymbol{q})$ arising from interference between contributions of randomly stacked planes. One then finds that within the kinematic theory $P_{(10l)}^{[0,1]}$ grows as in Eq. (5.1) with $L_{(10l)}^{[0,1]}$ = 0.15 mm , i.e., the power scattered into the low-order (10l) rod grows nearly as fast as the power diffracted into the (001) reflection since scattering along the whole rod is possible at this sample orientation. The estimates thus show that the incident x-ray beam is quickly depleted by scattering into the low-order spots and rods, which become in turn sources of strong secondary diffraction. Scattering into the (10l) Bragg rods is able to compete with diffraction into the sharp (001) reflection and the appearance of secondary Bragg rods in Fig. 5.2 is therefore not surprising.

Note that the contrast and, thus, the diffraction strength depend on the x-ray energy, see Eq. (5.2). For the 15 keV x-rays, used in Fig. 5.3, the estimates given above change to $L_{(001)}$ = 0.16 mm and $L_{(10l)}^{[0,1]}$ = 0.23 mm. Still, these characteristic lengths are comparable to the sample thickness of 0.2 mm and multiple scattering effects can also account for the secondary rods observed at 15 keV.

5.4 Direct evidence of dynamical diffraction regime

To show the effect of multiple-wave diffraction is on the direct beam, a few diffraction patterns were measured without the beam stop, hence allowing us to directly compare intensities of low-order reflections and of direct beam. The experimental setup is described in section 6.2.

Figure 5.4 presents diffraction patterns taken at the same sample orientation but with different exposure times. In panel 5.4(a) the direct beam is closed and a much longer exposure time (10 min) is used. It is shown to clarify the sample orientation. The incident X-ray beam propagates along the hexagonal planes in the crystal and directly visualizes two of the (31l)-class scattering rods. The image shown in panel

5.4(b) is taken with a much shorter exposure time (1 s) and the beam stop is moved away. Here the direct beam and the lowest-order (001)-class diffraction peaks do not over-saturate CCD camera used as a detector. Thus, we can directly compare their intensities. As shown in panel 5.4(c), the diffracted peaks have intensities of the order of 5 and 10% of the intensity of the direct beam. These are quite significant intensities, especially if one has to consider a coherent interference of single- and multiple-diffracted waves when both the beam and the structure keep their coherence.

Figure 5.5 presents an even more striking example illustrating the importance and role of dynamical diffraction. Here the incident beam is normal to the hexagonal

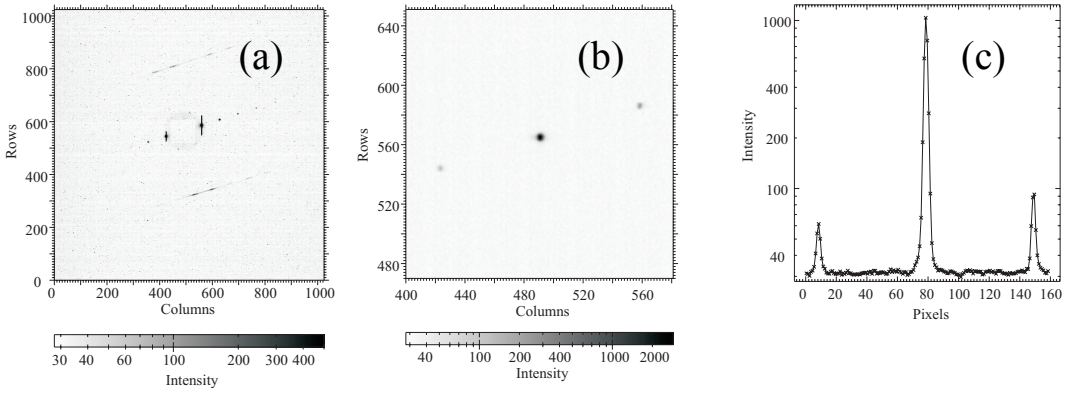

Figure 5.4. Diffraction pattern taken with longer exposure time and blocked direct beam (a) and a zoom into the central part of the diffraction pattern with shorter exposure time and direct beam hitting the detector (b). The photon energy is 15 keV. Panel (c) presents a slice through the intensity profile in (b).

planes of the crystal. Six low-order (110)-class reflections are very bright (indicated referring to the 12-hour scale of an ordinary watch). As can be seen from intensity profiles, the diffraction peak at 1:30 is the strongest and has maximum intensity higher even than that of the direct beam. Those at 11:30 and 3:30 are comparable to the direct beam while the other three in the left-bottom part of the image are 3 to 4 times weaker. The asymmetry (11:30 is stronger than 5:30, etc.) is indicative of the very small angular width of the reflections. It originates from the curvature of the Ewald sphere, as described in more detail in the previous chapter. The use of harder (15 keV instead of 10 keV) X-rays led to a smaller curvature of the Ewald sphere. Its radius was increased by a factor of 1.5 and its deviation from a plane at small angles was reduced by $1.5^2 = 2.25$ times for the same crystal reflections.

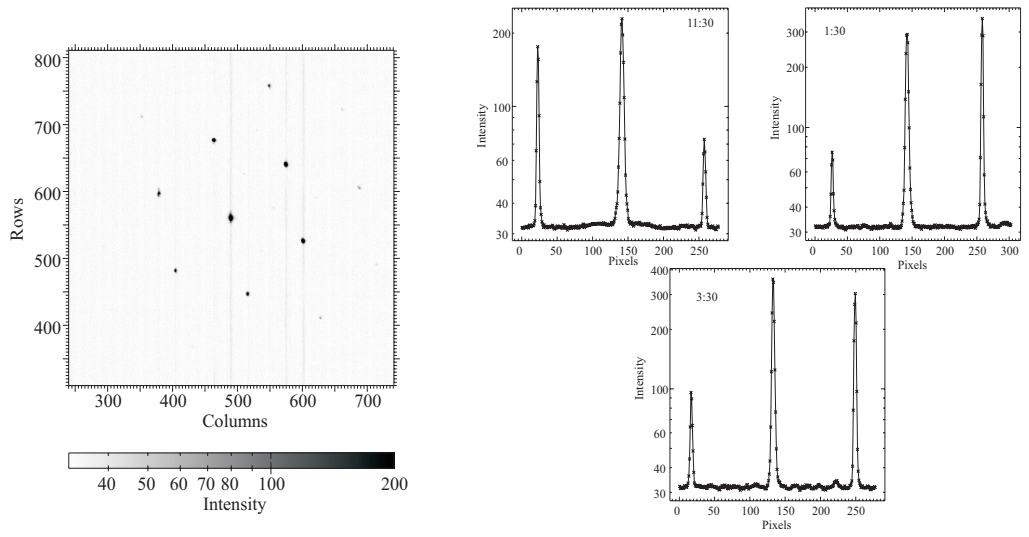

Figure 5.5. The image on the left presents a diffraction pattern together with the direct beam. The photon energy is 15 keV. The insets on the right show slices of intensity profiles taken from 11:30 to 5:30, 7:30 to 1:30, and 9:30 to 3.30. All intensity profiles intersect the centre of diffraction pattern. The intensities in different panels are not to be compared directly - the intensities are averaged over slices of different thickness. The expose time is 0.1 sec.

Using the analysis presented in section 5.3, one can evaluate the characteristic length $L_{(110)}$=0.26 mm in this colloidal crystal for the strong (110) reflections seen in Figure 5.5 and 15 keV x-rays. Therefore, the sample thickness L=0.2 mm was just comparable to $L_{(110)}$, so that the diffracted beam can significantly deplete the direct beam towards the end of the crystal. This is indeed confirmed by our observations. It also becomes clear that the diffracted beams are very strong and can in turn act as fundamental beams to induce strong secondary diffraction.

5.5 Conclusion

In conclusion, direct evidence of the dynamic regime of X-ray diffraction in the long-range ordered colloidal crystal has been demonstrated. It reveals itself in the diffraction pattern as an appearance of secondary Bragg rods. Simple estimates show that, in contrast to common belief, dynamic x-ray diffraction should be rather typical for crystals consisting of highly ordered (sub)micrometer colloidal spheres and has to be taken into account. Since dynamic diffraction is likely to redistribute the diffracted

power towards weaker reflections, one should be aware that the amplitude of particle excursions evaluated from the Debye-Waller factor and the spatial extent of the positional order in colloidal crystals could be underestimated.

The estimates given above show that the presence of long-range order along the beam is essential for the transition into the dynamic regime. Development of an appropriate theory is, however, needed in order to exploit dynamic diffraction for detailed *quantitative* structural characterization.

Literature:

[1] Bethe H.A, Ann. Physik, **87**, 55 (1928).

[2] Zachariasen W.H., *Theory of X-ray diffractions in crystals* (Wiley, New York, 1945).

[3] R.W. James, *The Optical Principles of the Diffraction of X-rays* (Cornell University Press, Ithaca, New York, 1965); J.M. Cowley, *Diffraction Physics* (North-Holland, Amsterdam, 1981).

[4] Batterman B.W. and Cole H., Rev. Mod. Phys., **36**, 681 (1964).

[5] Pinsker Z.G., *Dynamical scattering of x-rays in crystals*, in Springer Series in Solid-State Sciences, Volume 3, Eds. Cardona M., Fulde P., Queisser H.J., (Springer Verlag, Berlin, 1978).

[6] Authier A., in *Advances in structural research by diffraction methods*, Vol. 3, eds. R. Brill, R. Mason, (Pergamon, Oxford, 1970), p. 1.

[7] Q. Shen, Dynamic diffraction, in: *Methods in Materials Research*, ed. E. Kaufmann et al. (John Wiley & Sons, 2000).

[8] V. Yannopapas, N. Stefanou, and A. Modinos, Phys. Rev. Lett., **86**, 4811 (2001).

[9] A. Moroz, Phys. Rev. Lett., **83**, 5274 (1999).

[10] L. A. Feigin and D. I. Svergun, *Structure Analysis by Small-Angle X-Ray and Neutron Scattering* (Plenum Press, New York, 1987).

[11] N.A.M. Verhaegh, D. Asnaghi, and H.N.W. Lekkerkerker, Physica A, **264**, 64 (1999); E.H.A. de Hoog et al., Langmuir **17**, 5486 (2001).

[12] A. V. Petukhov, D. G. A. L. Aarts, I. P. Dolbnya, E. H. A. de Hoog, K. Kassapidou, G. J. Vroege, W. Bras, and H. N. W. Lekkerkerker, Phys. Rev. Lett., **88**, 208301 (2002).

Chapter 6

Destruction of long-range order in d(r)ying colloidal crystals recorded with small-angle x-ray diffraction

6.1 Introduction

To further illustrate the capabilities of the high-resolution small-angle x-ray diffraction technique [1,2], we apply it to record in-situ the destruction of the long-range order during drying (i.e. solvent evaporation from the colloidal crystal). Capillary forces can play a significant role in drying colloidal systems, but their impact was earlier addressed mainly in connection with the formation of a paint film on surfaces [3]. The strong capillary forces are also used in the so-called controlled drying technique [4,5] to assemble colloidal spheres on a flat substrate. Drying might be needed, for example, for photonic applications if a colloidal crystal is used as a template to fabricate a band-gap photonic material. Previous studies already demonstrated that SAXD is very powerful technique in determining long-range order parameters in colloidal crystals [18,9,1,2]. Here x-rays are particularly advantageous since optical techniques are not suited due to greatly enhanced turbidity of the sample.

6.2 Experimental setup with high transverse resolution

The colloidal crystal samples [6,7] were the same that were used to assess the order parameters. A SAXD study was performed at the SAXS/WAXS station of the BM-26 "DUBBLE" beam line at the European Synchrotron Radiation Facility (E.S.R.F.) in Grenoble. A cone of about 4 microradians of synchrotron radiation was cut off by 100 μm wide horizontal and vertical primary slits situated at a distance z_{H1}=28 meters from the bending magnet radiation source. Monochromatic 15 keV x-rays (wavelength λ=0.83 Å, spectral width $\Delta\lambda/\lambda=2\cdot10^{-4}$) were selected by a sagittally focusing (i.e., in the horizontal plane of the electron orbit) double-crystal Si(111) monochromator, located at z_{mono}=33 m. It was followed

by a bent silicon mirror at z_{mir}=35.5 m downstream from the source, which focused the beam in the vertical plane and discriminated against harmonics coming from the monochromator. The sample was mounted at z_{samp}=49 m on computer-controlled rotation and translation stages allowing to scan through the sediment and to carefully orient the colloidal single crystals. The diffraction was recorded at a distance of 8 m from the sample (z_{det}=57 m) by an x-ray sensitive CCD (charge-coupled device) camera (X-Quis, Photonics Science). The diffraction images were digitized into 1024×1024 pixels with the pixel size corresponding to 52 μm physical separation on the phosphor screen of the camera. The entire field of view was about 7.5 cm along the diagonal. The readout offset was about 32 counts per pixel with a typical readout noise of 2 to 3 counts. The maximum measurable intensity corresponded to 4096 counts per pixel (12 bit data format). The sample drying was also visually observed using a video camera installed in the experimental hutch.

Apart from the use of the detector with higher resolution (in comparison to a gas-filled detector, see Chapter 2), the transverse resolution of the setup was improved by careful re-alignment of the whole optical setup. To achieve best resolution in the plane of the detector, the direct beam was focused on the screen of the CCD camera. Below we will give estimates of the setup resolution in this particular experiment. With the source size of about d_s=100 μm (root mean square) at the ESRF and at the wavelength λ used in the present experiment, the transverse coherence length was $l_{tr,mono}=\lambda z_{mono}/d_s$=27 μm at the position of the monochromator and $l_{tr,mir}=\lambda z_{mir}/d_s$=30 μm at the mirror (see Section 2.5.1). After a focusing element the beam converges and, correspondingly, the transverse coherence length l_{tr} shrinks. Assuming ideal optical elements and neglecting diffraction limitations, at the sample position l_{tr} can be estimated as $l_{tr,h}=l_{tr,mono}(z_{det} - z_{samp})/(z_{det} - z_{mono})$=9 μm and $l_{tr,v}=l_{tr,mir}(z_{det} - z_{samp})/(z_{det} - z_{mir})$=11 μm in the horizontal and the vertical directions, respectively.

The coherence length l_{tr} can be further shortened by imperfectness of the optical elements inserted between the x-ray source and the sample. Results presented in the following section show that in the horizontal direction the transverse coherence length $l_{tr} > 5$ μm was indeed reached in this experiment, suggesting practically ideal performance of the beamline optics with the relatively small entrance slits size of 100 μm used in the present experiment. Colloidal spheres separated in the transverse direction by a distance larger than l_{tr} are irradiated by mutually incoherent waves and their scattering fields do not interfere. As a result, the transverse coherence was sufficient to resolve the diffraction peaks, but is far too small to probe the long-range order.

Using the results of section 2.5.2 of this thesis, one can also evaluate the resolution of this setup in the longitudinal direction. The finite spectral width $\Delta\lambda$ will limit the resolution to $\delta q_1 = 4\pi\theta^2\Delta\lambda/\lambda^2 \sim 0.004$ mm^{-1} for the (110) reflections with the diffraction angle $2\theta_{(110)} = 7\times10^{-4}$ rad. As was shown in Chapter 2, an additional factor reducing the longitudinal resolution is related to the angular spread of the plane-wave components ε in the x-ray beam inside the sample. The corresponding spread of the Ewald spheres for the case $\theta << 1$ and $\varepsilon << 1$ limits the resolution to

$$\delta q_2 = 4\pi\theta\varepsilon/\lambda. \qquad (6.4)$$

We note again that, similar to δq_1, δq_2 reduces towards small scattering angles, although only linearly with θ.

One could distinguish two contributions to the total value of ε. One of them is related to the fact that the incoming x-ray beam has the form of a cone converging towards the detector. The opening angle of this cone $\varepsilon_{\text{cone}}$ is determined by the acceptance angle of the 100 μm wide primary slits divided by the magnification factor of the focusing system. Under the conditions of the present experiment one can evaluate $\varepsilon_{cone}=5\times10^{-6}$ and 6×10^{-6} in the horizontal and the vertical directions, respectively. The other contribution arises from the finite transverse coherence of the x-ray beam, which is discussed above. As a result, at a given point in the beam there is a finite angular spread $\varepsilon_{tr}=\lambda/l_{tr}$ of the mutually incoherent plane waves. Assuming uncorrelated contributions of ε_{cone} and ε_{tr}, one can estimate the total angular spread ε of the plane-wave components as $\sqrt{\varepsilon_{tr}^2+\varepsilon_{cone}^2}$, which amounts to 1.05×10^{-5} and 0.95×10^{-5} radians in horizontal and vertical planes, respectively.

Using the results of Section 2.5 and the estimates given above, one gets for the (110) reflections $\delta q_2 = 4\pi\theta\varepsilon/\lambda = 0.28$ mm^{-1} and 0.25 mm^{-1} in the horizontal and vertical directions, respectively. One can see that $\delta q_2 >> \delta q_1$, i.e. δq_2 is a much more important limiting factor than δq_1. Thus, the consideration presented above suggests that one can, in principle, achieve a resolution $\delta q/k_0$ better than 10^{-8}, which would allow one to probe positional correlations in the particle positions on distances up to $l_{beam}=2\pi/\delta q_2 > 1$ centimeter along the beam propagation direction. However, as shown in Chapter 5 of this thesis and further discussed in Section 6.5, there is another limitation of the technique related to the switch of the diffraction into the dynamic regime, which requires more sophisticated data analysis.

6.3 The "wet" crystal: structure and long-range order

It has been experimentally proven that the hard sphere colloids pack into a long-living random hexagonal close packed (rhcp) structure, which is formed by choosing the stacking direction of every subsequent layer at random [1,2,8-13]. To illustrate the stacking disorder in our sample, Fig. 6.1(d) displays the diffraction pattern obtained from one of the crystals inside

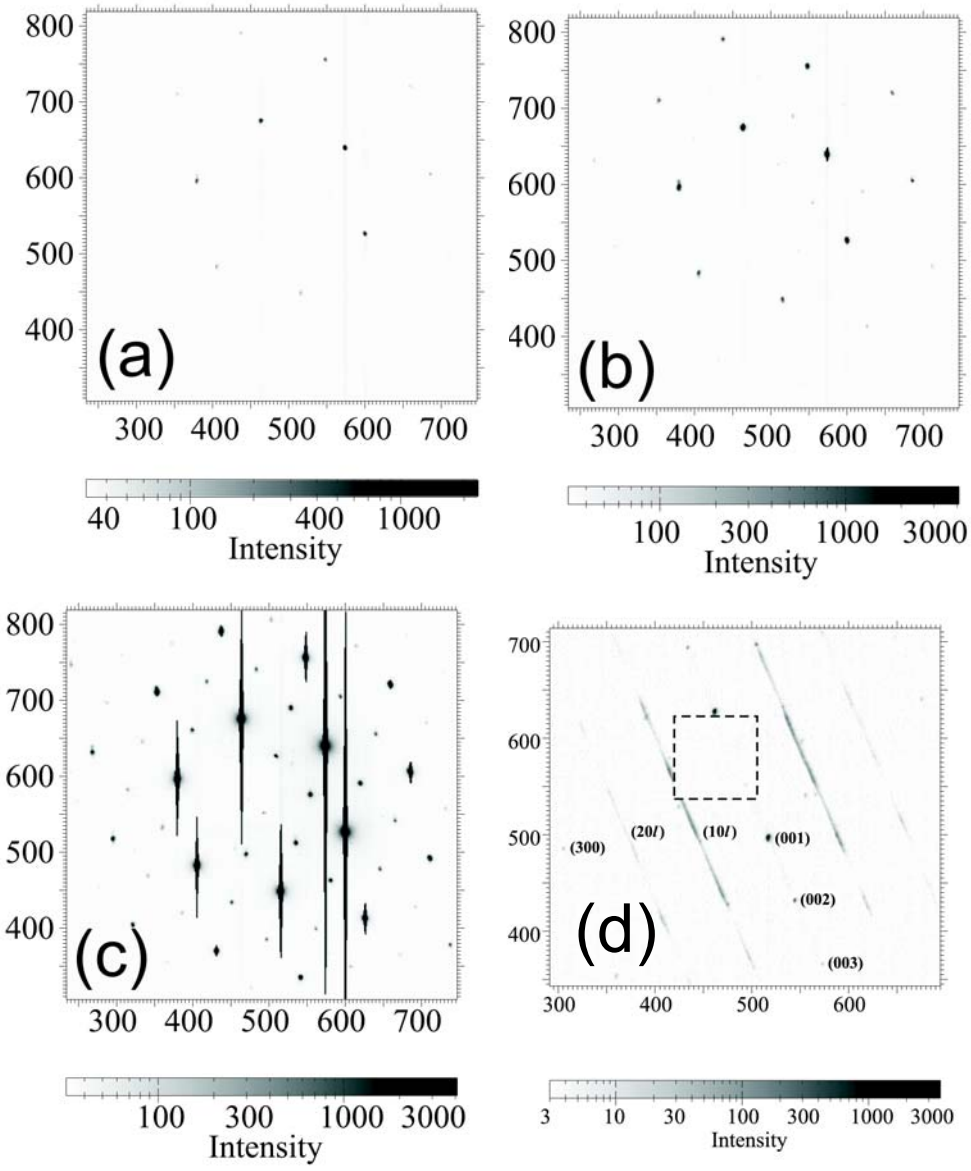

Figure 6.1. Diffraction patterns measured with the x-ray beam incident along the (001) direction (a-c) and the (-120) direction (d). The exposure time of the CCD camera is ΔT=0.1 s (a), ΔT=1 s (b,d), and ΔT=60 s (c).

the capillary. The hexagonal planes in this crystal make up a large angle with respect to the flat capillary surface enabling us to send the x-ray beam parallel to the hexagonal planes.

To observe the structure modification during drying we have chosen another crystal, with its hexagonal planes (nearly) parallel to the capillary walls. Figure 6.1(a) displays diffraction patterns measured after the hexagonal planes of the crystal have been carefully aligned normal to the incident x-ray beam. Here the *l*-index is nearly zero. The images are obtained at different exposure times ΔT. In panel (a) ΔT=0.1 s and only the brightest reflections are visible. Upon increase of ΔT in panels (b) and (c) the weaker reflections become detectable while the brightest reflections considerably over-saturate CCD camera. In (c) the too high exposure also leads to the appearance of vertical stripes in the image, presumably caused by a charge spill out effect into neighboring pixels in the vertical direction. By performing such a series of measurements one can compensate for the limited dynamic range of the CCD camera (i.e., the ratio of the maximum and minimum intensities, which can be reliably measured within one diffraction pattern).

Figure 6.2 presents the horizontal profile of one of the (110)-type diffraction peaks in Fig. 6.1(a). The solid line is a Gaussian fit $I(q_x)=I_0\exp(-(q_x-q_{x,0})^2/\sigma^2)+I_{dark}$ with I_0 and I_{dark} denoting the maximum peak intensity and the readout offset, respectively, $q_{x,0}$ =600.75 detector pixels is the x-position of the peak. The full 1/e width of the Gaussian fit is 2σ = 3.2 pixels = 1.5 μm^{-1}. There are several contributions to the peak width in the plane of the detector. In addition to the finite transverse coherence of the beam σ_{coh} discussed above, the instrumental resolution is determined by the resolution of the CCD detector itself σ_{det} and the

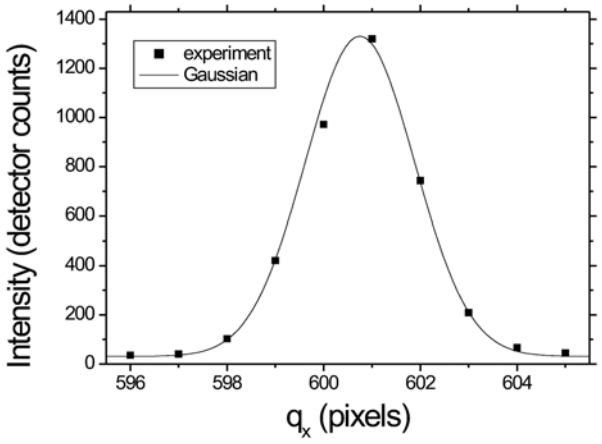

Figure 6.2. Horizontal profile through the (110)-type diffraction peak in Fig. 6.1(a) [with the maximum intensity at the detector coordinates (x, y)=(601, 527)]. Points present the detector readouts and the solid line is a Gaussian fit as described in the text.

imperfectness of focusing of the beam at the detector plane σ_{focus} depending on the quality of the optical elements and their alignment. Assuming statistically-independent contributions of these factors, one can express the observed peak width as $\sigma^2 = \sigma^2_{det} + \sigma^2_{focus} + \sigma^2_{coh} + \sigma^2_{intr}$, where σ_{intr} is half of the full intrinsic width of the reciprocal lattice reflection of the crystal itself. As will be demonstrated below, the crystal has extremely narrow reflections so that the last term can be neglected and σ is then entirely limited by the instrument. The full width of the point-spread function of the CCD detector used was about $2\sigma_{det}$=2...2.5 pixels and we could not independently estimate the exact value of σ_{focus}. Yet, one can conclude that $2\sigma_{coh}$ < 2...2.5 pixels = 0.9 ...1.2 μm^{-1} and, thus, the transverse coherence length $l_{tr} = 2\pi/(2\sigma_{coh})$ is larger than 5...6 μm. The vertical profile through the same reflection is ~20 % broader possibly due to imperfections of the beam focusing. All the other reflections in Fig. 6.1(a) have the same slightly elliptical shape with the same width.

To make use of the higher resolution achievable along the longitudinal direction in a small-angle experiment, the sample was tilted by angle $\zeta = 0.4°$ with respect to its orientation in Fig. 6.1(a). The axis of rotation is slightly inclined (by about 15° counter-clockwise) from the vertical direction. The resulting diffraction pattern is shown in Fig. 6.3. In this case the Bragg condition is still (nearly) fulfilled for two (110)-type reflections, which leads to only two very bright diffraction peaks strongly over-saturating the detector in Fig. 6.3 (marked in the figure with 1a and 1b). The other four (110)-type reflections (marked in the figure with 2) miss the Ewald sphere by $\Delta q = \zeta q_{(110)} = 0.3\ \mu m^{-1}$ and their intensity is strongly reduced (by about three orders of magnitude). Thus, the width of the reflections δq must be very much smaller than the wave vector mismatch $\delta q << \Delta q$.

A further estimate of the width of the reflections δq can be obtained by noting that the diffraction patterns in Figs. 6.1 and 6.3 display strong asymmetry, i.e., the intensities of two opposed reflections (h,k,l) and (-h,-k,-l) are significantly different (e.g., the (110)-type reflections marked as 1a and 1b in Fig. 6.3). At a small diffraction angle 2θ the Ewald sphere deviates from a plane by as little as $\delta q_\perp = k_0 \cdot 2\theta^2$. For a pair (h,k,l) and (-h,-k,-l) of opposed reflections the difference in the wave vector mismatch cannot be larger than $2\delta q_\perp$. The strong asymmetry of the (110)-type reflections thus suggests that $\delta q < 2\delta q_{\perp,(110)} = 0.037\ \mu m^{-1}$. This result indicates the presence of long-range order over distances of the order of $2\pi/(2\delta q_{\perp,(110)}) \approx 200$ microns, i.e., over the thickness of the capillary in agreement with earlier result [1]. In other words, the crystal before drying does possess long-range order, i.e. positional order over the whole crystal size.

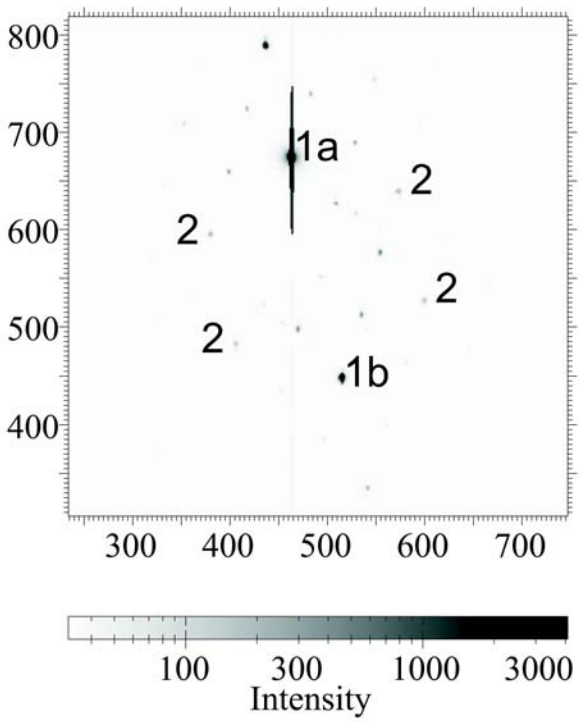

Figure 6.3. Diffraction pattern from a slightly tilted sample. The exposure time is ΔT=10 s. The six(110)-type reflections are marked by 1a, 1b, or 2; $q_{(110)}=4\pi/a$, a - nearest neighbor distance. t=-35 min.

So, one can probe the width of diffraction peaks on three different levels of sensitivity. The direct determination of the peak width from the detector image is the most crude and can detect broadening of the reciprocal lattice reflections in the transverse direction only of the order of $2\sigma = 1.5\ \mu m^{-1}$. In the longitudinal direction a much higher sensitivity can be achieved. One can make use of the tilted crystal orientation and compare the intensities of the (110)-type diffraction peaks marked 1 and 2, respectively, in Fig. 6.3. In this way one can detect changes of the width of reflections, when it is comparable to $\Delta q = 0.3\ \mu m^{-1}$. The highest sensitivity $\sim 2\delta q_{\perp,(110)} = 0.037\ \mu m^{-1}$ can be achieved by watching the asymmetry of the diffraction pattern (i.e., by comparing the intensities of reflections 1a and 1b).

6.4 Drying: loss of long-range order

The drying was achieved by cutting off the top part of the capillary with supernatant. Cyclohexane was let to evaporate from the remaining short (~30 mm) part of the capillary

through the open top. Figure 6.4 schematically summarizes some of the important stages of the drying process as observed using the video camera. No significant change of the diffraction pattern was detected after opening the capillary, when the meniscus was well above the sediment. One needs to note that the pattern in Fig. 6.3 was taken when the capillary was already opened and the solvent was evaporating. The same pattern was measured in the closed capillary at the same sample orientation.

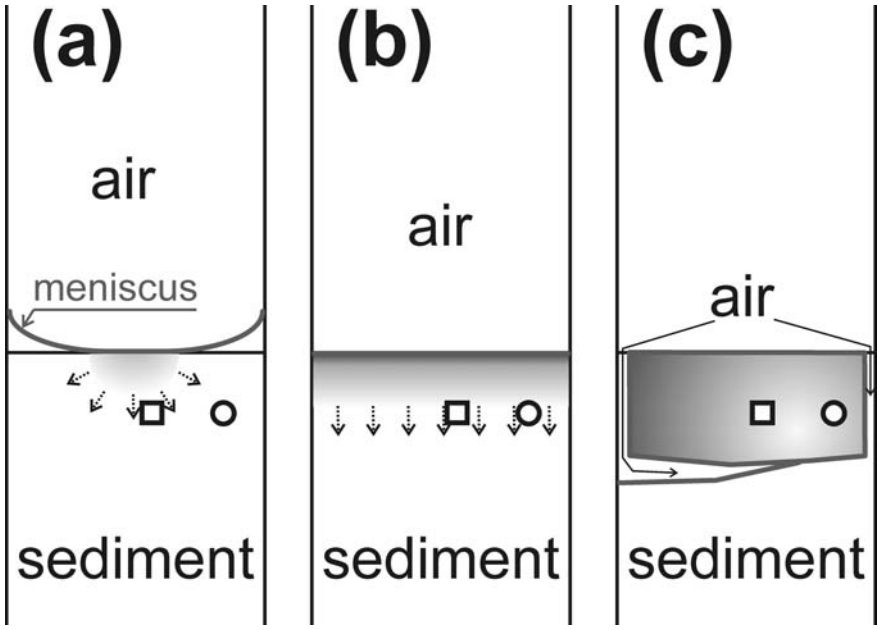

Figure 6.4. Sketch of some of the visually observed stages during drying, when the meniscus reaches the sediment (a), flattens out completely (b), and air penetrates into the sediment (c). These three stages approximately correspond to diffraction patterns shown in Figs. 6.5, 6.6 and 6.8, respectively. The approximate position of the observation point within the sediment in Fig. 6.1d is indicated by a square. Other diffraction patterns were taken at a point indicated by a circle.

Fig. 6.5 presents the diffraction pattern measured when the meniscus touched the sediment [as sketched in Fig. 6.4(a)]. To indicate the time scale in the following, this moment of time is used as t = 0. The pattern in Fig. 6.3 was taken 35 minutes before t = 0. The pattern in Fig. 6.6 was taken at about t=14 minutes, when the meniscus flattened while the sediment was still wet [see Fig. 6.4(b)]. The intensity of the brightest two (110)-type reflections is now significantly reduced, while the other four are strengthened, leading to a (nearly) six-fold symmetric pattern. Now the reflections 2 are only a factor 2 to 2.5 weaker than reflections 1a and 1b. The origin of the modification of the diffraction patterns in Figs. 6.3, 6.5 and 6.6 is illustrated in Fig. 6.7. For a long-range ordered crystal in Fig. 6.3 the reflections are very

narrow (solid line in Fig. 6.7). For two of the (110)-type reflections the Bragg condition is (nearly) fulfilled, i.e., the wave vector mismatch is small (arrow 1). For the other four (110)-type reflections the wave vector mismatch Δq is relatively large so that these reflections are nearly invisible in Fig. 6.5. Upon shortening the positional order, the reflections broaden (dashed line in Fig. 6.7) leading to a strong reduction of the intensity for a small wave vector mismatch in Fig. 6.6.

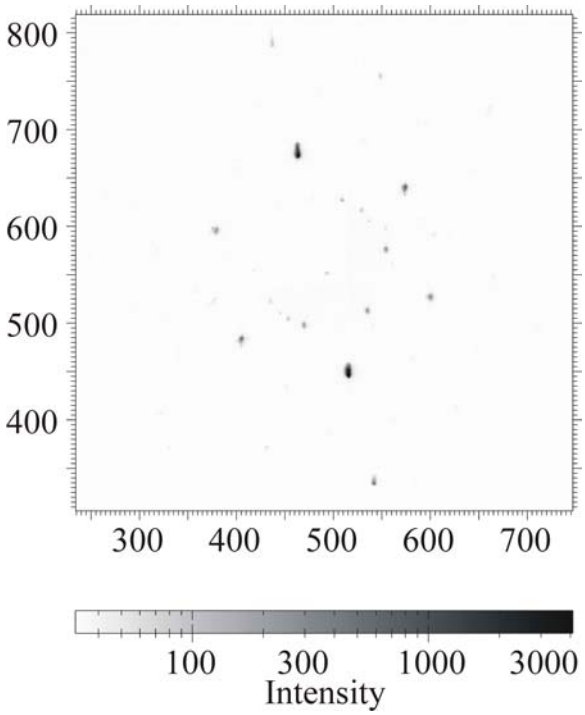

Figure 6.5. Diffraction pattern measured when meniscus touches the sediment (t=0). The exposure time is 10 s.

It should be noted that the asymmetry of the pattern in Fig. 6.3 (reflections 1a and 1b) has disappeared in Fig. 6.5, which indicates that the width of reflections is now $\delta q > \delta q_{\perp,(110)}$. Yet, since two (110)-type diffraction peaks (reflections 1a and 1b) are still much stronger than the other four (reflections 2), δq is smaller than the wave vector mismatch Δq induced by the sample tilt (arrow 2 in Fig. 6.7). Upon further increase of the capillary-force-induced strain field, the width of reflections becomes comparable to the tilt-angle-induced wave vector mismatch Δq (dot-dashed line in Fig. 6.7), so that the intensities of all six reflections of the (110)-type in Fig. 6.6 are similar. This broadening could be explained by shortening the spatial extent of the positional order Λ down to about $2\pi/\Delta q = 20$ μm.

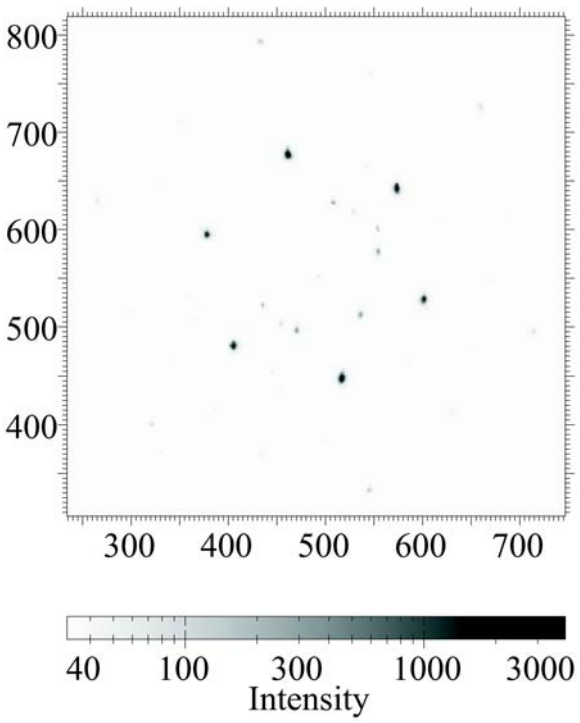

Figure 6.6. Diffraction pattern measured when meniscus becomes flat (t=14 min). The exposure time is 10 s.

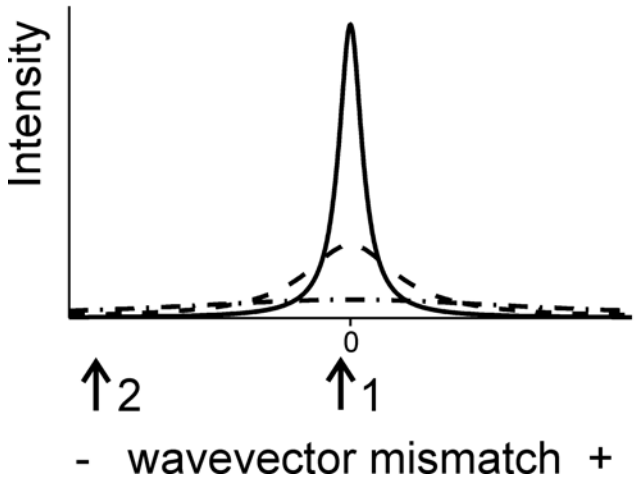

Figure 6.7. Qualitative illustration of modifications of intensities of (110)-type reflections in Figs. 6.3, 6.5 and 6.6, which are induced by shortening the length Λ of positional order.

It should be also noticed that the resolution in the plane of the detector is still too low to resolve the broadening of reciprocal lattice reflections. The reflections in Figs. 6.3, 6.5 and 6.6 keep practically the same shape and width. It should be further mentioned that the stress field may somewhat change the crystal orientation and, thus, affect the wave vector mismatch and the symmetry of the pattern (compare with Fig. 6.1 (a,b,c)). However, it is necessarily

accompanied by a significant broadening of the reflections since their intensity is now very much weaker. The pattern shown in Fig. 6.8 was taken at an instant t=21minutes. At this moment the meniscus turned upside down and air penetrated down along the sides of the capillary [as sketched in Fig. 6.4(c)]). Formation of a large air void in the sediment was visually observed on the TV screen connected to the video camera in the experimental hutch. The diffraction peaks are seen to split into many separate reflections in Fig. 6.8 indicating that the crystal is not able to withstand a too strong stress anymore and it breaks up into smaller crystallites.

Note that the peak broadening was observed only in the azimuthal direction. As illustrated in Fig 6.9, the radial profile kept practically the same instrument-limited width as in Fig. 6.2. The latter result suggests that the crystallites in the mosaic are significantly larger than, and possess positional order over distances more than, the x-ray beam transverse coherence length $l_{tr} > 5…6$ μm (see the discussion of Fig. 6.2). The azimuthal broadening, in turn, is related to decrease of orientational correlation between different crystallites in the mosaic.

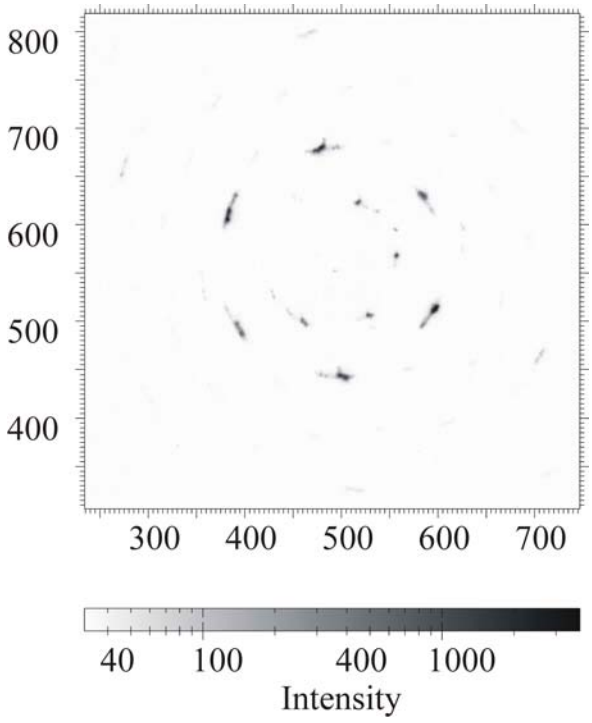

Figure 6.8. Diffraction pattern measured when air penetrated into the sediment (t=21 min). The exposure time is 15 s.

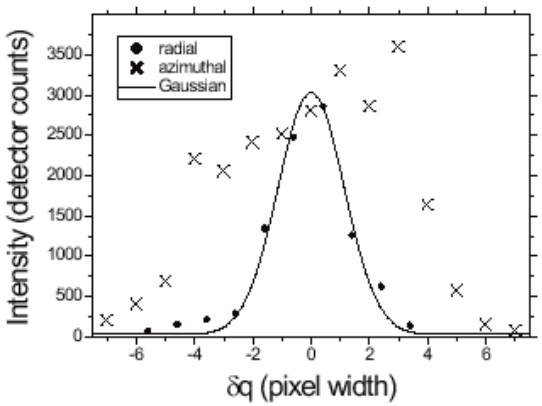

Figure 6.9. Radial (circles) and azimuthal (crosses) profiles through the (110)-type diffraction peak in Fig. 6.8 [around detector pixel with coordinates (x, y)=(600, 515)]. The solid line is a Gaussian function with the same width as in Fig. 6.2.

A similar pattern (Fig. 6.10) was measured at t=28 minutes, when the sediment became turbid and looked dry. However, no significant modification of the diffraction pattern was observed, which suggest that the observation point was still wet. The final drying of the crystal was observed only between t=30 and t=35 minutes as a significant increase of the diffracted intensity due to an enhancement of the scattering contrast as can be seen in Fig. 6.11. We note that apart from the increased intensity, the diffractogram is very similar to that shown in Figs. 6.9 and 6.10.

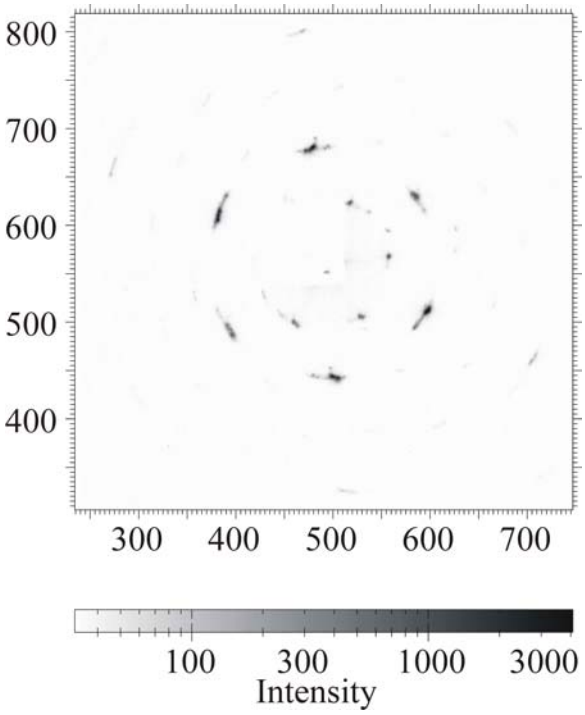

Figure 6.10. Diffraction pattern measured at t=28min. The exposure time is 30s.

Several factors could play a role in the drying process. First of all, solvent evaporation leads to an increase of the concentration of non-absorbing polymer, which osmotically compresses the sediment.

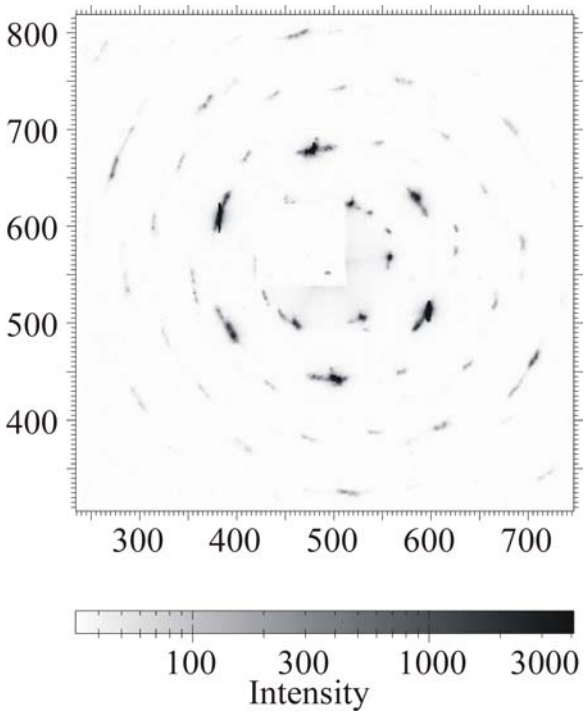

Figure 6.11. Diffraction pattern measured in the dry crystal at t=38 min). Note the increased contrast. The exposure time is 30s.

In the case of slow evaporation (giving sufficient time to equilibrate) the system should follow the so-called drying line [14]. In our experiment evaporation of the volatile cyclohexane was presumably too fast for the polymer diffusion into the sediment to equilibrate its concentration. In this case one could expect a permanent increase of osmotic compression at the top of the sediment starting right after the opening of the capillary. However, we did not observe any remarkable effect in the early stage of the solvent evaporation, when the meniscus was well above the sediment. We cannot, however, completely rule out this effect at later stages when the polymer concentration had raised even further. Fast modification of the diffraction pattern began approximately when the meniscus touched the sediment. As sketched in Fig. 6.4(a) the capillary forces, which can strongly push the colloidal particles together, can come into play. However, they are applied only at the top of the sediment, at a couple of millimeters distance from the observation point. Our results suggest that the stress fields generated by the pressure differences and the strain at the air-

solvent interface are able to elastically propagate over a macroscopically large distance without strong decay (illustrated by arrows and shading in Fig. 6.4). Flattening of the meniscus, as sketched in Fig. 6.4(b), and creation of new air-solvent interfaces inside the sediment, as illustrated in Fig. 6.4(c), increase the area over which the capillary forces act and brings them closer to the observation point. As we have observed, the enhanced stress field leads to further broadening of the crystal reflections followed by a break-up of the single crystal. Surprisingly, the main effect of the drying was detected at the three stages sketched in Fig. 6.4 when the drying front did not yet reach the observation region and there were no capillary forces acting within that part of the crystal. On the contrary, the diffraction pattern did not change anymore when the crystal dried out completely, although colloids at that stage are strongly pushed together by both the capillary forces and the van der Waals attractions (enhanced due to increased refractive index contrast). We finally remark that to disturb the positional order in an ideal single crystal, one has to apply a non-uniform external stress field (e.g., of the bending or screwing type) to the crystal. A colloidal hard-sphere crystal contains a finite density of defects [15] even at thermodynamic equilibrium, much more imperfectness could be induced by numerous growth defects incorporated in the experimental conditions. An additional contribution to lattice disorder might be provided by the polydispersity of the colloidal spheres [16,17]. All these effects could also act as an “internal” source of the stress non-uniformity, which reduces the ability of the crystal to sustain compression.

6.5 Dynamical diffraction

Figure 6.12 shows a three-dimensional plot of the central part of the same diffraction pattern as in Fig. 6.1(a), but measured together with the direct beam. In fact, this is another presentation of the diffraction pattern shown in Fig. 5.5, which provided direct evidence of the dynamic character of the diffraction. This representation is more convenient for a comparison with a diffraction pattern measured at the same spot and the same sample orientation after drying, which is displayed in Fig. 6.13.

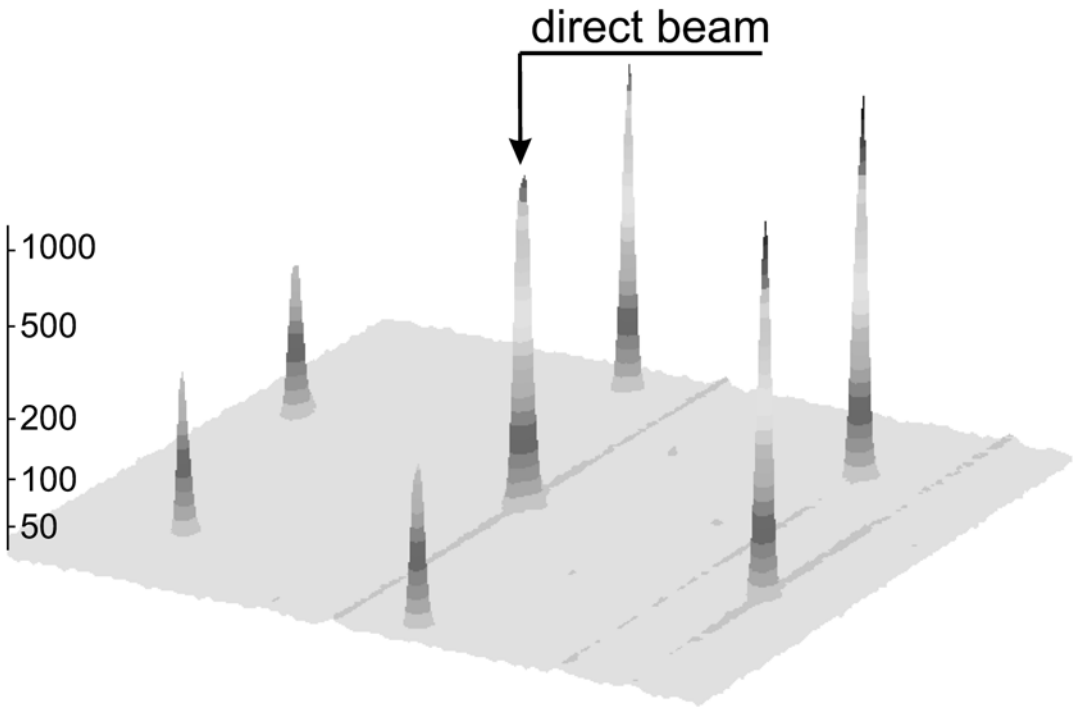

Figure 6.12. Three-dimensional plot of the central part of the same diffraction pattern as in Fig. 6.1(a) but measured without beam stop. The exposure time is 0.1 sec.

Note that the intensity of the direct beam is increased by about a factor of 2 so that we had to use a shorter exposure time ΔT to avoid detector saturation. In the dry crystal the absorption is practically unaffected since it is mostly originating from the silica spheres and the glass walls of the capillary. Thus, variation of the sample extinction of the intensity of the direct beam should be related to sample scattering. After drying the contrast is enhanced by about 80% so that the power scattered by one silica sphere is more than three times larger. Under the instrumental conditions of this experiment, for the strong (110)-class reflections the characteristic length $L^{wet}_{(110)}$ =0.26 mm in a wet colloidal crystal and $L^{dry}_{(110)}$ = 0.14 mm after drying. However, the diffracted intensity is seen to significantly reduce, mostly due to the shortening of the crystal positional correlation length Λ, which overcompensates the shortening of $L_{(110)}$.

As has been discussed in Chapter 5, in order to significantly deplete the direct beam, Λ must be comparable to the sample thickness L in the wet crystal (Fig. 6.12) thus confirming the presence of long-range inter-planar order [1]. This depletion effect, however, significantly weakens in Fig. 6.13 in the dry crystal with $\Lambda << L$, where the pattern can be considered as an incoherent sum of kinematic diffraction patterns originating from small crystal domains. The

results presented in Figs. 6.12 and 6.13 indicate that the strength of the diffraction and its transition into the dynamic regime can be used as an alternative approach to probe the extent of the positional order in colloidal crystals.

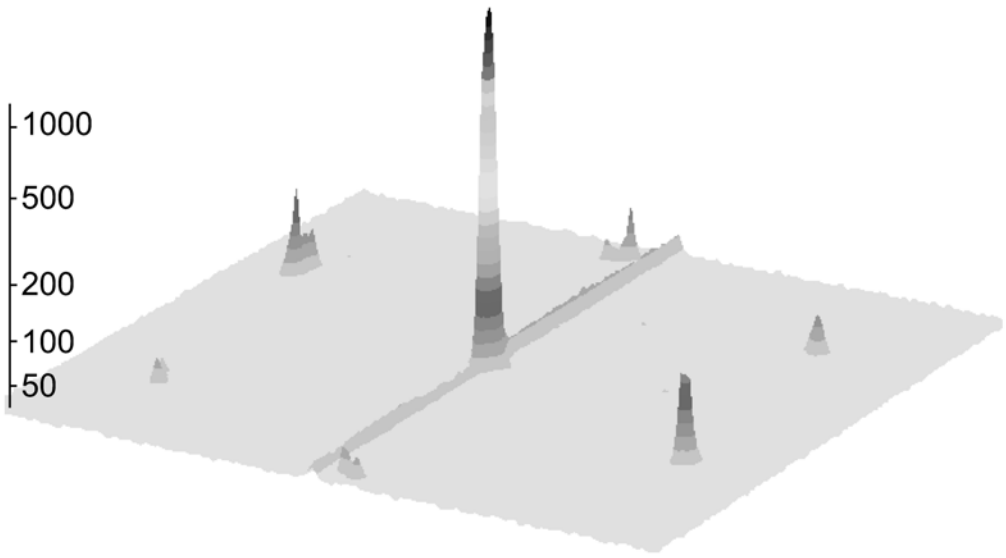

Figure 6.13. Three-dimensional plot of the central part of a diffraction pattern measured without the beam stop in the dry crystal (t=55 min). The exposure time is 0.05 sec. The small "ridge" in the background level is an artefact of the camera caused by the intense direct beam [cf. Fig 6.1(c)]. A similar but somewhat weaker effect can be also seen in Fig. 6.12.

6.6 Conclusion

In the present Chapter we have applied the high-resolution small-angle x-ray diffraction to observe in-situ the modification of the crystal structure caused by capillary forces during drying.

Broadening of the diffraction peaks is observed already when the meniscus reaches the sediment. We associate this with a stress field originating from capillary forces and, possibly, an enhanced osmotic pressure applied at the top of the sediment and elastically propagating down. When air penetrates into the sediment and a wet part of it is encapsulated by the solvent-air interface, the stress crosses a critical value leading to a non-reversible strain and the crystal breaks into many domains with slightly different orientations. All structural

changes observed are induced by external stress fields in the wet crystal and no change in its structure is detected when it finally dries.

The dynamical regime of x-ray diffraction in the long-range ordered colloidal crystal has been also discussed. The diffraction switches to the (nearly) kinematic regime when the long-range positional order is destroyed. Our results indicate that the strength of the diffraction and its transition into the dynamic regime can be used as an alternative approach to probe the extent of the positional order in photonic colloidal crystals.

Literature:

[1] A. V. Petukhov, D. G. A. L. Aarts, I. P. Dolbnya, E. H. A. de Hoog, K. Kassapidou, G. J. Vroege, W. Bras, and H. N. W. Lekkerkerker, Phys. Rev. Lett., **88**, 208301 (2002).

[2] A. V. Petukhov, I. P. Dolbnya, D. G. A. L. Aarts, G. J. Vroege, and H. N. W. Lekkerkerker, Phys. Rev. Lett., **90**, 028304 (2003).

[3] A.F. Routh, W.B. Russel, Langmuir, **15**, 7762 (1999).

[4] Y.A. Vlasov, X.-Z. Bo, J.C. Sturm, and D.J. Norris, Nature (London) **414**, 289 (2001)

[5] K.P. Velikov, C.G. Christova, R.P.A. Dullens, A. van Blaaderen, Science, **296**,106 (2002).

[6] N.A.M. Verhaegh and A. van Blaaderen, Langmuir 10, 1427 (1994); N.A.M. Verhaegh, D. Asnaghi, and H.N.W. Lekkerkerker, Physica (Amsterdam) **264A**, 64 (1999); E.H.A. de Hoog, *et al.*, Langmuir **17**, 5486 (2001).

[7] E.H.A. de Hoog, PhD thesis, University of Utrecht (2001) [Chapter 6].

[8] J.Zhu, M.Li, R.Rogers, W.Meyer, R.H.Ottewill,W.B. Russel, and P.M. Chaikin, Nature (London) **387**, 883 (1997).

[9] H. Versmold, S. Musa and A. Bierbaum, J.Chem.Phys. **116**, 2658 (2002).

[10] N.A.M. Verhaegh, J.S. van Duijneveldt, A. van Blaaderen, and H.N.W. Lekkerkerker, J. Chem. Phys. **102**, 1416 (1995).

[11] W.K. Kegel and J.K.G. Dhont, J. Chem. Phys. **112**, 3431 (2000).

[12] Ch. Dux and H.Versmold, Phys. Rev. Lett. **78**, 1811 (1997).

[13] S. Pronk and D. Frenkel, J. Chem. Phys. **110**, 4589 (1999).

[14] M.D. Haw, M. Gillie, W.C. Poon, Langmuir, **18**, 1626 (2002).

[15] J.M. Polson, E. Trizac, S. Pronk, D. Frenkel, J. Chem. Phys. **112**, 5339 (2000).

[16] S.R. Williams, I.K. Snook, and W. van Megen, Phys. Rev. E **64**, 021506 (2001).

[17] W.G.T. Kranendonk and D. Frenkel, Mol. Phys., **72**, 679 (1991).

[18] W. Vos, M. Megens, C.M. van Kats, and P. Bosecke, Langmuir **13**, 6004 (1997); J.E.G.J. Wijnhoven, L. Bechger, and W.L. Vos, Chem. Mater, **13**, 4486 (2001).

Summary

An extensive synchrotron small-angle X-ray diffraction study of various order/disorder parameters in silica hard-sphere colloidal crystals has been carried out. By using high-resolution synchrotron small-angle X-ray diffraction, measurements of the orientational, positional and stacking order in crystals of ~4 % polydisperse hard colloidal silica spheres grown in sediments of colloid-polymer mixtures have been performed on beamline BM26B DUBBLE at the European Synchrotron Radiation Facility (ESRF) in Grenoble, France. The beamline characteristics and SAXS setup are described in detail in Chapter 2. It turned out that the issue of the instrumental resolution of the whole apparatus played a crucial role in such measurements and had to satisfy certain requirements. This is considered in Chapter 2 (Section 2.5) and, partially, in Chapter 6 (Section 6.2) for both cases of real and reciprocal spaces.

The experimental results obtained agree well with the diffraction theory developed by Guinier and Wilson for different types of close-packed structures (*fcc*, *hcp*) and various types (and degrees) of stacking disorder (Chapter 3). The present work reports a first unambiguous prove that hard-sphere colloidal crystals can possess perfect positional order over distances comparable to the crystal size despite the size polydispersity of colloidal spheres. This conclusion is drawn from a profound evaluation of the size of the reciprocal lattice reflections using a specially-designed high-resolution X-ray diffraction technique with a resolution of one millionth of the incoming wave vector (Chapter 4).

The data presented allowed an accurate characterization of various long-range order parameters and clearly revealed that the inherent size polydispersity of colloids does not prevent the formation of large high-quality single crystals possessing long-range positional and orientational order (Chapter 4). A random stacking hexagonal close-packed (*rhcp*) structure was experimentally determined. The present results suggest that the stacking disorder has a long lifetime (much longer than a year) or might even be the stable state. The structure displayed by hard-sphere crystals distinctly differs from the structure of *charge-stabilized* colloidal crystals [Vos et al.].

Although the latter have a mosaic structure with a much shorter extent of the positional order, they do display a high degree of *fcc* stacking order.

Another experimental observation (Chapter 4, Section 4.5) is that our results suggest that for the hard-sphere crystals the stacking parameter α may only have two discrete values of 0.5 (for *rhcp* structure) and 1 (for *fcc*).

In Chapter 5, direct evidence of a dynamic regime of X-ray diffraction in our long-range ordered colloidal crystal is demonstrated. It reveals itself in the diffraction patterns as an appearance of secondary Bragg rods. Simple estimates show that, in contrast to common belief, dynamic x-ray diffraction must be rather typical for crystals consisting of highly ordered (sub)micrometer colloidal spheres and has to be taken into account. The estimates given show that the presence of long-range order along the beam is essential for the transition of diffraction from the kinematic into the dynamic regime.

Chapter 6 reports the *in-situ* observation of the crystal structure modification during drying. It is important to know how the structure and quality of the crystal is changing upon drying as the drying process might be needed, for example, for photonic applications where a colloidal crystal is used as a template to fabricate a band-gap photonic material. We observed that at later stages of drying the diffraction peaks are seen to split into many separate reflections indicating that the crystal is not able to withstand a too strong stress, caused by capillary forces, anymore and it breaks up into smaller crystallites. We also observed peak broadening in the azimuthal direction. However, the radial profile of the Bragg reflections kept practically the same instrument-limited width as it had before drying. The latter result suggests that the crystallites in the mosaic are significantly larger than, and retain positional order over distances more than, the x-ray beam transverse coherence length $l_{tr} > 5\ldots6$ μm, estimated for this particular experiment discussed. The azimuthal broadening, in turn, is related to a decrease of orientational correlation between different crystallites in the mosaic.

All structural changes observed are induced by external stress fields in the wet crystal and no change in its structure is detected when it finally dries.

We also see another manifestation of the dynamical regime of x-ray diffraction in the long-range ordered colloidal crystal. The diffraction switches to the (nearly) kinematic regime when the long-range positional order is destroyed. Our results indicate that the strength of the diffraction and its transition to the dynamic regime can be used as an alternative approach to probe the extent of the positional order in photonic colloidal crystals.

Samenvatting

Dit proefschrift beschrijft een uitgebreide studie van de orde/wanorde parameters in colloïdale kristallen in silicadispersies. Met behulp van hoge resolutie synchrotron SAXS (= kleine hoek Röntgenverstrooiing), uitgevoerd op de BM26B DUBBLE bundellijn van het ESRF (=European Synchrotron Radiation Facility te Grenoble, Frankrijk), zijn metingen verricht aan de oriëntatie-, positie- en stapelingsorde in kristallen van 4 % polydisperse harde colloïdale silicabollen, gevormd in het sediment van colloïd-polymeermengsels. In hoofdstuk 2 worden de karakteristieken van de bundellijn en de SAXS opstelling in detail beschreven. De instrumentele resolutie van het totale apparaat bleek een cruciale rol te spelen bij de metingen en moest daarom aan een aantal eisen voldoen. Deze worden beschouwd in hoofdstuk 2 (sectie 2.5) en in hoofdstuk 6 (sectie 6.2) voor de reële en de reciproke ruimte.

De experimenteel verkregen resultaten komen goed overeen met de diffractietheorie ontwikkeld door Guinier en Wilson voor verschillende soorten dichtgepakte structuren (*fcc*, *hcp*) en verschillende soorten (en mate) van stapelingswanorde (hoofdstuk 3). Het hier gepresenteerde werk toont voor het eerst ondubbelzinnig aan dat colloïdale kristallen perfecte positionele ordening kunnen vertonen op afstanden vergelijkbaar met de kristalgrootte (hier 0,1 mm) ondanks de polydispersiteit van de colloïdale bollen. Deze conclusie kan getrokken worden uit een diepgaande evaluatie van de uitgebreidheid van de reflecties in het reciproke rooster op basis van een speciaal ontwikkelde hoge resolutie Röntgendiffractie techniek met een resolutie van een miljoenste van de inkomende golfvector (hoofdstuk 4).

De hier gepresenteerde gegevens lieten een nauwkeurige karakterisering toe van verschillende ordeparameters en toonden duidelijk aan dat de inherente polydispersiteit van de colloïden geen belemmering vormt voor de vorming van grote éénkristallen van hoge kwaliteit wat betreft hun positie- en oriëntatie-ordening op lange afstanden (hoofdstuk 4). Er werd een willekeurig gestapelde hexagonale dichtgepakte (*rhcp*) structuur vastgesteld. De resultaten suggereren dat de

stapelingswanorde een lange levensduur heeft (veel langer dan een jaar) of zelfs de stabiele toestand zou kunnen zijn. De structuur van deze harde bollen kristallen verschilt duidelijk van die van ladingsgestabiliseerde colloïdale kristallen [Vos et al.]. Hoewel die laatste een mozaiekstructuur bezitten met een veel minder sterk ontwikkelde positie-ordening, vertonen ze juist een hoge mate van *fcc* stapelingsordening.

De experimentele waarnemingen (sectie 4.5) suggereren verder dat in harde bollen kristallen de stapelingsparameter α slechts twee discrete waarden 0.5 (van de *rhcp* structuur) en 1 (van *fcc*) kan aannemen.

In hoofdstuk 5 wordt een direct bewijs geleverd van het bestaan van een dynamisch regime van Röntgenverstrooiing in deze colloïdale kristallen. Dit komt in de verstrooiingspatronen tot uiting in de vorm van secundaire Bragg "rods". Eenvoudige schattingen laten zien dat - in tegenstelling tot wat vaak aangenomen wordt - dynamische Röntgenverstrooiing eerder regel dan uitzondering is voor sterk geordende (sub)micrometer colloïdale bollen. Deze schattingen tonen aan dat de aanwezigheid van ordening over lange afstanden langs de bundel essentieel is voor de overgang van het kinematische naar het dynamische regime van diffractie.

Hoofdstuk 6 rapporteert over de waarneming *in situ* van de veranderingen in structuur en de kwaliteit van het kristal tijdens het indrogen. Dit is van belang omdat het indroogproces onder andere toegepast wordt bij fotonische toepassingen, waarbij een colloïdaal kristal als "template"wordt gebruikt om een zogenaamd fotonisch "band-gap" materiaal te produceren. Tijdens de latere stadia van het indrogen blijken de diffractiepieken zich op te splitsen in vele afzonderlijke reflecties, hetgeen erop wijst dat het kristal niet in staat is langer weerstand te bieden aan de sterke spanning veroorzaakt door de capillaire krachten en in kleinere kristallieten opbreekt. Er wordt ook piekverbreding in de azimuthale richting waargenomen, terwijl het radiële profiel van de Bragg reflecties daarentegen vrijwel dezelfde (instrument gelimiteerde) breedte behoudt als voor het indrogen. Dit laatste suggereert dat de kristallieten in het mozaiek significant groter zijn en hun positie-ordening behouden op afstanden groter dan de transversale coherentielengte van de Röntgenbundel (hier $l_{tr} > 5\ldots6$ μm). De

azimuthale verbreding is gerelateerd aan de afname van de correlatie in oriëntatie tussen verschillende kristallieten in het mozaiek.

Alle waargenomen structurele veranderingen worden geinduceerd door externe spanningsvelden in het bevochtigde kristal en er wordt geen verdere verandering in de structuur waargenomen als het kristal uiteindelijk opdroogt.

Ook hier manifesteert zich het dynamische regime van Röntgenverstrooiing in het oorspronkelijke colloïdale kristal. De diffractie gaat over in het kinematische regime zodra de ordening op lange afstanden verloren gaat. De resultaten suggereren dat de sterkte van de diffractie en de overgang naar het dynamische regime gebruikt kunnen worden als een alternatieve methode om de mate van positie-ordening in fotonische colloïdale kristallen te bepalen.

Curriculum Vitae

Igor Petrovich Dolbnya was born on December 11th, 1962, in Krasnoyarsk city (Siberia, Russia). In June 1986 he graduated from the Physics Department of Novosibirsk State University. The topic of his Master research project was "A CCD linear-array detector with MCP image intensifier for time-resolved X-ray scattering experiments". Since then Igor Dolbnya worked at the Synchrotron Radiation (SR) Lab at the Budker Institute of Nuclear Physics (BINP) of the Siberian Branch of the Russian Academy of Science in Novosibirsk, Russia, where he worked as a Research Associate, Junior Scientific Researcher (since 1988), Research Physicist (since 1992) and Senior Scientist (since 1998). In 1996 – 1997 he also worked at Pohang Accelerator Laboratory, University of Science and Technology, South Korea as a Postdoctoral Fellow. In 1999 Igor Dolbnya worked at the FOM-Institute for Atomic and Molecular Physics (AMOLF) as a Guest Scientist and in the summer 1999 he moved to Grenoble, France, where he joined the DUBBLE team. Since April 2000 he works as a beamline scientist at DUBBLE, where he is responsible for the SAXS/WAXS Instrument and, partially, for the Interface Diffractometer at the hard line of DUBBLE.

The scientific interests of Igor Dolbnya are rather wide. His previous experience was mostly concentrated on X-ray imaging (X-ray microscopy and microtomography, X-ray fluorescence scanning microprobe elemental analysis, subtraction angiography, X-ray phase-contrast imaging), small-angle X-ray scattering, powder and single-crystal X-ray diffraction. He was also designing, developing and building different SR instrumentation such as beamlines, X-ray monochromators and detectors. His previous work resulted in about 60 scientific publications.

Publications

This thesis is based on the following papers:

Petukhov A.V., Dolbnya I.P., Aarts D.G.A.L. and Vroege G.J., Destruction of long-range order recorded with in-situ small-angle x-ray diffraction in drying colloidal crystals,
Phys. Rev. E, *in press*.

Petukhov A.V., Dolbnya I.P., Aarts D.G.A.L., Vroege G.J. and Lekkerkerker H.N.W., Bragg Rods and Multiple X-Ray Scattering in Random-Stacking Colloidal Crystals, *Phys. Rev. Letters, 90, 028304 (2003)*.

Petukhov A.V., Aarts D.G.A.L., Dolbnya I.P., de Hoog E.H.A., Kassapidou K., Vroege G.J., Bras W. and Lekkerkerker H.N.W., High-Resolution Small-Angle X-Ray Diffraction Study of Long-Range Order in Hard-Sphere Colloidal Crystals, *Phys. Rev. Letters, 88, 208301 (2002)*.

Dolbnya I.P., Petukhov A.V., Aarts D.G.A.L., Vroege G.J. and Lekkerkerker H.N.W., Coexistence of *rhcp* and *fcc* Phases in Hard-Spere Colloidal Crystals, *to be submitted*.

Dolbnya I.P., Alberda H., Hartjes F.G., Udo F., Bakker R.E., Konijnenburg M., Homan E., Cerjak I., Goedtkindt P. and Bras W., A fast position sensitive MSGC detector at high count rate operation, *Rev. of Sci. Instrum., 73 No. 11, 3754 (2002)*.

Other papers by the author since 2000:

Vanhaecht B., Willem R., Biesemans M., Goderis B., Basiura M., Magusin P.C.M.M., Dolbnya I., and Koning C.E., A WAXD and Solid-State NMR Study on Cocrystallization in Partially Cycloaliphatic Polyamide 12.6-Based Copolymers, *Macromolecules, 37 (2): 421-428 (2004).*

Dermaut F., Van den Kerkhof T., Goderis B., Mertens R., Dolbnya I., Van der Veken B.J., Blockhuys F., Geise H.J., A volume-corrected Kratky model and the influence of the shape of the orientation distribution function on the molecular orientation in PPV and its precursor,
Macromolecules, 37 (1): 110-117 (2004).

A.V. Petukhov, J.H.J. Thijssen, A. Imhof, A. van Blaaderen, I.P. Dolbnya, A. Snigirev,
I. Snigireva, M. Drakopoulos, 3D Structure and (Dis-)order in Photonic Crystals by Microradian Synchrotron X-ray Diffraction,
ESRF Newsletter No. 38 (2003)..

Sikharulidze I., Farago B., Dolbnya I.P., Madsen A., de Jeu W.H., Surface and bulk elasticity determined fluctuation regimes in smectic membranes,
Phys. Rev. Letters, 91 (16): Art. No. 165504 (2003).

de Jager M.W., Gooris G.S., Dolbnya I.P., Bras W., Ponec M., Bouwstra J.A., The phase behaviour of skin lipid mixtures based on synthetic ceramides,
Chemistry and Physics of Lipids, 124 (2): 123-134 (2003).

Heeley E.L., Maidens A.V., Olmsted P.D., Bras W., Dolbnya I.P., Fairclough J.P.A., Terrill N.J., Ryan A.J., Early stages of crystallization in isotactic polypropylene,
Macromolecules, 36 (10): 3656-3665 (2003).

Xian X., Petukhov A.V., Snel M.M.E., Dolbnya I.P., Aarts D.G.A.L., Vroege G.J., Lekkerkerker H.N.W., Depletion-induced colloidal crystals at a wall characterised by small-angle X-ray diffraction,
Journal of Applied Crystallography, 36: 597-601 Part 3 Sp. Iss. 1 (2003).

Knaapila M., Torkkeli M., Jokela K, Kisko K, Horsburgh L.E., Palsson L.O., Seeck O.H., Dolbnya I.P., Bras W., ten Brinke G., Monkman A.P., Ikkala O., Serimaa R., Diffraction analysis of highly ordered smectic supramolecules of conjugated rodlike polymers,
Journal of Applied Crystallography, 36: 702-707 Part 3 Sp. Iss. 1 (2003).

Meneau F., Cristol S., Sankar G., Dolbnya I.P., Bras W., Catlow C.R.A., Thomas J.M., Greaves G.N., In situ study of the formation of CdS nanoparticles by small-angle X-ray scattering,
Journal of Applied Crystallography, 36: 718-721 Part 3 Sp. Iss. 1 (2003).

Bras W., Dolbnya I.P., Detollenaere D., van Tol R., Malfois M., Greaves G.N., Ryan A.J., Heeley E., Recent experiments on a combined small-angle/wide-angle X-ray scattering beam line at the ESRF,
Journal of Applied Crystallography, 36: 791-794 Part 3 Sp. Iss. 1 (2003).

Polushkin E., van Ekenstein G.A., Dolbnya I., Bras W., Ikkala O., ten Brinke G., In situ radial small angle synchrotron X-ray scattering study of shear-induced macroscopic orientation of hierarchically structured comb-shaped supramolecules,
Macromolecules, 36 (5): 1421-1423 (2003).

Stevenson A.W., Gureyev T.E., Paganin D., Wilkins S.W., Weitkamp T., Snigirev A., Rau C., Snigireva I., Youn H.S., Dolbnya I.P., Yun W., Lai B., Garrett R.F., Cookson D.J., Hyodo K., Ando M., Phase-contrast X-ray imaging with synchrotron radiation for materials science applications,
Nuclear Instruments & Methods, Sec. B, 199: 427-435 (2003).

Bell P.C., Bergsma M., Dolbnya I.P., Bras W., Stuart M.C.A., Rowan A.E., Feiters M.C., Engberts J.B.F.N., Transfection mediated by gemini surfactants: Engineered escape from the endosomal compartment,
Journal of the American Chemical Society 125 (6): 1551-1558 (2003).

Caseri W.R., Chanzy H.D., Feldman K., Fontana M., Smith P., Tervoort T.A., Goossens J.G.P., Meijer E.W., Schenning A.P.H.J., Dolbnya I.P., Debije M.G., de Haas M.P., Warman J.M., van de Craats A.M., Friend R.H., Sirringhaus H., Stutzmann N.,
"(Hot-)Water-Proof", semiconducting, platinum-based chain structures: Processing, products, and properties,
Advanced Materials 15 (2): p. 125 (2003).

Jongen L., Goderis B., Dolbnya I., Binnemans K., Influence of the chain length on the thermal behavior of lanthanide(III) 4-alkoxybenzoates,
Chemistry of Materials, 15 (1): 212-217 (2003).

Heeley E.L., Poh C.K., Li W., Maidens A., Bras W., Dolbnya I.P., Gleeson A.J., Terrill N.J., Fairclough J.P.A., Olmsted P.D., Ristic R.I., Hounslow M.J., Ryan A.J., Are metastable, precrystallisation, density-fluctuations a universal phenomena?,
Faraday Discussions, 122: 343-361 (2003).

ESRF Highlights 2002, p. 19.

Carbajal-Tinoco M.D., Ober R., Dolbnya I., Bras W., Williams C.E., Structural changes and chain conformation of hydrophobic polyelectrolytes,
Journal of Physical Chemistry B , 106 (47): 12165-12169 (2002).

Heeley E.L., Morgovan A.C., Bras W., Dolbnya I.P., Gleeson A.J., Ryan A.J., Shear-induced crystallization of polyethylene studied by small- and wide-angle X-ray scattering (SAXS/WAXS) techniques,
Physchemcomm, 5(23): 158-160 (2002).

Knaapila M., Ikkala O., Torkkeli M., Jokela K., Serimaa R., Dolbnya I.P., Bras W., ten Brinke G., Horsburgh L.E., Palsson L.O., Monkman A.P., Polarized luminescence from
self-assembled, aligned, and cleaved supramolecules of highly ordered rodlike polymers,
Applied Physics Letters, 81 (8): 1489-1491 (2002).

Sikharulidze I., Dolbnya I.P., Fera A., Madsen A., Ostrovskii B.I., de Jeu W.H., Smectic membranes in motion: Approaching the fast limits of X-ray photon correlation spectroscopy,
Phys. Rev. Letters, 88 (11): Art. No. 115503 (2002).

Polushkin E., van Ekenstein G.A., Knaapila M., Ruokolainen J., Torkkeli M., Serimaa R., Bras W., Dolbnya I., Ikkala O., ten Brinke G., Intermediate segregation type chain length dependence of the long period of lamellar microdomain structures of supramolecular comb-coil diblocks,
Macromolecules, 34 (14): 4917-4922 (2001).

Fera A., Dolbnya I.P., Opitz R., Ostrovskii B.I., de Jeu W.H., Crystalline smectic-B films as fluctuating systems: Static and dynamic x-ray scattering,
Phys. Review E, 63 (2): Art. No. 020601 Part 1 (2001).

Fera A., Dolbnya I.P., Grubel G., Muller H.G., Ostrovskii B.I., Shalaginov A.N., de Jeu W.H., Complex dynamic behavior of fluctuating smectic-A films as studied by scattering with coherent X-rays,
Phys. Rev. Letters, 85 (11): 2316-2319 (2000).

Acknowledgements

As I started thinking about this last part of the thesis I realized, at some stage, that it is nearly impossible to mention and thank so many people with whom I interacted and communicated through all these years and who contributed, in a varying degree and various manner, into the present work, in particular, and the DUBBLE project, in general. This is just an illusion. So, if I don't mention your name: this does not mean that I am less grateful …!

Nevertheless, I don't give up and let me thank at least some people.
First of all, I would like to express my gratitude to Henk Lekkerkerker, Andrei Petukhov, Gert-Jan Vroege and Wim Bras for their help, support and care as without that it was nearly impossible to finish this work. They know the rest ...

I address my special thanks to Wim de Jeu, Dirk Detollenaere, Elias Vlieg, Ruud van Tol, Dirk Aarts, Xinyi Xian, Els de Hoog, Karen Butter, Bonny Kuipers, Karel van der Werf, David van der Beek, Dick Glastra van Loon, Iliya Cerjak, Menno Oversluizen, Peter Goedkindt, Els Homan-Tol, Jeroen Jacobs, Hans Alberda, Andre Gabriel, Marco Konijnenburg, Piet Lassing, Sven Hoffmann, Henk Shenk, Harry Reynaers, Bart Goderis, Alfons van Blaaderen, Arnout Imhof, Job Thijssen, Boris Ostrovskii, Irakli Sikharulidze, Andrea Fera, Anatoly Snigirev, Irina Snigireva, Alexander Chumakov, Sergey Nikitenko, Claudio Ferrero, Menhard Kocsis, Michael Drakopoulos and to my many other friends and colleagues whom I knew and know and who knew and know me.

I realize that the list is not complete, but I hope you will forgive me for this something probably an utterly inadequate "You know who you are, and … thanks a lot to all of you!" I will remember you all … and never forget!
Bedankt voor alles!